Femtosecond Nonlinearities in AlGaAs Diode Laser Amplifiers

by

Charles Timothy Hultgren

B.S., University of California at Berkeley
(1987)

S.M., Massachusetts Institute of Technology
(1991)

Submitted to
the Department of Electrical Engineering and Computer Science
in partial fulfillment of the requirements
for the degree of

Doctor of Philosophy

at the

Massachusetts Institute of Technology

July 1994

Signature of Author______________________________________
Department of Electrical Engineering and Computer Science
July 25, 1994

Certified by______________________________________
Erich P. Ippen
Thesis Advisor

Accepted by______________________________________
Frederic R. Morgenthaler
Chairman, Committee on Graduate Students

Femtosecond Nonlinearities in AlGaAs Diode Laser Amplifiers

by

Charles Timothy Hultgren

Submitted to
the Department of Electrical Engineering and Computer Science
on July 25, 1994 in partial fulfillment of the requirements
for the degree of Doctor of Philosophy.

Abstract

As optical communication systems continue to advance in speed and complexity, the demand grows for high-speed devices to perform wavelength conversion, multiplexing, and switching operations. Semiconductor diode laser amplifiers exhibit large and ultrafast optical nonlinearities that make them promising candidates as the basic building blocks for such all-optical devices. The primary goal of this thesis is the measurement and characterization of the ultrafast optical nonlinearities exhibited by an AlGaAs diode laser amplifier. The results lead to a better understanding of fundamental processes in semiconductors and enable the evaluation of active semiconductor waveguides for use in all-optical devices.

This thesis presents a detailed study of ultrafast gain and refractive index dynamics in a bulk AlGaAs diode laser amplifier. Pump-probe measurements are performed with ~100 femtosecond optical pulses generated by a modelocked titanium:sapphire laser system. The refractive index measurements employ a time-division interferometer that allows the measurement of phase shifts as small as $\pi/1000$ radians. Measurements of gain and refractive index dynamics are performed at a series of carrier densities and over a broad range of above- and below-band wavelengths – from 810 to 905 nanometers. The phenomena encountered in this work include two-photon absorption, carrier heating through free-carrier absorption, spectral hole burning, carrier cooling through stimulated transitions, and an instantaneous refractive index dynamic attributed to the optical Stark effect. The carrier heating dynamic recovers with a 1.1 picosecond time constant, and below-band refractive index measurements show that there is a delay of ~120 femtoseconds in the onset of carrier heating. Values for the nonlinear refractive index coefficients associated with the carrier heating index nonlinearity and the instantaneous index nonlinearity are determined as a function of wavelength and carrier density. For the instantaneous index dynamic, a maximum $n_{2\perp}$ of -5×10^{-12} cm^2/W is measured.

Thesis Advisor: Erich P. Ippen
Title: Elihu Thomson Professor of Electrical Engineering

Acknowledgements

First, I would like to thank my advisor Professor Erich Ippen, whose guidance and support over the past six years kept me going in the right direction and made this thesis possible. His creativity and physical insight were invaluable to explaining the numerous puzzles that were encountered throughout this work. Professors Clifton Fonstad and Shaoul Ezekiel, as members of my thesis committee, provided useful comments and suggestions about the work presented here. I am very grateful to Chris Cook of MIT Lincoln Laboratory – his expertise in anti-reflection coatings helped to make these experiments a success.

Dr. Stuart Brorson was my mentor in the early years – he taught me much of what I know about lasers and solid state physics, and everything I know about GEC. Edward Lizine, Building 36 custodian, was a welcome companion during many late-night experiments. Jack Dann made himself available after hours and on weekends to lend a hand with computations. Anna at the Bradford provided countless hours of guidance and advice. Dr. Katie Hall, despite a continuous stream of so-called jokes, was my favorite office mate and the developer of many novel experimental techniques.

Thanks to David Dougherty, Gadi Lenz, Reginald Foghat, Mike Connell, Conrad Zoso, and Siegfried Fleisher, the members of the Bitter Coffee and Science Klüb, who taught me a unique appreciation for femtosecond pulses and most of what I know about nonlinear optics. I know they will miss me as much as I will miss them. Nick Ulman warrants special mention for inspiring me to finish-up quickly and head west to the land of burritos and hockey. Alex Guimaraes, Mike Brandstein, Abbas Kashani, and Don Keeshow provided endless amusements outside of the darkened optics lab. During the early years, Minoru Akuhara helped me to explore and appreciate the nightlife of Boston and the wonderful beaches of New England. Other persons who one way or another made a special contribution to my experience here include Mitch Dmohowski, Dan Kiefer, Trad'r Sam, Nick Kiefer, Burr Fabidacola, John Wei, and Robert Cornell.

Aside from myself, the one person who has waited the longest for this moment to arrive is Katie Power. I thank her for her patience and friendship throughout this ordeal, and I look forward to seeing her on a more frequent basis.

Finally, thanks to my family – David, Carrie, mom, and dad – for your love and support. Out the door in '94!

To Dube and Bojack.

Contents

List of Figures

Chapter 1

Introduction

High speed optical communication systems are now capable of operating at gigabits per second transmission rates. Future long-haul fiber optic links may operate at even higher bit rates. Further, these high-speed capabilities could be applied to other lightwave transmission systems such as local area networks and board-to-board and even chip-to-chip communication systems in computers. As bit rates begin to exceed the capacity of high-speed electronics, the demand for high-speed all-optical devices grows. Examples of such devices include optical amplifiers, optical switches, multiplexers and demultiplexers, and wavelength converters.

These devices might be realized in a variety of materials and structures – leading candidates include organic materials, fiber optic-based devices, and semiconductor waveguide structures. Each approach possesses inherent advantages and disadvantages. For instance, organic materials exhibit strong optical nonlinearities but are easily damaged by environmental stresses such as heat and water vapor. Fiber optic-based devices possess weak nonlinearities, but the low loss in optical fiber allows long interaction lengths to be employed. This results in a large refractive index nonlinearity with little absorption. However, the long device length implies latency problems and large device sizes. Semiconductor waveguide devices are attractive because they are compact, robust, and potentially compatible with existing electronic semiconductor devices. Semiconductor-based devices exhibit large refractive index nonlinearities, but these are often accompanied by large absorptive nonlinearities as well.

This thesis is an investigation of optical nonlinearities in semiconductor waveguides. In particular, a detailed study of ultrafast gain and refractive index dynamics in an AlGaAs diode laser amplifier is presented. The fundamental processes that will be addressed include free carrier absorption, two-photon absorption, stimulated transitions, spectral hole burning, and the optical Stark effect. These processes give rise to a rich variety of gain and refractive index dynamics which are studied as a function of wavelength and carrier density. The results of these studies are interesting from a purely fundamental standpoint because they reveal how photons interact with carriers in a semiconductor. In addition, these studies are of practical relevance to the development of devices that employ active semiconductor waveguides. The results will help to reveal the feasibility of such devices and possible ways to optimize their performance. In this introductory chapter we present a brief overview – first, of the relevant measurements that have been performed previously and second, of the main issues that we are concerned with for this thesis.

1.1 Background

Broadly speaking, there are two complementary approaches to the study of ultrafast optical nonlinearities in semiconductor waveguides. The first employs short optical pulses in a pump and probe configuration to perturb a sample and measure its response in time [1]. The second approach involves frequency domain methods such as four-wave mixing [2]. Other related experimental methods include high frequency diode laser modulation response [3, 4, 5, 6, 7, 8] and spectral distortions imparted to short optical pulses propagating through waveguides [9, 10, 11].

A great deal of time-resolved pump-probe studies have been performed on active and passive semiconductor waveguide structures. Early measurements involved pump-probe studies of gain dynamics in an AlGaAs diode laser amplifier using pulses from a dye laser system [12, 13, 14]. In this sort of measurement, the pump perturbs the sample, and the probe senses the gain change caused by the pump. Measuring the probe transmission through the waveguide as a function of the time delay between the two pulses reveals the ultrafast semiconductor gain dynamics. Since then, additional gain measurements have been performed with ~100 femtosecond pulses on AlGaAs devices around 0.8 μm [15, 16, 17, 18], InGaAs around 0.9 μm [19, 20, 21], and InGaAsP around 1.5 μm [22, 23, 24].

In recent years the pump-probe experimental technique has been modified to enable the measurement of refractive index dynamics. These measurements are conceptually similar to gain measurements, but they require a bit more ingenuity. The basic idea is to measure the phase shift of the probe pulse as a function of pump-probe delay. This is usually accomplished with a third pulse that acts as a phase reference for the probe. The measured probe phase shift can then be related to the pump-induced refractive index dynamics. In this thesis, measurement of refractive index dynamics is accomplished with a time-division interferometer (TDI). The TDI enables very stable and accurate measurements of small pump-induced index changes in a waveguide. The TDI was first used in optical fiber measurements [25, 26] and below-band measurements of passive AlGaAs waveguides [27, 28, 29]. Here, we combine the standard pump-probe gain measurement and the TDI to study both gain and refractive index dynamics in an active AlGaAs waveguide.

Recently, other methods for performing pump-probe measurements in waveguides have been developed. One technique employs acousto-optic modulators to shift the carrier frequencies of the pump and probe by tens of megahertz [30]. By interfering the pulses on a fast detector, one can measure the radio frequency beat signal between shifted and unshifted pulses. In this way, the pump and probe can be distinguished, not by their orthogonal polarizations, but by their slightly shifted carrier frequencies. This heterodyne technique allows gain measurements to be performed in waveguides with the pump and probe pulses polarized parallel – as well as perpendicular – to one another. Using an FM detection scheme, one can also measure refractive index nonlinearities with this scheme [31]. This heterodyne measurement technique has been applied to InGaAsP devices at 1.5 μm [30, 32, 31] and recently, to InGaAs devices at 0.9 μm [21]. Another interesting technique is a multiple wavelength pump-probe experiment that has been used to study InGaAs devices at 0.9 μm [19, 20, 21]. Pulses from a Ti:sapphire laser system are spectrally broadened in a short piece of optical fiber. Then, by selecting and compressing different wavelength components one can perform pump-probe measurements with the pump and probe pulses at two separate wavelengths.

To date, all pump-probe measurements on active semiconductor waveguide structures have revealed qualitatively similar dynamics. The dominant ultrafast dynamics that have been observed are attributed to some combination of the following mechanisms: free carrier absorption, two-photon absorption, stimulated transitions, and the optical Stark effect. These processes give rise to ultrafast dynamics such as carrier heating and cooling, spectral hole burning, and an instantaneous refractive index transient. The characteristic size and recovery time for each of these nonlinearities differs somewhat between the various device structures and material systems, but in general, the ultrafast behavior is comparable.

The frequency domain offers an alternate approach to the study of ultrafast nonlinearities in active waveguides. One popular technique is four-wave mixing, which usually employs two CW beams at frequencies f and $f + \Delta f$ [2, 33, 34, 35, 36, 37, 38, 39, 40, 41, 42, 43]. The beams propagate down a waveguide, and through nonlinear interactions, they produce sidebands at $f - \Delta f$ and $f + 2\Delta f$. Measurement of these sidebands reveals information about nonlinearities on a $1/(2\pi\Delta f)$ time scale. By varying Δf, the frequency detuning between the beams, one can extract information about the temporal behavior of the optical nonlinearities.

In theory, the time domain and frequency domain approaches should lead to the same conclusions about ultrafast optical nonlinearities. Four-wave mixing measurements have recently been performed out to frequency detunings of several terahertz, corresponding to a time resolution as fast as 50 femtoseconds [40, 41, 42]. There is fairly good agreement between pump-probe measurements and four-wave mixing measurements. Both show evidence for carrier heating and spectral-hole burning nonlinearities, but some discrepancies between the two approaches remain. The measurements described later on will help to reconcile some of these discrepancies.

The goal of this thesis is to explore in detail the ultrafast gain and refractive index dynamics in an AlGaAs diode laser amplifier. The processes of interest include free carrier absorption, stimulated transitions, spectral hole burning, two-photon absorption, carrier heating and cooling, and the optical Stark effect. Many of these phenomena have been identified in previous pump-probe experiments, but here we hope to study these nonlinearities more fully by characterizing their behavior as a function of carrier density and wavelength. This will result in a better understanding of fundamental processes in semiconductors, and it will allow us to evaluate the potential of active semiconductor waveguides for use in all-optical devices.

1.2 Semiconductor amplifiers

The device of interest in this thesis is an AlGaAs diode laser amplifier – also known as an active waveguide. An active semiconductor waveguide is essentially a semiconductor diode laser with anti-reflection (AR) coatings applied to its two facets. The device does not operate as a laser because the AR coatings eliminate the optical feedback that forms the laser cavity. Instead, the device functions as an optical amplifier, providing gain for photons traveling through the structure. The optical gain – and equivalently, the carrier density in the active region – is set by simply applying a DC bias current to the device. The p-n junction provides for external carrier injection into the active region, and the carriers are confined to the active region by the surrounding higher band gap cladding region. In addition, because of the higher refractive index of the active region as compared to the cladding, the device functions as an optical waveguide.

An active waveguide provides a convenient structure for measuring optical nonlinearities in semiconductors. The long interaction length provided by the waveguide geometry means that nonlinear effects are integrated over the entire length. Compared to a thin-film sample, for example, signals are larger and easier to measure in a waveguide structure. Thus, a waveguide structure enables sensitive measurements of optical nonlinearities.

Moreover, because these structures are *active* waveguides, the carrier density in the device is easily set by varying the externally applied bias current. This ability to set the carrier density is extremely useful because it enables the measurement of how optical nonlinearities vary with carrier density. By varying the carrier density *and* tuning the pulse wavelength, one can investigate optical nonlinearities in an active waveguide over a large parameter space. This is a powerful way to characterize optical nonlinearities and to identify the physical processes that give rise to these nonlinearities.

Another benefit, of a practical nature, is that active waveguides are readily adaptable for use in all-optical devices. For instance, a strong optical nonlinearity in a waveguide structure could become the basis for an all-optical switching device. Instead of having to infer the performance of a proposed device from the response measured in a thin-film sample, the behavior exhibited by active waveguides is immediately applicable to devices. Other benefits include helping to understand the operation of and reveal limitations to diode laser modelocking and high frequency diode laser modulation. Thus, it is of practical interest to study optical nonlinearities in a waveguide structure since the results can have a direct impact on devices with similar structures.

To motivate the practical side of the measurements described in this thesis, we give examples of three devices which employ active waveguides. The first device shown in Fig. 1.1 is a traveling wave optical amplifier [44, 45, 46, 47, 48, 49]. This is

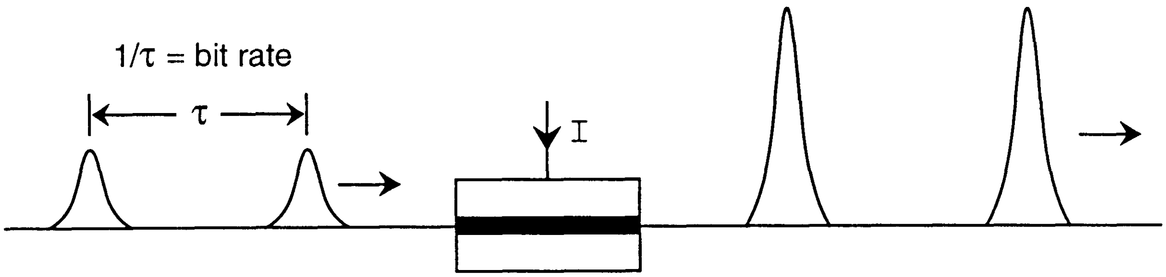

Figure 1.1: Semiconductor diode laser amplifier. Injected current I provides optical gain for light that travels through the waveguide structure.

just an active waveguide structure with optical gain provided by carrier injection. For such a device, it is important that pulses are amplified without introducing significant distortions. For example, temporal broadening and spectral shifts must be kept to a minimum.

Whereas optical amplifiers need to exhibit linear behavior, the next two devices we describe require highly nonlinear behavior. The first device, shown in Fig. 1.2, employs an active waveguide as the nonlinear switching element in a demultiplexer [50]. The control pulses induce π phase shifts in a nonlinear waveguide that sits in one arm of a fiber interferometer. Every other data slot of the input data stream is switched into one of two output data streams. Thus, the bit rate is reduced by a factor of 2; this could be done to allow for electronic processing of the data. This device requires an optically induced π phase shift that does not also induce significant long-term phase shifts and is not accompanied by absorptive nonlinearities.

Finally, the wavelength converter shown in Fig. 1.3 is used to shift the wavelength of an optical signal [51, 52]. Four-wave mixing between the signal and a CW pump results in the generation of a sideband that duplicates the input signal. A spectral filter selects the sideband, and the same input signal emerges at the output shifted in wavelength. This device would be useful in wavelength-division multiplexed systems where the ability to convert and recycle wavelengths enables the design of complex networks. Also, since the wavelength converter acts as a phase conjugator, the spectrum of the output signal is the inverse of the input signal - this is shown schematically in the figure. Thus, a wavelength converter can also be used to compensate for dispersion

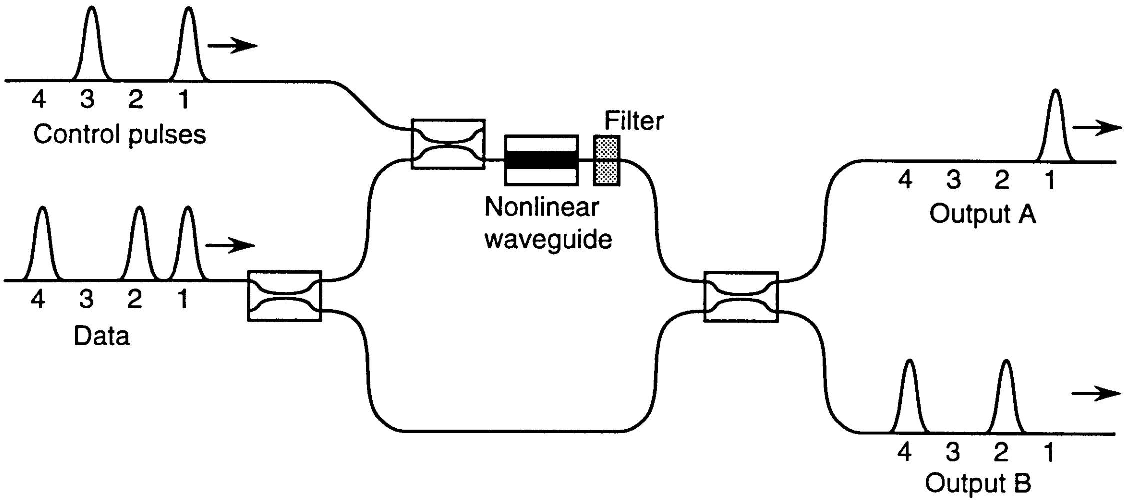

Figure 1.2: All-optical demultiplexer. The active waveguide functions as a nonlinear switching element in a fiber interferometer. Control pulses induce periodic π phase shifts that switch the input data stream into two output data streams.

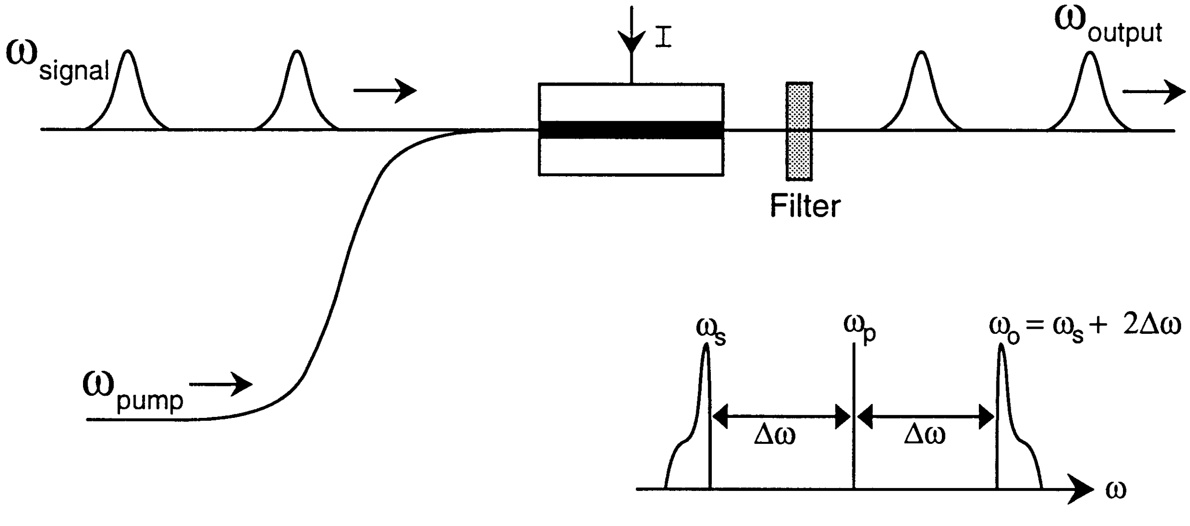

Figure 1.3: Wavelength converter. Through four-wave mixing in an active waveguide, an input bit stream is shifted in frequency.

in fiber communication systems [53, 54, 55].

As yet, none of these devices has been made into a commercial product, but there have been experimental demonstrations of both optical amplifiers [44, 45, 46, 47, 48, 49] and wavelength converters [51, 52, 54, 55]. As the demand grows for higher bit rate systems, these devices may be developed into products. And although the development of an all-optical computer is probably not a realistic expectation, hybrid optical and electronic systems are certainly feasible. Optics may never match electronics as far as cost and integration density goes, but the speed of all-optical devices could find application as the bridge between electronic processing and optical communication. Optoelectronic devices could be valuable for board-to-board or chip-to-chip communication, or at the transmitting and receiving ends of fiber communication networks. The measurements to be described later on will hopefully shed some light on the feasibility of devices that employ active semiconductor waveguides. Or, at least this research will reveal important issues that could limit the performance of such devices. In any case, the results will have relevance to the development of future practical all-optical devices.

1.3 Overview of experiments

The past several years have seen a mini-revolution in ultrafast optics brought about by the invention of the modelocked titanium:sapphire (Ti:sapphire) laser [56, 57, 58]. And just as active waveguides are convenient structures for studying optical nonlinearities in semiconductors, the Ti:sapphire laser is the ideal tool for performing these studies. This laser system can produce pulses shorter than 100 femtoseconds over a wavelength range from 750 to 1000 nanometers. Furthermore, the Ti:sapphire laser is inherently stable and reliable because of its all solid-state make-up. This makes it far superior to modelocked dye lasers, the competing source for sub-picosecond pulses in this wavelength range. Over just a few years, the modelocked Ti:sapphire laser, with its remarkable stability and wide tuning range, has become the pulse source of choice for many researchers. The enhanced capability afforded by Ti:sapphire lasers has allowed new measurements that were not possible five years ago to be performed. In addition, older experiments are also being repeated with Ti:sapphire lasers, yielding new and interesting results.

This thesis is concerned with ultrafast optical nonlinearities in AlGaAs and their

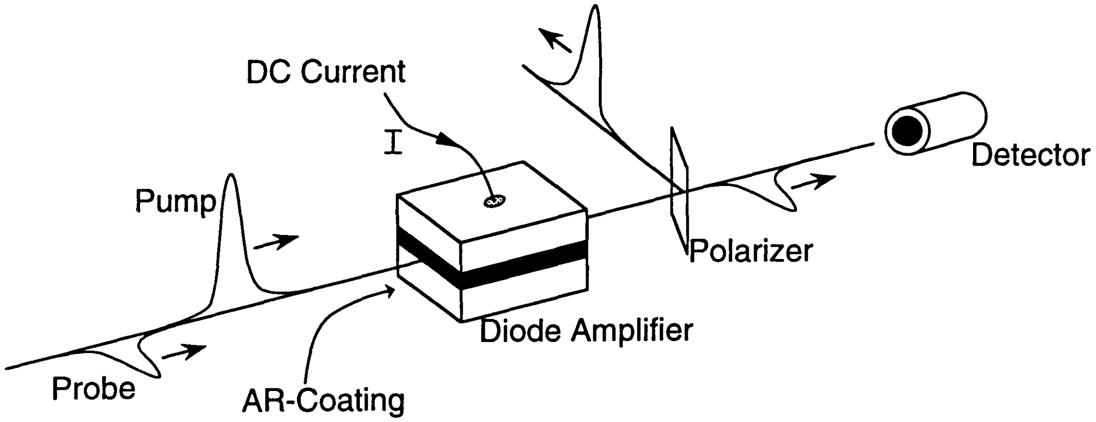

Figure 1.4: Schematic of pump-probe measurement technique in an active waveguide.

variation with wavelength and carrier density. The Ti:sapphire laser system allows the resolution of dynamics on a 100 femtosecond time scale. In addition, the broad wavelength tunability of the Ti:sapphire laser enables measurements of optical nonlinearities below and above the band edge of AlGaAs materials and devices.

Briefly, we now outline the pump-probe experimental technique employed in this thesis. A pump-probe technique is used to measure time-resolved absorptive and refractive index dynamics in a bulk AlGaAs active waveguide. Fig. 1.4 is a schematic that shows the essentials of pump-probe measurements in active waveguides. A stream of pulses from the Ti:sapphire laser is split into two pulse streams. One is designated the pump pulse, while the other has its polarization rotated by 90 degrees and is called the probe pulse. The pump and probe pulses are coupled through the waveguide. The pump pulse perturbs the sample, and the probe senses this pump-induced change in the absorption and the refractive index. After traveling through the waveguide, the pump is filtered out with a polarizer, and we measure the power or the phase of the probe pulse.

By measuring the probe power (or phase) as a function of the temporal delay between the pump and probe pulses, we can map out the absorptive (or refractive index) dynamics that the pump induces in the waveguide. Here, we are concerned with dynamics on a picosecond time scale – or pump-probe delays on the order of millimeters. The time delay between the pump and probe pulses is obtained with a computer-controlled micron-precision delay stage. Note that since the pulses coming out of the Ti:sapphire laser system are separated in time by 12 nanoseconds, the pump-induced perturbation of the waveguide is fully recovered between successive pump-probe pulse pairs.

These time-resolved measurements of gain and index response can be performed at various pump-probe wavelengths and at various carrier densities. From such measurements, one can learn a great deal about fundamental carrier dynamics in semiconductors. A summary of the optical processes in semiconductors that these measurements are concerned with appears in Fig. 1.5. Absorption of photons by free electrons or free holes promotes carriers high up into the band. These energetic carriers interact with the sea of free carriers at the bottom of the band causing them to heat up. As the warm carriers emit phonons, they cool back to their equilibrium temperature on a picosecond time scale.

Stimulated emission and absorption of photons lead to a variety of effects: carrier density changes which persist for long times ($\sim$nanosecond); spectral hole burning which recovers quickly ($\sim$100 femtoseconds) as carriers collide and scatter into empty states; and carrier heating and cooling. Note that stimulated density changes can heat or cool the carriers depending on whether carriers are removed or added and whether these carriers have energies greater than or less than the average energy of the distribution. For instance, putting electrons into the conduction band with energies less than the average energy of the electron distribution will result in a cooling of the electrons. None of these effects occurs when we excite the semiconductor with below-band light. Thus, below-band excitation is a convenient way to turn off the dynamics associated with stimulated transitions.

Two-photon absorption causes carrier density changes and carrier heating. And finally, the optical Stark effect is an electronic nonlinearity that causes shifting of the electronic states when the semiconductor is excited by an electromagnetic field. As we shall see, this shifting of states causes a large instantaneous refractive index nonlinearity.

This thesis will describe one set of experiments performed with pulses tuned to photon energies above the band gap energy of the AlGaAs active region. The other set of measurements involves pulses tuned below the band edge. The below-band measurements allow us to isolate the three effects – free carrier absorption, two-photon absorption, and the optical Stark effect – in the absence of stimulated transition effects. Both sets of measurements will be performed as a function of wavelength and carrier density. From these measurements we will pull out numbers for the nonlinear

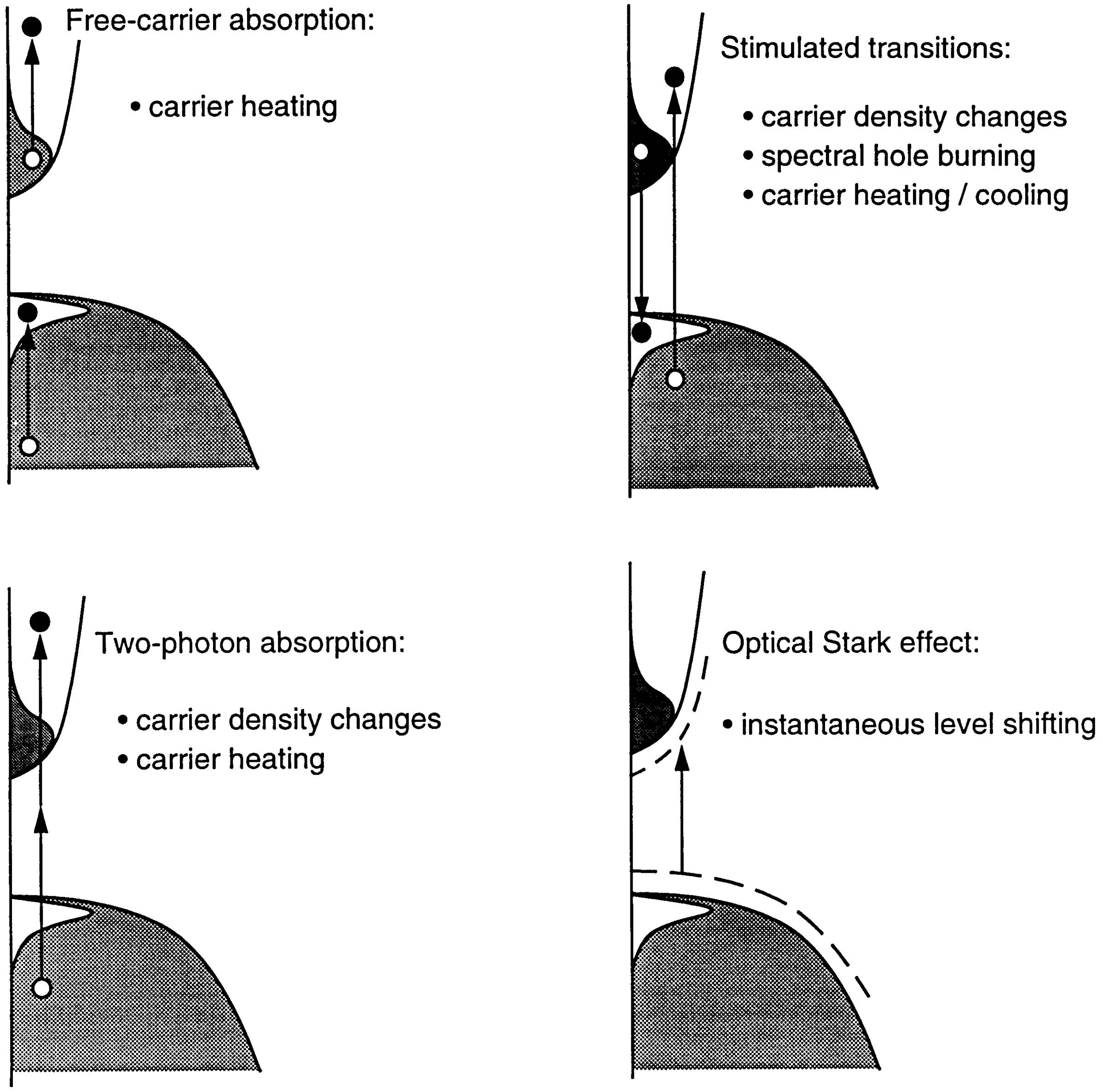

Figure 1.5: Schematic of optical processes in semiconductors and the effects they produce: Free carrier absorption, stimulated emission and absorption, two-photon absorption, and the optical Stark effect.

refractive index coefficient n_2 that goes into the expression $n = n_0 + n_2 I$. Other issues that will be addressed include the effect of chirped pulses on the measured pump-probe response, the variation of the pump-probe response with increasing pump power, and cooling of the carriers through stimulated absorption.

1.4 Thesis outline

The next chapter covers some preliminaries that will be referred to throughout this thesis. The short pulse laser system, the AlGaAs diode laser amplifier and its optical modes, and gain and index in semiconductors will be discussed. Then, in Chapter 3 we will describe the pump-probe measurement technique that allows measurement of ultrafast gain and refractive index dynamics in the AlGaAs active waveguide. One important topic is an artifact in the refractive index measurement that is caused by pulse chirp. The three chapters that follow deal with an assortment of experimental gain and refractive index measurements. Chapter 4 describes above- and below-band pump-probe measurements. Then, Chapter 5 takes an in-depth look at the transparency point, an interesting operating point for above-band measurements. Finally, Chapter 6 details additional results that include power-dependent measurements, carrier cooling through stimulated absorption, and spectrally-resolved measurements. In Chapter 7 we analyze and discuss the results of the previous three experimental chapters. In particular, values for the nonlinear refractive index coefficient n_2 associated with the various refractive index dynamics are derived from the data. Then, we discuss the results obtained here and compare our results to other pump-probe and four-wave mixing measurements. In the concluding chapter, we detail the prospects for future all-optical devices containing active semiconductor waveguides, and we outline possible experiments to be performed in the future.

Chapter 2

Preliminaries

This chapter presents an assortment of topics that will help us to interpret and understand the experiments described later on. The first section describes the short pulse laser system used to perform the pump-probe measurements. Then, the AlGaAs diode laser studied in this thesis is detailed. In particular, we present computations and measurements of the optical mode profile that propagates in the AlGaAs diode laser waveguide. Finally, optical gain and refractive index in semiconductors are examined with particular attention to how carrier density and carrier temperature changes affect the gain and refractive index. The preliminaries discussed in this chapter will be referred to throughout this thesis.

2.1 Ti:Sapphire laser system

The pump-probe technique is a popular method for observing ultrafast processes in materials. The key to performing such measurements is a stable and reliable source of ultrashort optical pulses. In the past, most pump-probe experiments required an inordinate amount of time tweaking, aligning, and cajoling the laser system into an acceptable mode of behavior. The recent development of modelocked Ti:sapphire lasers [56, 57, 58] has fortunately helped to alleviate some of this laser misery for people performing experiments in the 700 to 1,000 nanometer wavelength range.

With commercial Ti:sapphire laser systems widely available, one can concentrate on performing experiments instead of endlessly aligning the laser system. Indeed, now it is not necessary to be a laser expert to perform short pulse measurements. This has opened up the use of ultrashort pulses to researchers in other fields like chemistry, materials science, and biology. In addition, the reliability and broad tunability offered by Ti:sapphire lasers make possible experiments that were previously not practical to perform with older laser systems. This is not to say that Ti:sapphire lasers are flawless. Indeed, they have their own set of endearing mysteries and idiosyncrasies, but overall their performance is a great improvement over older systems such as actively modelocked dye lasers.

The measurements described in this thesis employ a modelocked Ti:sapphire laser system. The operation of modelocked Ti:sapphire lasers is now fairly well understood [58], and their performance has been optimized to the point where pulses as short as 11 femtoseconds have been obtained directly out of a Ti:sapphire laser [59, 60]. Here, we will present a brief overview of the Ti:sapphire laser used in this work. The active medium for a Ti:sapphire laser is titanium ions embedded in a sapphire host crystal. The Ti^{3+} ions absorb blue-green light and emit light from about 700 to 1100 nanometers wavelength. The blue-green pump light was provided by a CW argon laser which was generally operated at 8 to 10 watts output power. The first generation of Ti:sapphire laser used in this work was a home-built system that used a saturable absorber dye jet to help start and maintain pulsed operation. This system was useful, but the dye jet made the system slightly unstable and also limited the extent of wavelength tunability. The later measurements were performed with a commercial Tsunami Ti:sapphire laser made by Spectra-Physics. The all solid-state makeup of this system resulted in improved performance and long-term stability which was essential for some of the measurements presented here. In addition, the system was wavelength tunable from 780 to 940 nanometers, allowing the measurement of optical nonlinearities over a broad wavelength range.

Fig. 2.1 shows a schematic of the Spectra-Physics Tsunami Ti:sapphire laser system. Typically, the laser system produces 1.5 watts of average power. The repetition rate is 82 MHz; so the energy per pulse directly out of the laser is about 18 nanojoules. The pulse duration was typically between 80 and 120 femtoseconds (measured in terms of the full-width at half maximum – FWHM – of the intensity). This indicates a peak power for each pulse of 0.18 megawatts. A typical experiment employs about 50 μW of average pump power (0.6 pJ per pulse; 6 watts peak power). Focusing this to a spot 2 microns in diameter corresponds to a peak intensity of about 200 MW/cm^2. One can see that short optical pulses are invaluable to performing nonlinear optics measurements because large peak powers and intensities can be produced with only moderate average powers. Thus, one can induce large nonlinearities in materials without causing thermal damage.

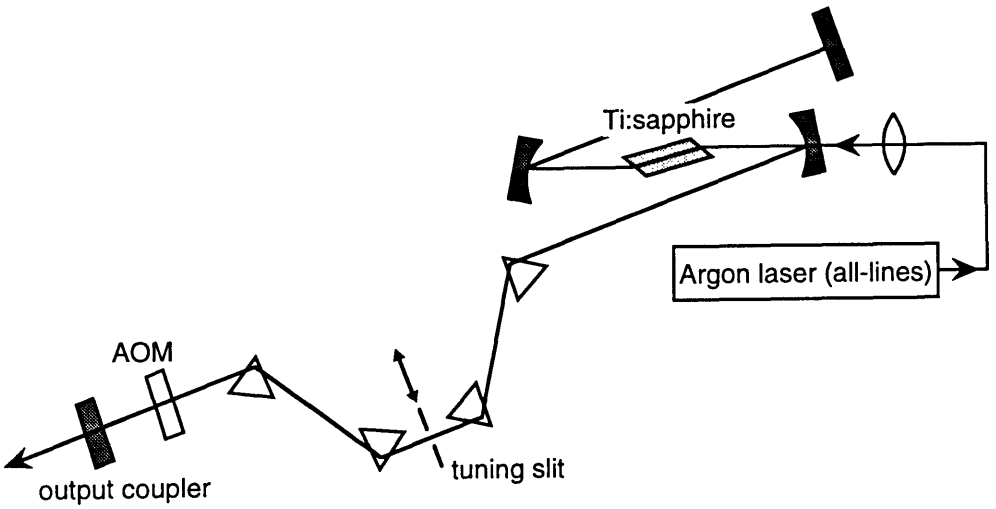

Figure 2.1: Schematic of Ti:sapphire laser system. The argon laser pumps the Ti:sapphire rod; the four prisms provide dispersion compensation; the tuning slit allows for wavelength selection; and the acousto-optic modulator (AOM) helps to start and maintain pulsed operation.

Most modelocked Ti:sapphire laser systems have certain common features: a mechanism for starting and maintaining pulsed operation, some method for tuning the wavelength, and a means to adjust the dispersion of the cavity. Referring to Fig. 2.1, the argon laser pumps the Ti:sapphire rod which sits in a fold in the cavity. The acousto-optic modulator (AOM) acts like a shutter which opens in sync with the pulse oscillating in the laser cavity. The AOM helps to start and maintain the pulsed operation of the laser. The tuning slit that sits between the prisms allows the laser wavelength to be tuned. By translating the slit back and forth one can select the desired wavelength of operation. The four prisms provide for adjustment of the laser cavity dispersion. Optimizing the cavity dispersion is important for achieving stable pulsed operation. The amount of dispersion encountered by the pulses in the cavity can be varied by moving the two middle prisms in and out of the beam path.

The theory of modelocked operation of a Ti:sapphire laser involves a process known as Kerr lens modelocking (KLM) [58]. KLM is the mechanism that causes the laser to favor pulsed operation over CW operation. The AOM helps to get the pulsing started, but the KLM action is the key to the generation of short, stable pulses. Here we present a simple physical picture of the KLM process. Generally, the KLM action takes place in the Ti:sapphire rod. The argon pump laser is focused in the Ti:sapphire rod a little tighter than is optimum for CW operation. When the laser operates in a pulsed mode, the high-intensity pulses induce an increase in the refractive index of the sapphire rod through the Kerr effect. This higher refractive index causes the mode to self-focus – that is, an effective lens is formed through the Kerr effect. Since pulses traveling through the rod are focused more tightly than the CW mode, the pulses see higher gain because the argon laser is focused to match this tighter mode. Thus, pulsed operation experiences a higher gain and is therefore favored over CW operation. One important issue is how the laser initially gets started pulsing. This initial push is provided by the AOM which forms pulses that have enough peak intensity to induce a Kerr lens in the Ti:sapphire rod. At this point the KLM process takes over, and the AOM is not needed. However, to ensure that the pulses do not drop out, the AOM is usually left on for long-term stability.

In order to monitor and analyze the performance of the laser system, two diagnostics are employed. An autocorrelator is used to monitor the temporal characteristics of the pulses, while a spectrometer looks at the spectrum of the pulses. Both help in optimizing the performance of the laser system to minimize noise and wavelength shifting. Fig. 2.2 shows a typical pulse autocorrelation and pulse spectrum.

An autocorrelator is formed by splitting a beam of pulses into two beams, mechanically delaying one beam with respect to the other, recombining them, and focusing them into a second-harmonic crystal such as lithium-iodate. When the two pulses are not coincident in time, no second-harmonic light is generated. As the two pulses are overlapped in time, more and more second-harmonic light is generated. By measuring the amount of second-harmonic light as a function of time delay between the two beams, one can generate the pulse autocorrelation function:

$$G^{(2)}(t) = \int_{-\infty}^{\infty} d\tau \, I(\tau) \cdot I(t+\tau) \, . \tag{2.1}$$

This is what is shown in the top plot of Fig. 2.2. Notice that the autocorrelation function is symmetric, and thus, some information about the pulse shape is lost. Still, autocorrelations are useful diagnostics. By assuming a pulse shape, one can pull out the pulse width from the measured autocorrelation function. For Ti:sapphire lasers, the pulse intensity is generally assumed to have a $\mathrm{sech}^2(t)$ shape. For a $\mathrm{sech}^2(t)$ pulse, the ratio of the autocorrelation FWHM to the intensity FWHM is 1.54. Then, the 139 femtosecond width of the pulse autocorrelation in Fig. 2.2 corresponds to a

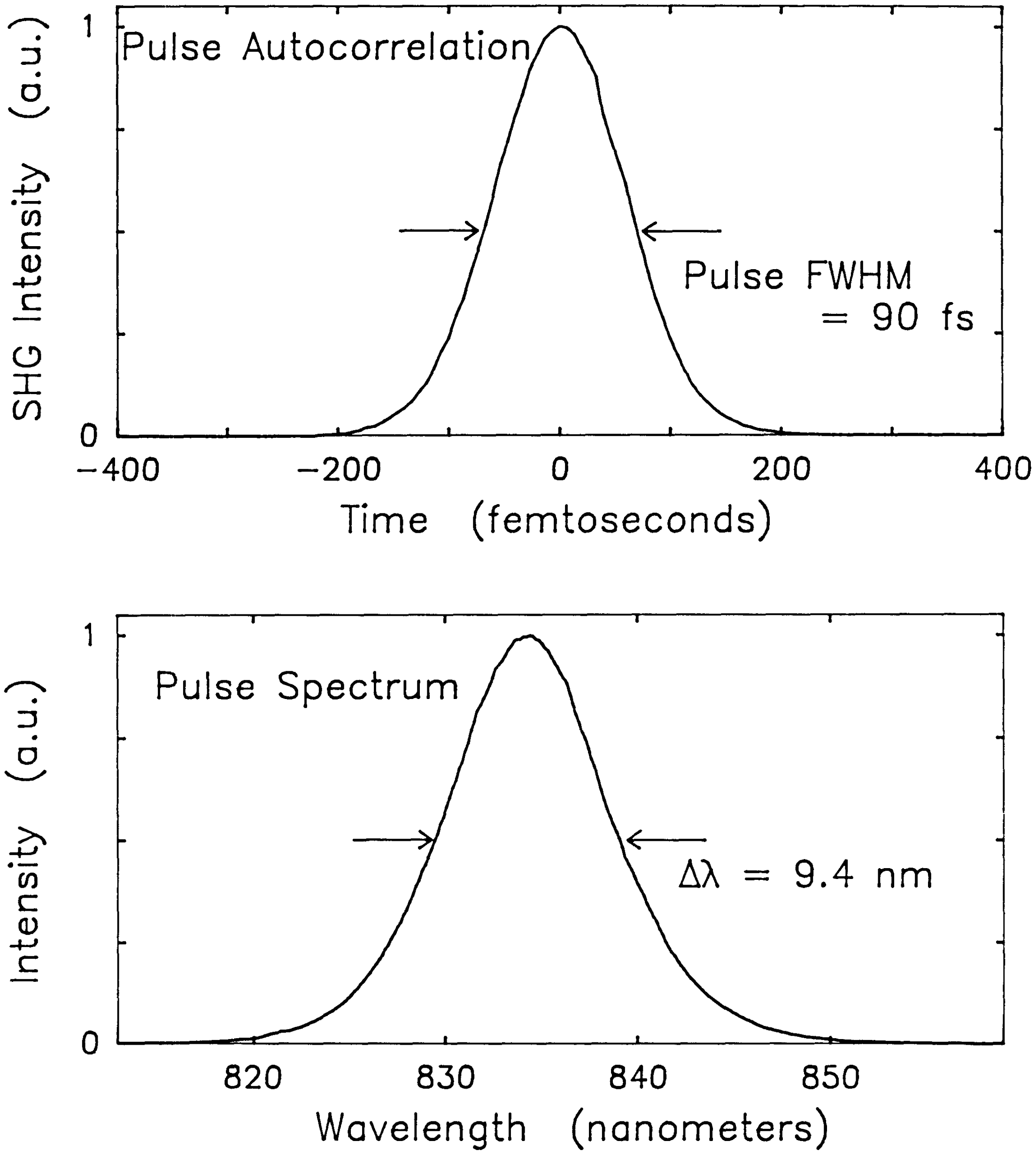

Figure 2.2: Typical autocorrelation and spectrum of pulses from the Ti:sapphire laser. The pulses have a full-width at half maximum (FWHM) of 90 femtoseconds, and the spectral width is 9.4 nanometers.

pulse intensity width of 90 femtoseconds.

An important relation between pulse width ($\Delta\tau$) and spectral width ($\Delta\nu$) can be obtained from the Fourier transform relations. Again assuming a $\mathrm{sech}^2(t)$ intensity pulse profile, we obtain $\Delta\tau \cdot \Delta\nu \geq 0.315$. When the time-bandwidth product equals 0.315, the pulse is said to be transform-limited. Otherwise, the pulse is chirped, or non-transform-limited. Transform-limited pulses are generally better behaved and more desirable for performing experiments. The pulses in Fig. 2.2 have a time-bandwidth product of 0.36, and so they are 14% over transform limit. They are chirped because some glass between the laser and the autocorrelator broadened the pulses slightly. In performing experiments, the pulse autocorrelation was monitored at the point just before the pulses were coupled into the diode laser amplifier. Using a set of dispersion compensating prisms between the laser and the experiment, the prism insertion could be varied until the pulse duration was minimized. This ensured that the pulses used in the measurements had a minimum amount of chirp. Also, by intentionally chirping the pulses with these prisms, the effect of pulse chirp on the measured pump-probe signal could be studied. The results of this investigation will be presented in the next chapter.

2.2 Diode laser amplifier

This section describes the diode laser amplifier that was studied in this thesis. After a look at the device structure, the optical mode that propagates through the device will be characterized. The waveguide supports two orthogonally-polarized modes, and of particular concern is how the mode profile varies with wavelength and polarization. This information will be used later on when values for n_2, the nonlinear refractive index coefficient, are calculated. A description of the procedure for determining n_2 from the measured refractive index dynamics is given at the end of this section.

2.2.1 Device structure and description

The device that was studied in this thesis is a bulk AlGaAs diode laser made by Hitachi (part no. HLP1400). A schematic of the 300-μm long diode laser is shown in Fig. 2.3. The active region is made of bulk $\mathrm{Al_{0.05}Ga_{0.95}As}$ with $\mathrm{Al_{0.35}Ga_{0.65}As}$ cladding layers. The device is a channeled-substrate planar (CSP) structure – this refers to the 1.2 by 5 μm channel that helps to confine the optical mode in the direction parallel

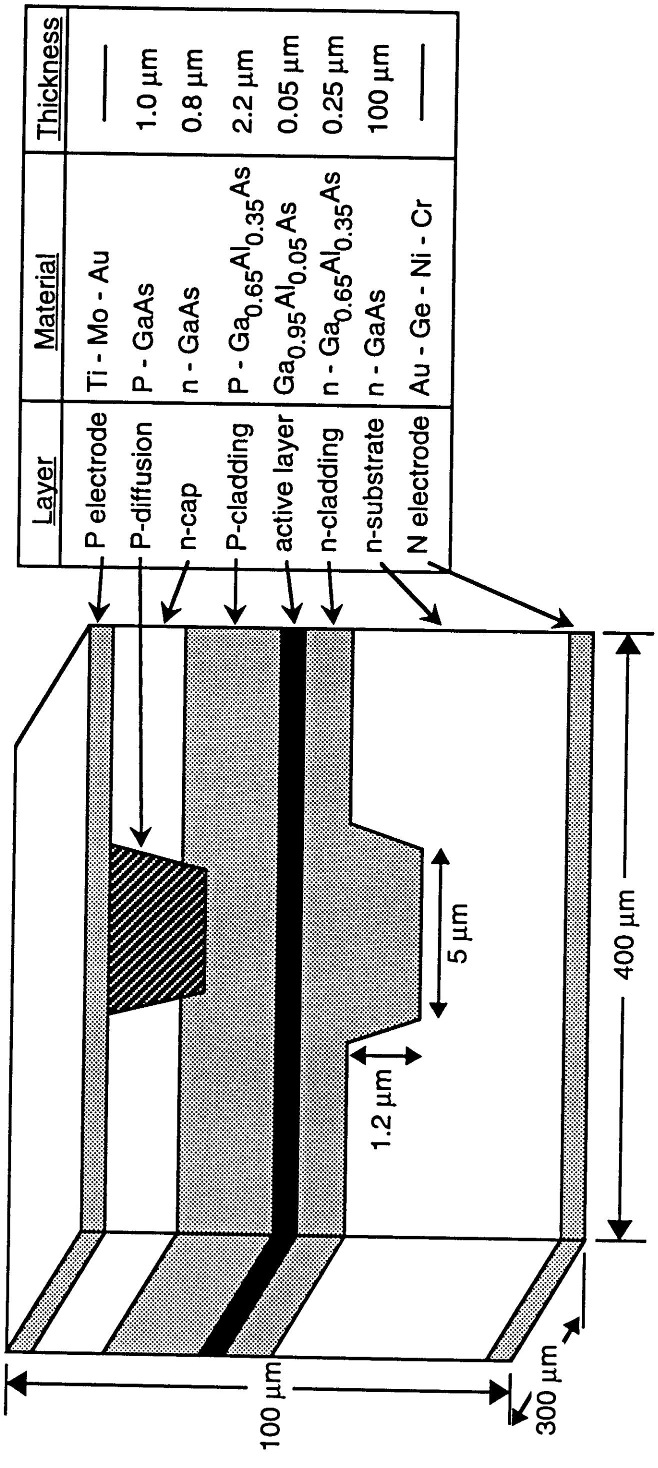

Layer	Material	Thickness
P electrode	Ti - Mo - Au	—
P-diffusion	P - GaAs	1.0 μm
n-cap	n - GaAs	0.8 μm
P-cladding	P - $Ga_{0.65}Al_{0.35}As$	2.2 μm
active layer	$Ga_{0.95}Al_{0.05}As$	0.05 μm
n-cladding	n - $Ga_{0.65}Al_{0.35}As$	0.25 μm
n-substrate	n - GaAs	100 μm
N electrode	Au - Ge - Ni - Cr	—

Figure 2.3: Schematic of the Hitachi HLP1400 AlGaAs diode laser. The device is a channeled-substrate planar (CSP) structure. The active region is bulk AlGaAs, and the device is 300 μm long.

to the layers [61]. The *p-n* junction provides for injection of electrons and holes into the active region, and the higher band gap cladding layers confine the carriers to the active region. The higher refractive index of the active region with respect to the cladding also provides for optical confinement in the vertical direction. In the horizontal direction, optical confinement results from a mixture of gain guiding and index guiding.

These diode lasers have a threshold current around 50 mA and operate at about 830 nanometers wavelength. With 80 mA of bias current, the diode laser typically produces 7 mW of power. The device is mounted out in the open with the front and rear facets accessible to allow light to be coupled into and out of the waveguide. Several diode lasers were used over the course of the experiments described in this work. However, for a given set of measurements a single device was generally used for consistency.

The devices studied in this work were made to function as diode laser amplifiers rather than as diode lasers. This was accomplished by depositing anti-reflection (AR) coatings on the front and rear facets of the diode laser [62]. The reflectivity of the facets was then reduced from ~30% to below 0.1%, causing the diode laser threshold current to increase by about two times. Reducing the reflectivity of the facets suppresses the lasing action of the device for currents below 100 mA, and the device then functions as an optical amplifier. Light can be amplified while traveling through the active waveguide structure, depending on the wavelength of the light and the bias current applied to the diode laser amplifier.

AR-coatings allow the device to be operated at a desired bias current without the diode laser producing significant amounts of light that would interfere with a measurement. Then, experiments can be performed as a function of carrier density by simply changing the bias current applied to the AR-coated diode laser. So, in this work the diode laser amplifier functions not so much as an optical amplifier but rather as an active waveguide that allows easy tuning of the carrier density. The AR-coatings are also useful because they eliminate pulses that reflect off the end facets and propagate back through the waveguide. These pulse echoes can generate spurious, unwanted pump-probe signals in addition to the signal produced by the primary pulses. With an AR-coating, this pulse echo effect is eliminated making the data cleaner and easier to interpret.

One problem encountered with the diode lasers used in this work was their short lifetimes. Some devices gave out after less than 100 hours of operation, and a lifetime of 200 hours was considered good. Still, this is well below the 1,000 hour lifetime specified for these diode lasers. The degradation in performance was characterized by a gradual decrease in spontaneous emission light emitted by the device, and occasionally, a distortion or darkening of parts of the output mode.

The rapid degradation of the devices is not fully understood, but three issues are probably important. First, the devices were operated at room temperature mounted on a heat sink but with no active cooling element used. Thus, thermally induced damage may contribute to the degradation process. If this were the case, a thermoelectric cooler might help to increase the lifetime. Second, the high intensity of the pulses in the waveguide (up to 200 MW/cm^2) could induce optical damage or defect generation. Finally, the AR-coating process may have a hand in the early demise of the devices. Before the AR-coating is applied to the facets, the protective passivation layer of SiO_2 is removed. This removal process may cause some damage to the device. Or, the AR-coating may be less resistant than the passivation layer to harmful agents such as water vapor. Several generations of AR-coatings were deposited on devices, and each coating involved a slightly different recipe. As these recipes improved over time, the device lifetimes also improved, suggesting that a good AR-coating can help the devices last longer. Still, the same degradation process was occasionally observed in devices that had not been AR-coated. This suggests that the AR-coating is not the only culprit, but rather it may be a combination of the above three items.

2.2.2 Waveguide modes

One of the goals of this thesis is to quantify nonlinear optical processes in AlGaAs. For instance, we would like to measure the nonlinear refractive index coefficient n_2 of AlGaAs to enable quantitative comparisons with other materials and devices. To measure n_2 we need to know the intensity profile of the optical mode in the waveguide. With this in mind, this section gives an overview of measurements and computations that were performed to characterize the shape of the optical modes in the active waveguide. The pump-probe measurements described later on are performed at a series of wavelengths, and so, here the modal shapes are computed as a function of wavelength in the 800 to 900 nanometer range.

The modal intensity profile was computed using the effective index method [61, 63, 64]. Briefly, the waveguide is treated as layers of dielectric with known thickness and refractive index. By applying the electromagnetic boundary conditions at each dielectric interface, an eigenvalue equation is obtained. Solving this equation yields the propagation constant $\beta = n_{\text{eff}}k$, where $k = 2\pi/\lambda$ and n_{eff} is the effective index, or the modal refractive index. Once the effective index is known, the mode shape is easily computed – generally, the mode is cosinusoidal in the active region and decays exponentially in the cladding. The waveguide supports two orthogonal modes – the TE mode is polarized parallel to the layers (horizontally), and the TM mode is polarized perpendicular to the layers (vertically). Since the refractive index varies with wavelength, the mode shape will also vary with wavelength. Therefore, the modes are computed versus wavelength with the wavelength-dependent refractive index of AlGaAs obtained from published measurements [64, 65, 66, 67].

It is fairly easy to compute the mode profile in the direction perpendicular to the layers using the effective index method. However, in the direction parallel to the layers the mode is confined by a combination of gain and index guiding, including contributions from thermally induced index changes. It is more difficult to compute the mode in this direction because the index profile becomes complex and convergence problems then arise in solving with the effective index method.

Fig. 2.4 shows modal intensity profiles at 830 nanometers computed using the effective index method. In the direction perpendicular to the layers ($\perp$), the mode is confined by the index difference between the active region and the surrounding cladding. Notice that since the active region is very narrow, only a small fraction of the mode overlaps the active region while the rest spills over into the cladding. The TM mode (polarized vertically, or perpendicular to the layers) is less confined than the TE mode (polarized horizontally, or parallel to the layers). When the device operates as a laser, it operates in the TE mode partly because the gain is higher for the TE mode. However, light can propagate through the waveguide in either the TE or the TM mode. In the parallel direction ($\|$), the active region is fairly wide and so the mode is almost completely contained within the 4 μm-wide active region. Also, the TE and TM modes are nearly identical in the parallel direction.

In order to confirm the accuracy of these mode computations, the far-field mode patterns were measured using a slit, a protractor, and a detector positioned a few inches away from the device. Since the diode laser only operates in the TE mode, light from the Ti:sapphire laser was coupled through the waveguide to generate both TE and TM modes. The measured far-field mode patterns perpendicular ($\perp$) and

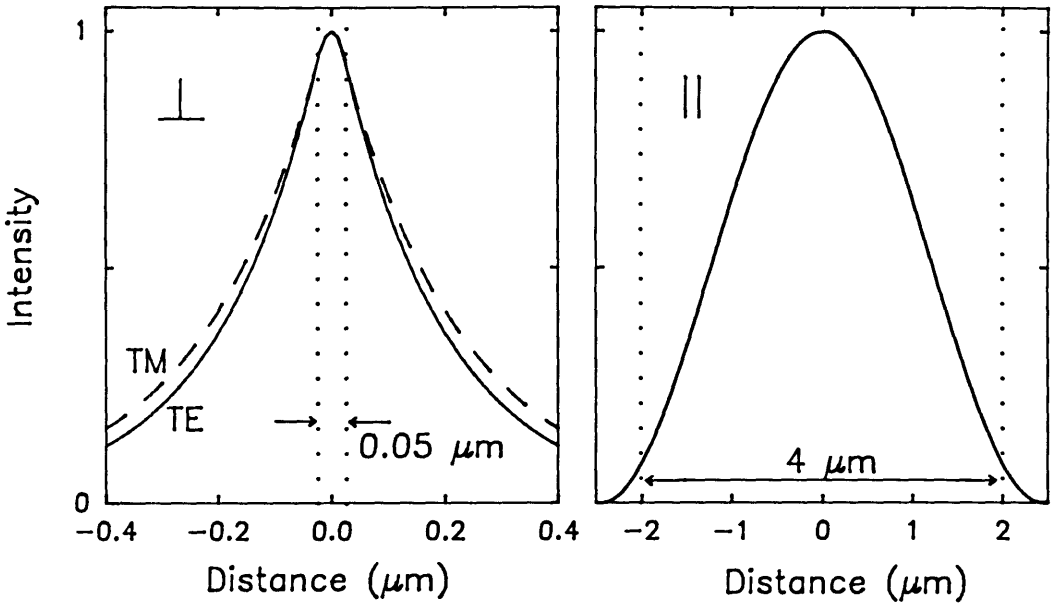

Figure 2.4: Computed modal intensity profiles perpendicular (⊥) and parallel (||) to the waveguide layers at 830 nanometers for the HLP1400 diode laser. The dotted vertical lines indicate the boundaries of the active region. The solid line indicates the TE mode (polarized horizontally – parallel to the waveguide layers), and the dashed line indicates the TM mode (polarized vertically).

parallel (||) to the layers are shown in the upper part of Fig. 2.5. Not surprisingly, it was also found that the TE-polarized light that was coupled through the waveguide exhibits the same far-field mode pattern as the light emitted by the laser diode.

The computed modes shown in the lower part of Fig. 2.5 were found by applying a far-field diffraction formula from Casey and Panish [64] to the waveguide modes from Fig. 2.4. In the perpendicular direction, the TE mode diverges slightly more than the TM mode. This is expected since the TE mode is more tightly confined than the TM mode in the waveguide and thus it diverges more rapidly. In the parallel direction, the TE and TM modes are almost identical, in agreement with the waveguide mode computations. Overall, the computed and measured far-field modes are in good agreement, indicating that the waveguide mode profiles computed with the effective index method are fairly accurate.

Next, we investigate the wavelength dependence of the mode profiles. One way to characterize waveguide modes is with Γ, the confinement factor, defined as the fraction of total power that overlaps the active region. Another way to characterize

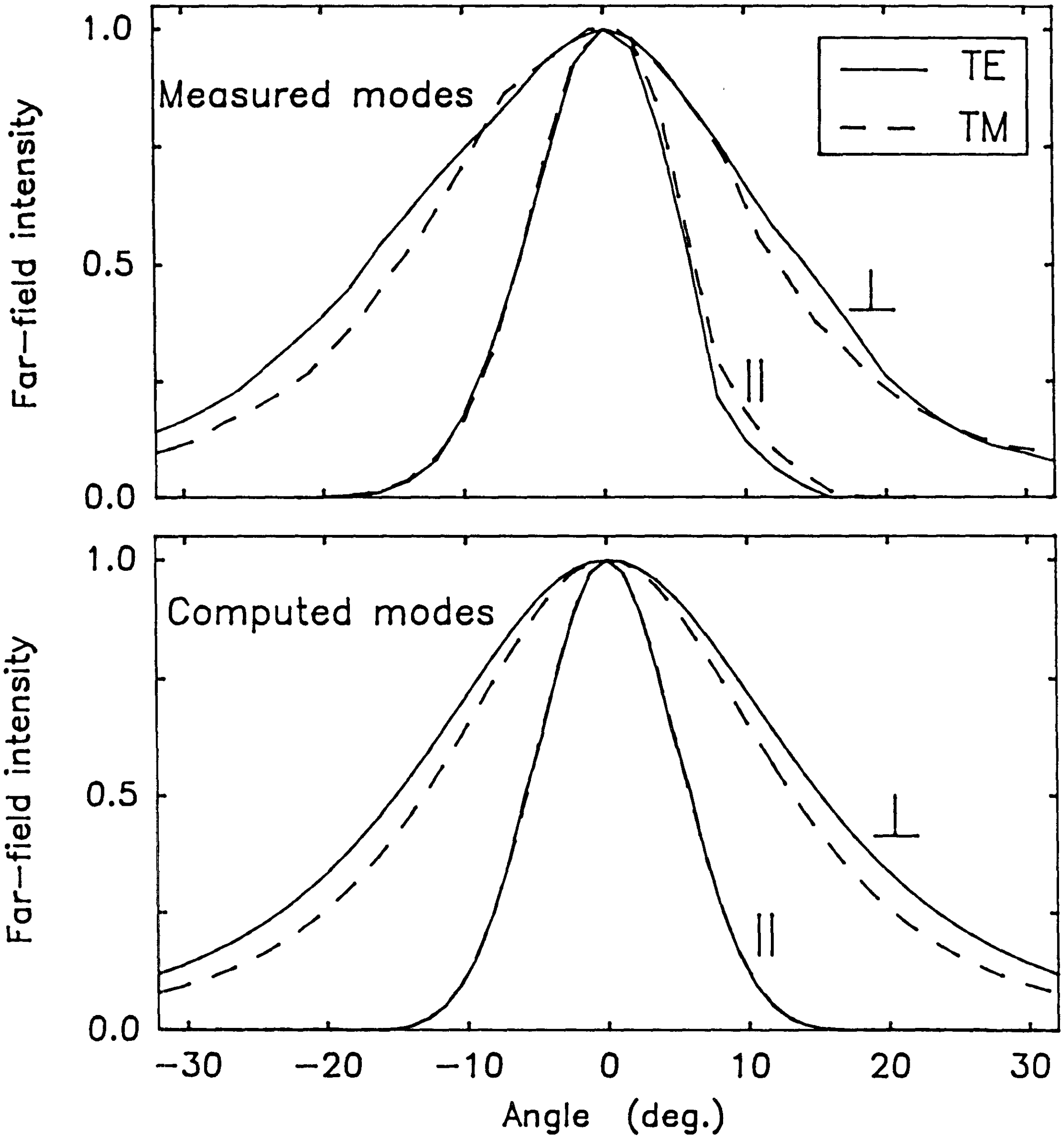

Figure 2.5: Measured and computed far-field mode patterns at 830 nanometers for the HLP1400 diode laser. The modes are shown parallel (||) and perpendicular ($\perp$) to the waveguide layers. The solid line indicates the TE mode, and the dashed line indicates the TM mode.

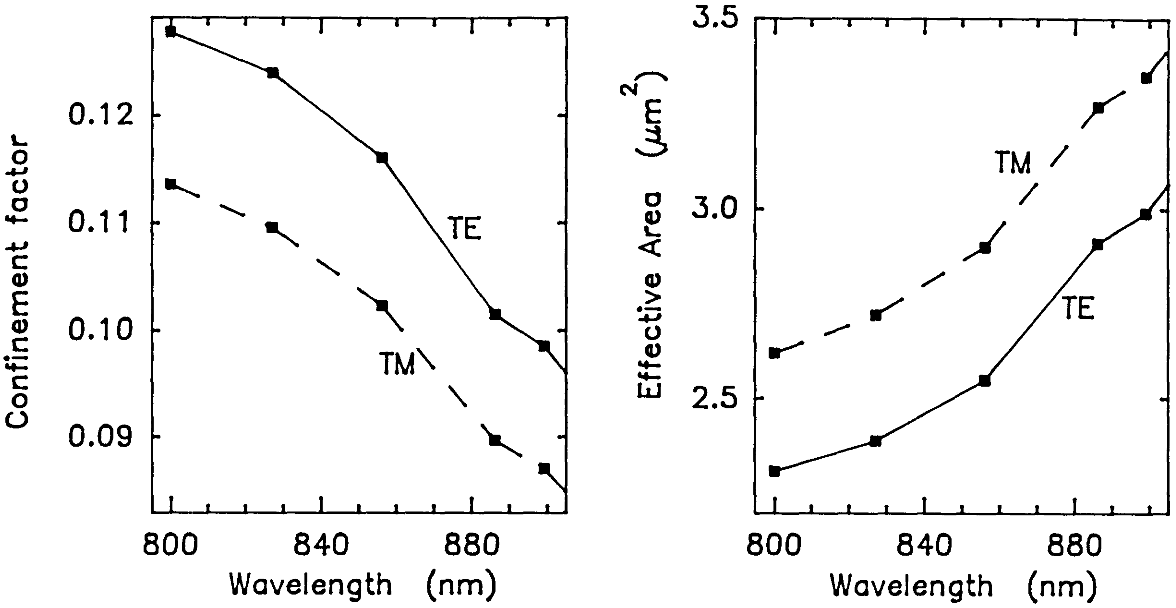

Figure 2.6: Computed confinement factor and effective area as a function of wavelength. The solid curve is for the TE mode, and the dashed curve is for the TM mode.

waveguide modes is with A_{eff}, the effective area, which is defined as [68, 69]

$$A_{\text{eff}} = \frac{\left[\int\int dx\, dy\, I(x,y)\right]^2}{\int\int dx\, dy\, I^2(x,y)}, \tag{2.2}$$

where $I(x,y)$ is the modal intensity profile. Given the refractive index of AlGaAs as a function of wavelength [64, 65, 66, 67], we can perform the mode computations as described above. From this, we can pull out the confinement factor and effective area for the diode laser amplifier modes as a function of wavelength and polarization. The results of this exercise are shown in Fig. 2.6.

The curves are slightly jagged because the refractive index of AlGaAs is not well known around the band edge, and so values for the refractive index were interpolated from published data. Notice that the confinement factor is in the neighborhood of 10%, showing that for this device most of the energy in a mode is actually contained *outside* the active region. In general, the TE mode is better confined than the TM mode, and so, the TE mode has a larger confinement factor and a smaller effective area. As we go to longer wavelengths, the modes become less and less confined. This is caused by the refractive index difference between the active region and the cladding becoming smaller as the wavelength increases. Additionally, the increasing ratio of wavelength to active region dimension (λ/d, where $d = 0.05\,\mu$m) also contributes to the decreasing confinement at longer wavelengths. Beyond about 910 nanometers, it was seen experimentally that the mode is not well-guided and starts to fall apart.

2.2.3 Computing modal and material index nonlinearities

Having characterized the optical mode that propagates through the waveguide, we now outline the method for determining n_2, the intensity dependence of the refractive index that goes into the expression $n = n_0 + n_2 I$. Specifically, the effective area A_{eff} is used to compute an effective intensity I_{eff} that is in turn used to find n_2. Later on in Chapter 7, the method described here will be applied to the measured refractive index data and values for n_2 will be determined as a function of wavelength and carrier density.

Assume a pump pulse with peak power P_{peak} induces a peak index change Δn in a material. In a pump-probe experiment, we measure the resulting phase shift of the probe pulse $\Delta\phi$. The index change and phase shift are related by $\Delta\phi/2\pi = \Delta n L/\lambda$, where L is the waveguide length. Given the pump intensity I, we can find n_2 from $\Delta n = n_2 I$. If the transverse mode profile were constant, we could find the pump intensity from $I = P_{\text{peak}}/A$, where A is the modal area. However, the mode profile is not flat, and so, as we now explain, the effective area must be introduced.

The refractive index change measured in a pump-probe experiment is the weighted average of the pump-induced index change across the transverse extent of the waveguide:

$$\Delta n = \frac{\int\int dx\, dy\, I(x,y)\, \Delta n(x,y)}{\int\int dx\, dy\, I(x,y)}\,. \tag{2.3}$$

For simplicity, the pump and probe are assumed to have the same modal intensity profiles $I(x,y)$. Assuming an instantaneous response, the spatially varying index change induced by the pump can be written $\Delta n(x,y) = n_2\, I(x,y)$, and Eq. (2.3) becomes

$$\Delta n = n_2 \frac{\int\int dx\, dy\, I^2(x,y)}{\int\int dx\, dy\, I(x,y)}\,. \tag{2.4}$$

Then, multiplying the top and bottom of this equation by the expression for peak pump power $P_{\text{peak}} = \int\int dx\, dy\, I(x,y)$, we obtain

$$\Delta n = n_2\, P_{\text{peak}} \frac{\int\int dx\, dy\, I^2(x,y)}{[\int\int dx\, dy\, I(x,y)]^2} = \frac{n_2\, P_{\text{peak}}}{A_{\text{eff}}} = n_2\, I_{\text{eff}} \,. \qquad (2.5)$$

So, to summarize, given a pump-induced phase shift of the probe pulse $\Delta\phi$, the nonlinear refractive index coefficient n_2 is found from

$$\Delta\phi = \left[\frac{2\pi L}{\lambda}\right] \Delta n = \left[\frac{2\pi L}{\lambda}\right] \frac{n_2\, P_{\text{peak}}}{A_{\text{eff}}} = \left[\frac{2\pi L}{\lambda}\right] n_2\, I_{\text{eff}} \,. \qquad (2.6)$$

The n_2 obtained from this method is the *modal* n_2. That is, the Δn measured in a pump-probe experiment is the change in modal refractive index, or effective index, induced by the pump. The effective index is like a weighted average of the refractive index taken over the modal profile of the waveguide. In the pump-probe measurements in these active waveguide devices, the dominant pump-induced index change occurs in the active region with little contribution from the cladding. Thus, the modal index change that we measure arises predominantly from the index change in the active region. Then, the amount of index change seen by the probe pulse is reduced approximately by the confinement factor. A waveguide with a confinement factor near unity can exhibit a large modal n_2 even though the strength of the underlying nonlinearity is relatively weak. And, as is the case with the device studied here, a waveguide with a small confinement factor may exhibit a small modal n_2 although the nonlinearity is strong. Thus, the modal n_2 is structure dependent. Given a specific waveguide structure, knowing the modal n_2 is important for designing a device based on that particular structure. However, the modal n_2 does not enable comparisons to be made between various materials and structures.

If one is interested in studying the characteristics of a nonlinear process apart from the device structure, then the parameter of interest is the *material* n_2. This is the nonlinear index coefficient of a given material, exclusive of device structure effects. To find the material n_2 for the active waveguides used here, we need to know the relation between Δn_{active} and $\Delta n_{\text{effective}}$. Then, given a measured modal refractive index change ($\Delta n_{\text{effective}}$), we can find Δn_{active}, the size of the index change in the active region that caused this modal index change. And knowing the modal profile, we can then compute the n_2 of the AlGaAs material independent of any structural

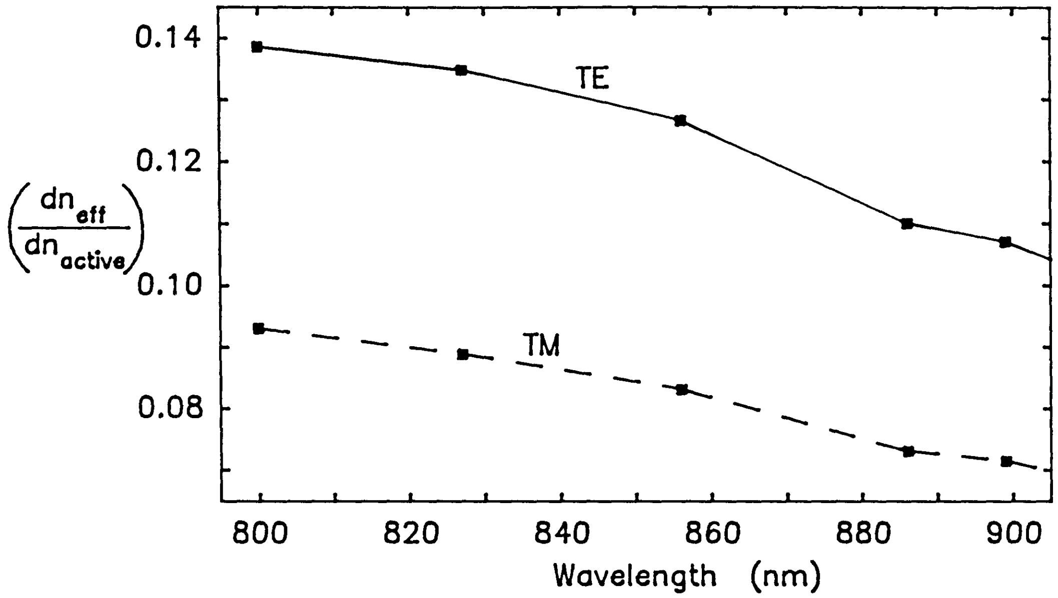

Figure 2.7: Calculated change in the modal refractive index with respect to a change in the active region refractive index plotted as a function of wavelength. The solid curve is for the TE mode and the dashed curve is for the TM mode.

effects. Given the relatively small confinement factor of the devices used in this work, we expect a large change in the active region refractive index to induce a relatively small change in the modal refractive index. Indeed, this what we find, and the results are plotted in Fig. 2.7. These results were obtained by the effective index method described in the previous section. Notice that the sensitivity of the effective index to changes in the active region index is smaller for the TM mode because the TM mode is less confined than the TE mode.

One thing to note is that when we calculate n_2 we assume all of the nonlinear refractive index change occurs in the active region with no contribution from the cladding. This is not strictly true, but in our case the assumption is a good one. In general, the nonlinearities we measure are enhanced as one approaches the band edge. For the measurements described later on the pulse wavelength is usually tuned no more than 80 meV away from the band edge of the active region. And in the case of the cladding, we are generally over 370 meV away from the band edge. Since the processes are resonant with the band edge, we are safe in neglecting the small contribution of the cladding to the material n_2.

2.3 Gain and index in semiconductors

The measurements described later on are concerned with gain and refractive index nonlinearities in AlGaAs. As a starting point for analyzing these measurements, it is important to have an understanding of the basic gain and refractive index properties of semiconductors. In particular, we wish to explore how the gain and refractive index are affected by changes in the carrier density or carrier temperature. The next section describes calculations of the optical gain spectrum of a semiconductor. The effects of carrier density and carrier temperature changes are calculated. Then, the refractive index response to a change in carrier density and carrier temperature is calculated. The computations presented here are based on elementary models of semiconductor band structure, but they serve as useful points of reference when analyzing the experimental results later on.

2.3.1 Gain in AlGaAs

We now compute the optical gain in AlGaAs, paying special attention to the effects of carrier density and carrier temperature. An expression for the gain spectrum is derived, following the approach of Casey and Panish [64] and Lasher and Stern [70]. We apply this expression to a simple parabolic band model and numerically compute the gain spectrum of AlGaAs for various carrier densities and temperatures.

First, consider a system containing two electronic levels, E_2 and E_1, separated by energy $E_{21} = E_2 - E_1$. The probability that the upper level E_2 is occupied by an electron is f_c. The probability the lower level E_1 is occupied is f_v. Here, f_c and f_v are numbers; later, for a semiconductor, they become functions of energy and temperature. A photon of energy $E_{21} = \hbar\omega$ can stimulate an electron transition from E_2 to E_1. This process is called stimulated emission and generates an additional photon. The rate of stimulated emission (transitions/sec-cm^3) is

$$r_{21} = B_{21} \, f_c \, (1 - f_v) \, P(E_{21}) \, , \tag{2.7}$$

where B_{21} is the transition probability (sec^{-1}) and depends on the strength of coupling between the two states by the electromagnetic field. $P(E_{21})$ is the density of photons with energy E_{21}. A photon of energy E_{21} can also stimulate an electron transition from E_1 to E_2. This is stimulated absorption, and a photon is absorbed in this process. The rate of stimulated absorption is

$$r_{12} \;=\; B_{12}\, f_v\, (1 - f_c)\, P(E_{21})\,. \tag{2.8}$$

From thermal equilibrium considerations, B_{12} and B_{21} must be equal [71]. The net stimulated emission rate, the difference between the rates of stimulated emission and stimulated absorption, is then:

$$r_{\text{net}} \;=\; r_{21} - r_{12} \;=\; B_{12}\, (f_c - f_v)\, P(E_{21})\,. \tag{2.9}$$

The gain (cm^{-1}) for this two-level system is the net stimulated emission rate divided by the photon flux (photons/sec-cm^2):

$$g(E_{21}) \;=\; \frac{r_{\text{net}}}{P(E_{21})\, v_g} \;=\; \frac{B_{12}\, (f_c - f_v)}{c/n}\,, \tag{2.10}$$

where $v_g \;=\; c/n$ is the group velocity, and n is the refractive index of the material. Note that in order for the gain to be positive, f_c must be greater than f_v. That is, the upper level occupation probability must be greater than the lower level occupation probability. In a semiconductor, this leads to the Bernard-Duraffourg condition for stimulated emission [64, 72].

From Fermi's "Golden Rule" [64, 71], the transition probability is

$$B_{12} \;=\; \frac{\pi e^2 \hbar}{m^2 \epsilon_0 n^2 E_{21}}\, |M|^2\,, \tag{2.11}$$

where e is the electron charge, $\hbar$ is Planck's constant, m is the electron mass, ϵ_0 is the permittivity constant, and M is the momentum matrix element. M describes the strength of coupling between the upper and lower state wave functions by the electromagnetic field. Finally, the gain for a two-level system can be written

$$g(E_{21}) \;=\; \frac{\pi e^2 \hbar}{\epsilon_0 m^2 c n E_{21}}\, |M|^2\, (f_c - f_v)\,. \tag{2.12}$$

In a semiconductor such as AlGaAs, we no longer have a simple two-level system. Instead, we have a distribution of states described by ρ, the density of states, and f, the Fermi function. Fig. 2.8 illustrates the optical gain process in a semiconductor. The electron and hole densities of states are represented by ρ_c and ρ_v, respectively. Multiplying the density of states ρ by the Fermi function f gives the distribution of carriers in energy. Assuming parabolic bands, the conduction band (upper level) density of states is

$$\rho_c(E - E_c) \;=\; \frac{1}{2\pi^2}\left(2m_c/\hbar^2\right)^{3/2}(E - E_c)^{1/2}\,, \tag{2.13}$$

and the valence band (lower level) density of states is

$$\rho_v(E_v - E) \;=\; \frac{1}{2\pi^2}\left(2m_v/\hbar^2\right)^{3/2}(E_v - E)^{1/2}\,. \tag{2.14}$$

E_c is the energy of the conduction band edge, and E_v is the energy of the valence band edge. m_c is the effective mass of electrons in the conduction band, and m_v is the effective mass of electrons in the valence band.

The probability that a conduction band state at a given energy E_2 is occupied (by an electron) is given by the Fermi function:

$$f_c(E_2, T_e) \;=\; \frac{1}{1 + e^{(E_2 - \mu_e)/kT_e}}\,, \tag{2.15}$$

where μ_e is the quasi-Fermi energy for the electrons and T_e is the temperature of the electrons in the conduction band. The probability that a valence band state at energy E_1 is occupied (by an electron) is

$$f_v(E_1, T_h) \;=\; \frac{1}{1 + e^{(E_1 - \mu_h)/kT_h}}\,, \tag{2.16}$$

where μ_h is the quasi-Fermi energy for the holes and T_h is the temperature of the hole distribution. The occupation probability for holes in the valence band is then $1 - f_v$.

Given the electron density N and temperature T_e, the electron quasi-Fermi energy can be computed from the relation

$$N \;=\; \int_{-\infty}^{\infty} \rho_c(E - E_c)\, f_c(E, T_e)\, dE\,. \tag{2.17}$$

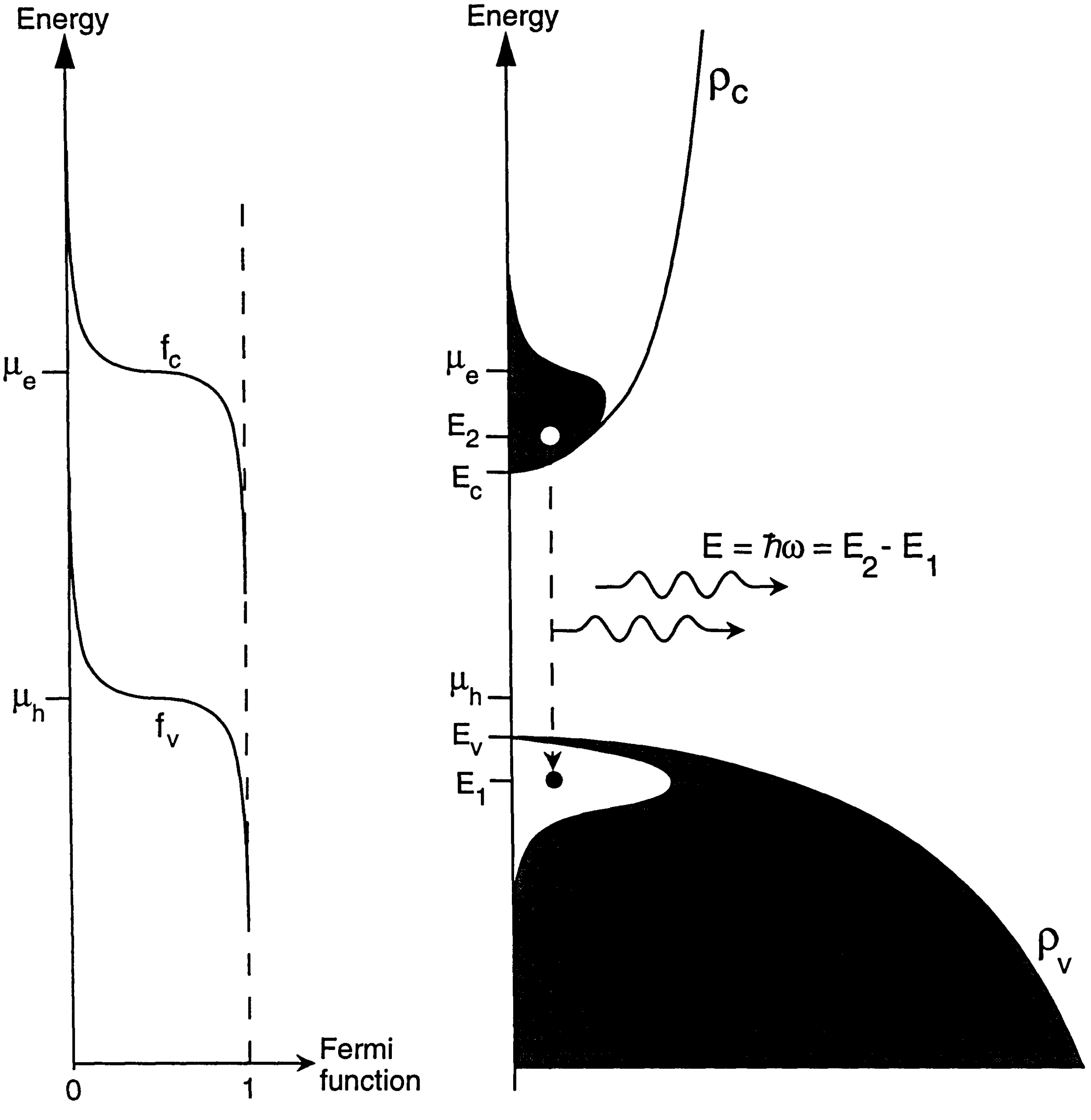

Figure 2.8: Optical gain in a semiconductor. A photon of energy E stimulates the recombination of an electron and hole and the emission of another photon of the same energy. The electron and hole distributions are obtained by the product of the density of states $\rho(E)$ and the Fermi function $f(E)$.

This integral is just the area of the shaded region in the conduction band from Fig. 2.8. Similarly, μ_h can be found from the corresponding relation for holes:

$$P = \int_{-\infty}^{\infty} \rho_v(E_v - E)\,[1 - f_v(E, T_h)]\, dE \;, \tag{2.18}$$

where P is the hole density. Likewise, this integral is the area of the white region in the valence band from Fig. 2.8.

The gain is found by applying the two-level gain expression of Eq. (2.12) to the electron and hole densities of states in Eqs. (2.13) and (2.14), respectively. Then, to find the gain at a given photon energy E, Eq. (2.12) is summed over all energy levels separated by E. So, the gain in a direct gap semiconductor is written

$$g(E) = \frac{\pi e^2 \hbar}{\epsilon_0 m_c m_v c n E} \int_{-\infty}^{\infty} |M|^2\, \rho_v(E_1)\, \rho_c(E_1 + E)\, [f_c(E_1 + E) - f_v(E_1)]\, dE_1 \;. \tag{2.19}$$

E_1 is the energy of a state in the valence band. E_2 $(= E_1 + E)$ is the energy of a state in the conduction band. f_c is the probability that the conduction band state is occupied by an electron, and f_v is the probability that the valence band state is occupied by an electron. For photon energies less than the energy gap ($E < E_g$), the gain is zero, since the electron and hole densities of states vanish in the band gap.

As discussed earlier, the condition for positive gain is that $f_c > f_v$. From this we can derive the Bernard-Duraffourg condition for stimulated emission in a semiconductor: $(\mu_e - \mu_h) > E$ [64, 72]. In other words, for positive gain, the energy difference between the electron and hole quasi-Fermi levels must be greater than the photon energy E. For photon energies greater than the Fermi level separation, the gain is negative (the semiconductor is absorptive).

Given an electron density and temperature, μ_e can be computed through iteration of Eq. (2.17). Similarly, given a hole density and temperature, μ_h can be computed from Eq. (2.18). Then, numerically evaluating Eq. (2.19) at a series of above band gap photon energies gives the gain spectrum. A typical gain spectrum that results from this process is shown in Fig. 2.9. Below the band gap energy E_g the gain is zero and so the semiconductor is transparent. Photons with energy just above the band edge experience positive gain. Here, the gain regime extends for about 65 meV above the band edge. The transition from positive to negative gain occurs at the

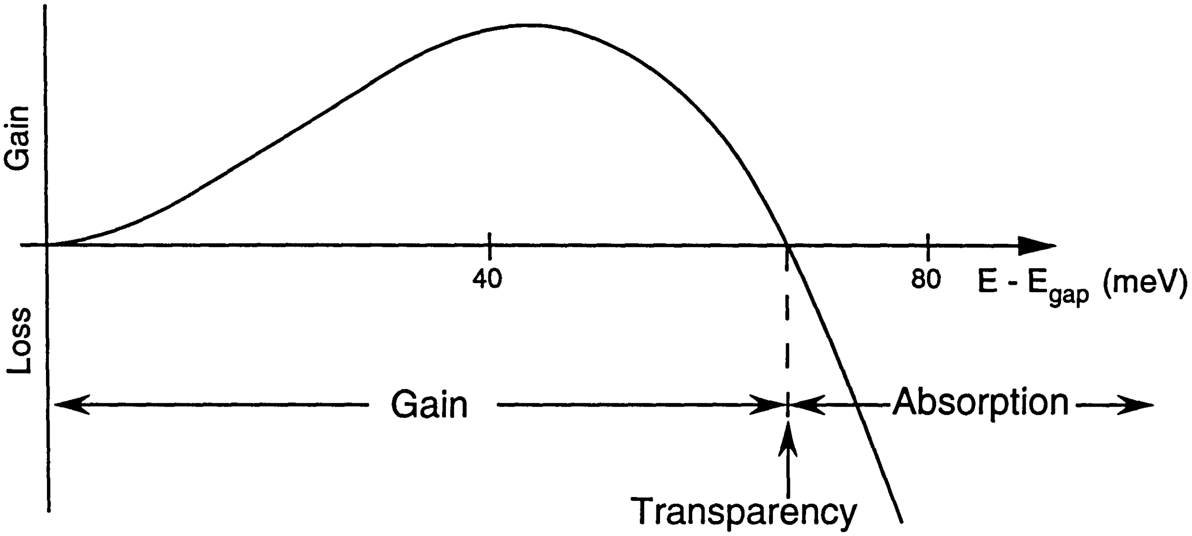

Figure 2.9: Typical semiconductor gain spectrum. The gain regime extends about 65 meV above the band edge, and after that, absorption dominates. Between the two regimes sits the transparency point.

transparency point. Photons at this energy see no net gain – no net carrier density changes occur, and the medium appears transparent. From the Bernard-Duraffourg condition, the transparency point occurs for a photon energy equal to the quasi-Fermi level separation ($\mu_e - \mu_h$). Beyond the transparency point, the gain falls to negative values. This is called the absorption regime of the semiconductor. Pulses with photons in this regime experience net loss.

The gain integral in Eq. (2.19) is taken over all states in the conduction and valence bands that are separated by the photon energy E. To account for momentum conservation, the integral should only be taken over those states having the same momentum. However, this restriction is relaxed for states near the band edge due to the high density of carriers and their strong coupling. For states higher up in the band, momentum conservation cannot be neglected. This work is concerned with the behavior of gain and refractive index just above the band edge. Thus, we can neglect momentum conservation, keeping in mind that the results obtained are not necessarily valid for energies high above the band gap energy.

To apply the gain computations to $Al_{0.05}Ga_{0.95}As$, the band gap is set to E_g = 1.49 eV, and we use a refractive index n = 3.6. We assume parabolic bands and assign a constant mass to the electrons and holes. The electron mass is $m_c = 0.067m_0$, where m_0 is the free electron mass. The heavy and light holes are treated together with a composite mass $m_v = 0.47m_0$, The split-off valence band is ignored. We do not include the effects of bandtailing – the existence of states below the band edge due to shallow dopants or impurities. Finally, the electron and hole density and temperature are set to the same values.

Fig. 2.10 shows the computed gain spectra for AlGaAs at four different carrier densities with the electron and hole carrier temperatures fixed at 300 K. As one would expect, an increase in carrier density results in an increase in gain for all above-band energies. Increasing the carrier density increases the bandwidth of the gain regime and pushes the transparency point out to higher energies.

Fig. 2.11 shows computed gain spectra for AlGaAs at three different carrier temperatures with the carrier densities fixed at 2.5×10^{18} cm^{-3}. Increasing the carrier temperature causes a gain compression in all three regimes of operation – gain, transparency, and absorption. Heating the carriers smears out the carrier distribution in energy, which results in a decrease in the optical gain. It turns out that for energies several hundred meV above the band edge, however, carrier heating actually causes an *increase* in the optical gain. The reason for this is that heating the carriers increases the occupation of high energy states far above the band edge. As a result, far above the band edge the optical gain increases – actually, since these energies are far into the absorption regime, one should say that the optical absorption decreases. In any case, the turning point in energy where carrier heating induces this reduction in optical absorption occurs so far into the absorption regime that this effect would be very difficult to observe. Since the measurements described here are performed near the band gap energy, we can conclude that carrier heating causes a uniform gain decrease across the optical gain spectrum.

Just to gain some further insight into how temperature changes affect the carriers, Fig. 2.12 shows the electron and hole distributions at two temperatures. In general, the electrons are more spread out in energy than the holes because of the lower density of states for electrons. Both the electrons and hole distributions become more smeared out in energy when the carrier temperature is increased.

Finally, we ask what happens to the Fermi energy and the average energy of the carrier distributions as a function of carrier density. These issues are important when we consider the effects of stimulated transitions on the temperature of the carriers.

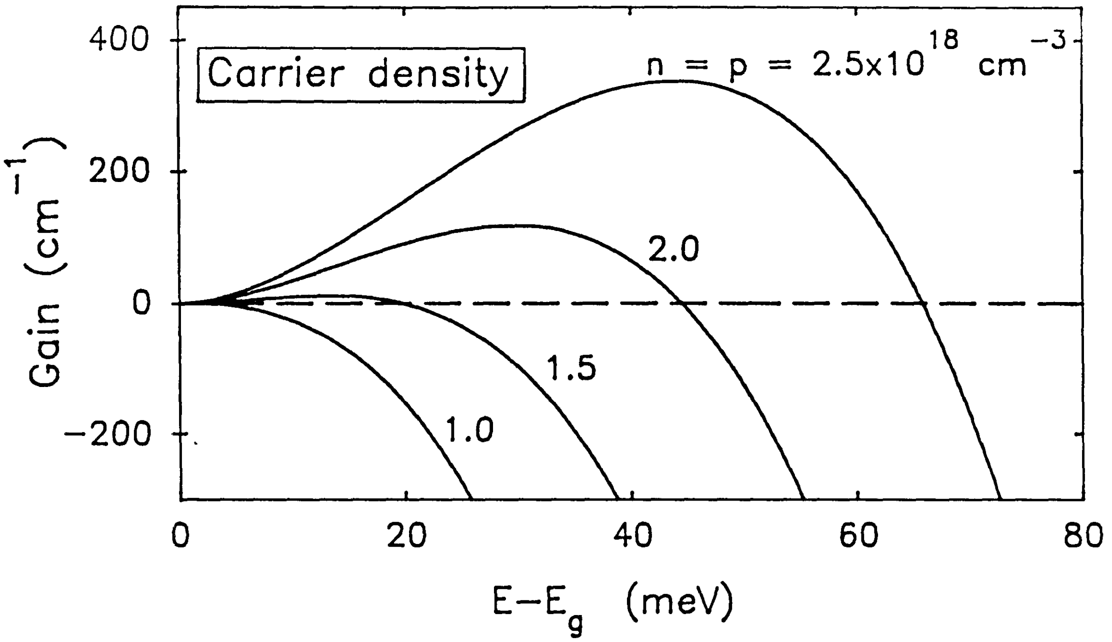

Figure 2.10: Gain curves for AlGaAs at various carrier densities. The electron and hole temperatures are fixed at 300 K.

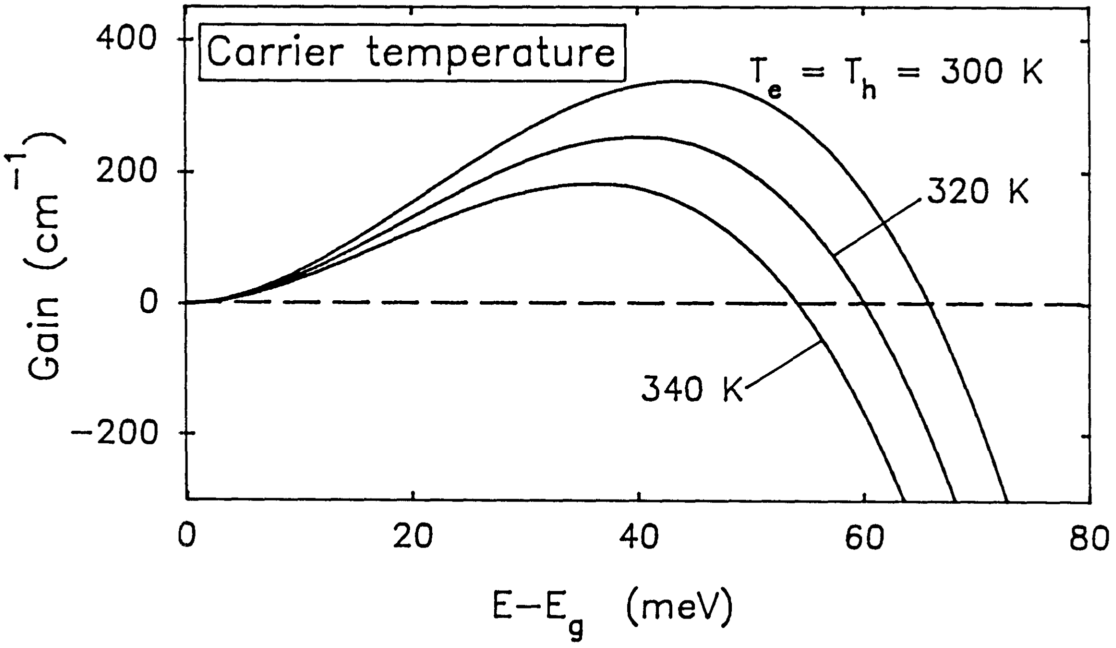

Figure 2.11: Gain curves for AlGaAs at various carrier temperatures. The electron and hole carrier densities are fixed at 2.5×10^{18} cm^{-3}.

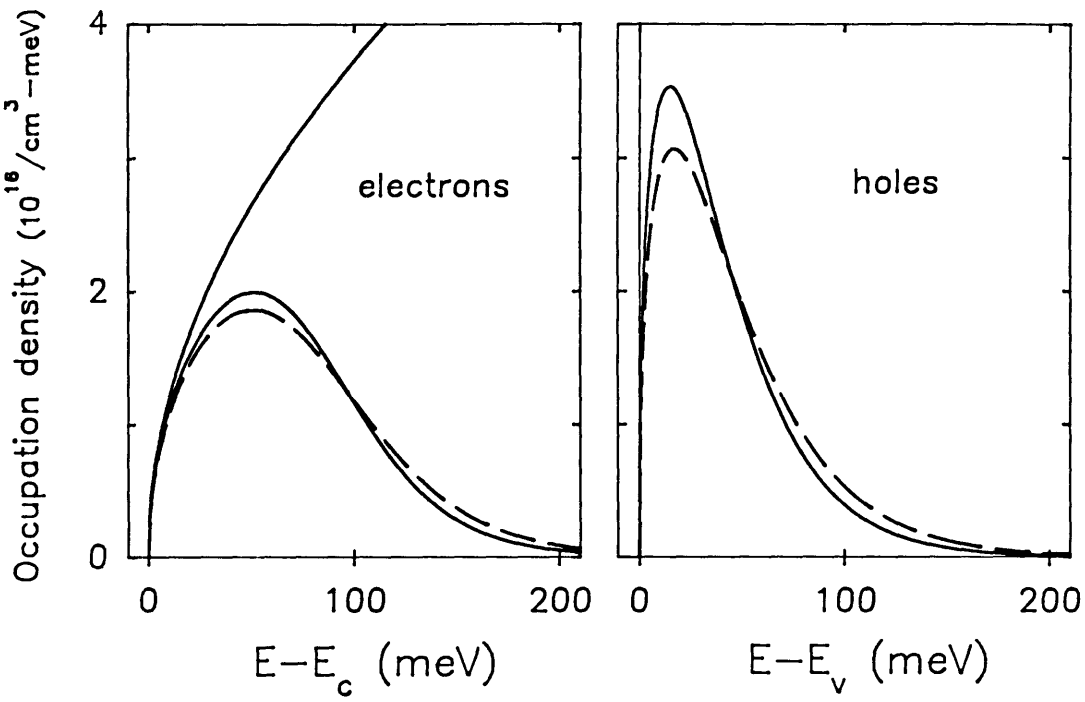

Figure 2.12: Effect of carrier temperature increase on electron and hole distributions. Carrier density is 2×10^{18} cm^{-3}. Carrier temperature is 300 K (solid line) and 350 K (dashed line). The other solid curve in each figure is a parabola that shows the density of states for the electrons and holes.

In a distribution of carriers the average energy per carrier $\langle E \rangle$ is the total energy divided by the number of carriers:

$$\langle E \rangle = \frac{\int_0^\infty E\,\rho(E)\,f(E)\,dE}{N}\,. \tag{2.20}$$

The electron and hole Fermi energies can be found from Eqs. 2.15 and 2.16. Then, the average energy per carrier is found from Eq. (2.20). Performing these computations as a function of carrier density results in the curves shown in Fig. 2.13. The average carrier energy $\langle E \rangle$ rises nearly linearly with density – because of the large hole density of states, the hole average energy is nearly flat.

When we consider the *separation* between the electron and hole Fermi energies and average energies, we obtain the results shown in Fig. 2.14. Recall that the separation between the electron and hole Fermi energies is the transparency point. Thus, for a carrier density of 2.5×10^{18} cm^{-3}, the gain, transparency, and absorption regimes are as indicated on the figure. Notice that the average energy separation lies above the

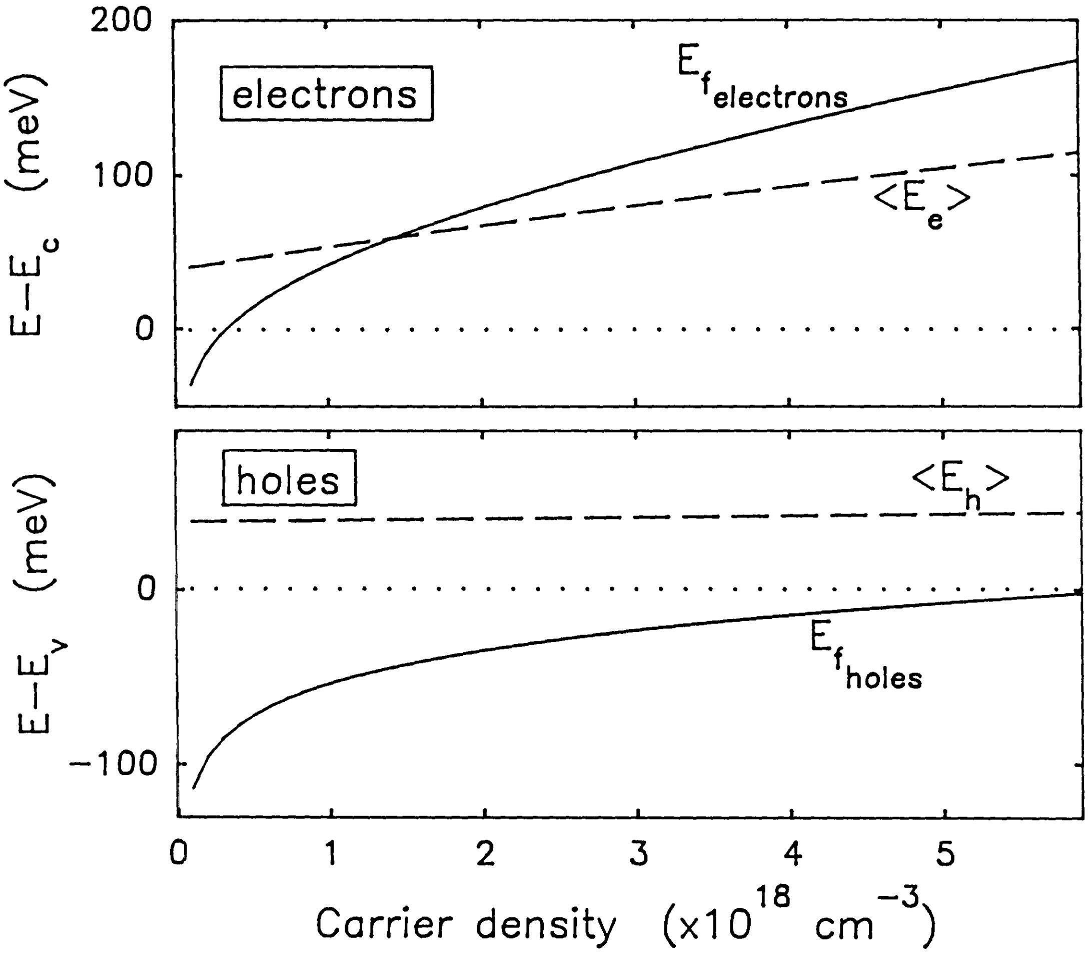

Figure 2.13: Electron and hole Fermi energies (solid line) and average energies (dashed line) as a function of carrier density.

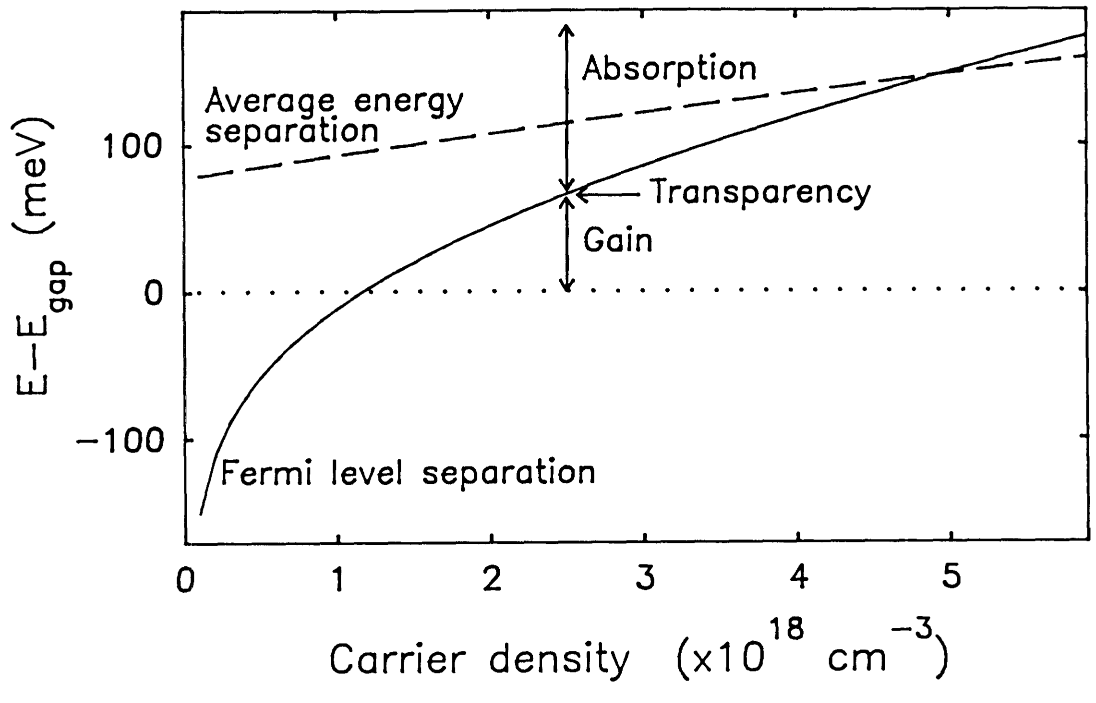

Figure 2.14: Separation between electron and hole Fermi energies (solid line) and average energies (dashed line) as a function of carrier density. The gain, transparency, and absorption regimes for electron and hole carrier densities of 2.5×10^{18} cm^{-3} are indicated.

Fermi energy separation at this carrier density. If a photon is absorbed and generates carriers with energies below the average energy of the distributions, then this will result in a net cooling of the carriers. This is the essence of stimulated cooling. Stimulated heating can result if a photon removes carriers from the distribution with energies less than the average energy of the distribution. These results will be referred to later in Chapter 6 when gain and refractive index dynamics attributed to stimulated cooling are observed.

2.3.2 Refractive index in AlGaAs

Now that we have a good handle on how the gain responds to carrier density and carrier temperature changes, in this section we look at how the refractive index responds to the same perturbations. Gain and refractive index are not independent quantities – together, they make up $\epsilon(\omega)$, the complex dielectric function. Thus, gain and refractive index are related through the Kramers-Kronig transform [73]. The Kramers-Kronig transform is often expressed as a relation between the refractive index n and the extinction coefficient k:

$$n(E) \;=\; 1+\frac{2}{\pi}\,P\int_0^\infty \frac{E'k(E')}{(E')^2-E^2}\,dE' \,, \tag{2.21}$$

where P indicates taking the principle value of the integral. The extinction coefficient is related to the gain g by the relation $k = -g\lambda/4\pi$. Then, Eq. (2.21) can be written

$$n(E) \;=\; 1-\frac{\hbar c}{\pi}\,P\int_0^\infty \frac{g(E')}{(E')^2-E^2}\,dE' \,. \tag{2.22}$$

Subtracting two gain curves gives the change in the gain spectrum $\Delta g(E)$ that results from a change in carrier density or a change in carrier temperature. So, for a given gain change $\Delta g(E)$, the corresponding refractive index change is

$$\Delta n(E) \;=\; -\frac{\hbar c}{\pi}\,P\int_0^\infty \frac{\Delta g(E')}{(E')^2-E^2}\,dE' \,. \tag{2.23}$$

This approach to relating gain and index changes in semiconductors has been applied in a number of theoretical and experimental studies [74, 75, 76, 77, 78, 79].

Fig. 2.15 shows the effect of carrier density changes on the gain and refractive index. As we saw in the previous section, increasing the carrier density causes an increase in the gain. Associated with this gain increase is a negative refractive index change. The gain change only affects above-band energies. However, the refractive index change caused by the above-band carrier density change extends well below the band edge. This is an interesting point because it says that refractive index measurements performed with below-band light are sensitive to the above-band dynamics. Indeed, the below-band measurements described later on in Chapter 4 will show this to be the case.

Fig. 2.16 shows the effect of a carrier temperature increase on the gain and refractive index. As shown in the previous section, heating up the carriers results in a decrease in the gain. The refractive index experiences an increase for energies near the band edge, and the maximum refractive index change occurs near the transparency point. Beyond 130 meV above the band edge, the refractive index change is negative. However, this energy lies deep in the absorption regime. The measurements described later on were not performed so far into the absorption regime, and so,

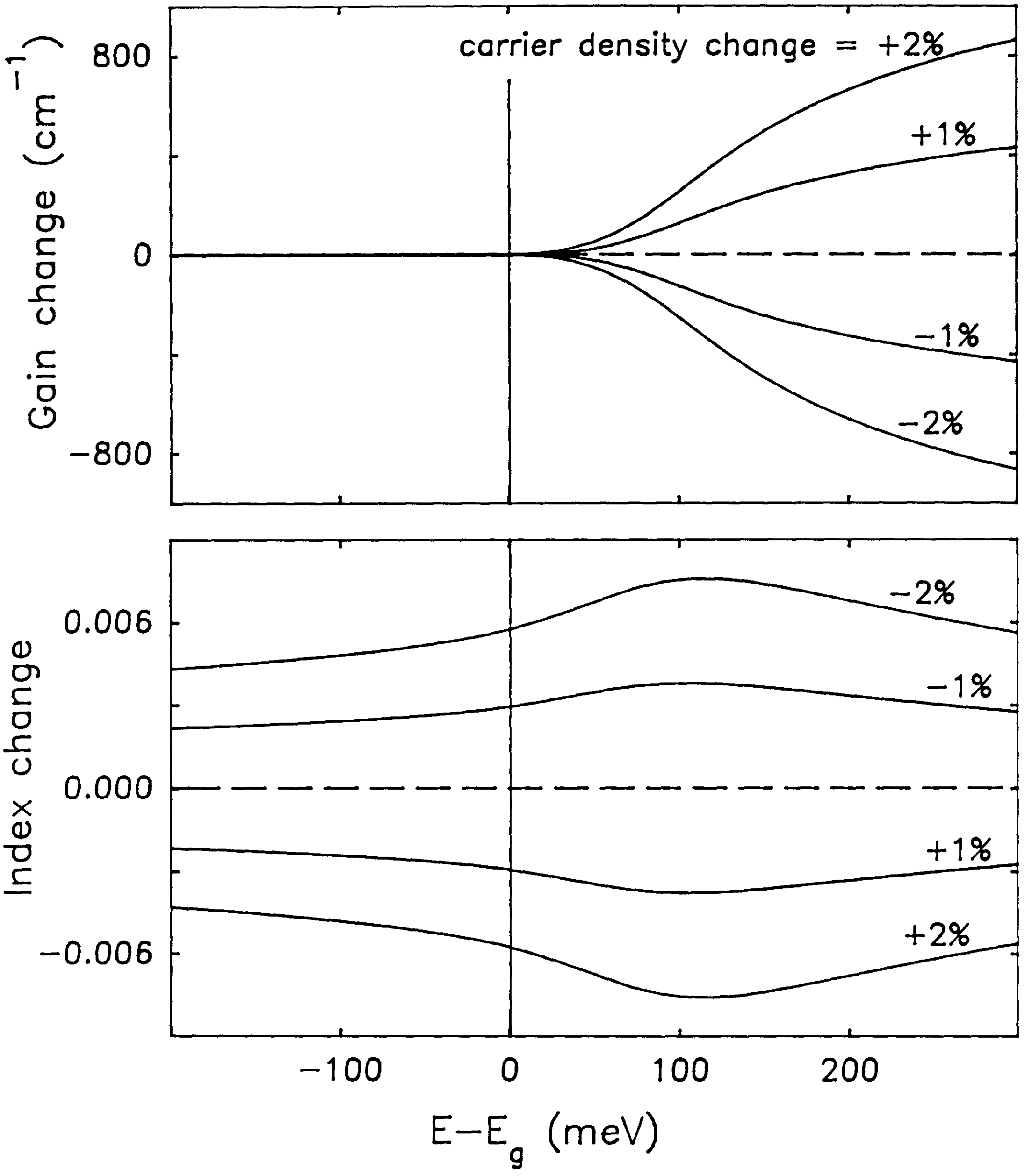

Figure 2.15: Gain and refractive index changes resulting from ±1 and ±2% changes in electron and hole densities. Carrier temperatures are fixed at 300 K, and the initial carrier density is 2×10^{18} cm^{-3}.

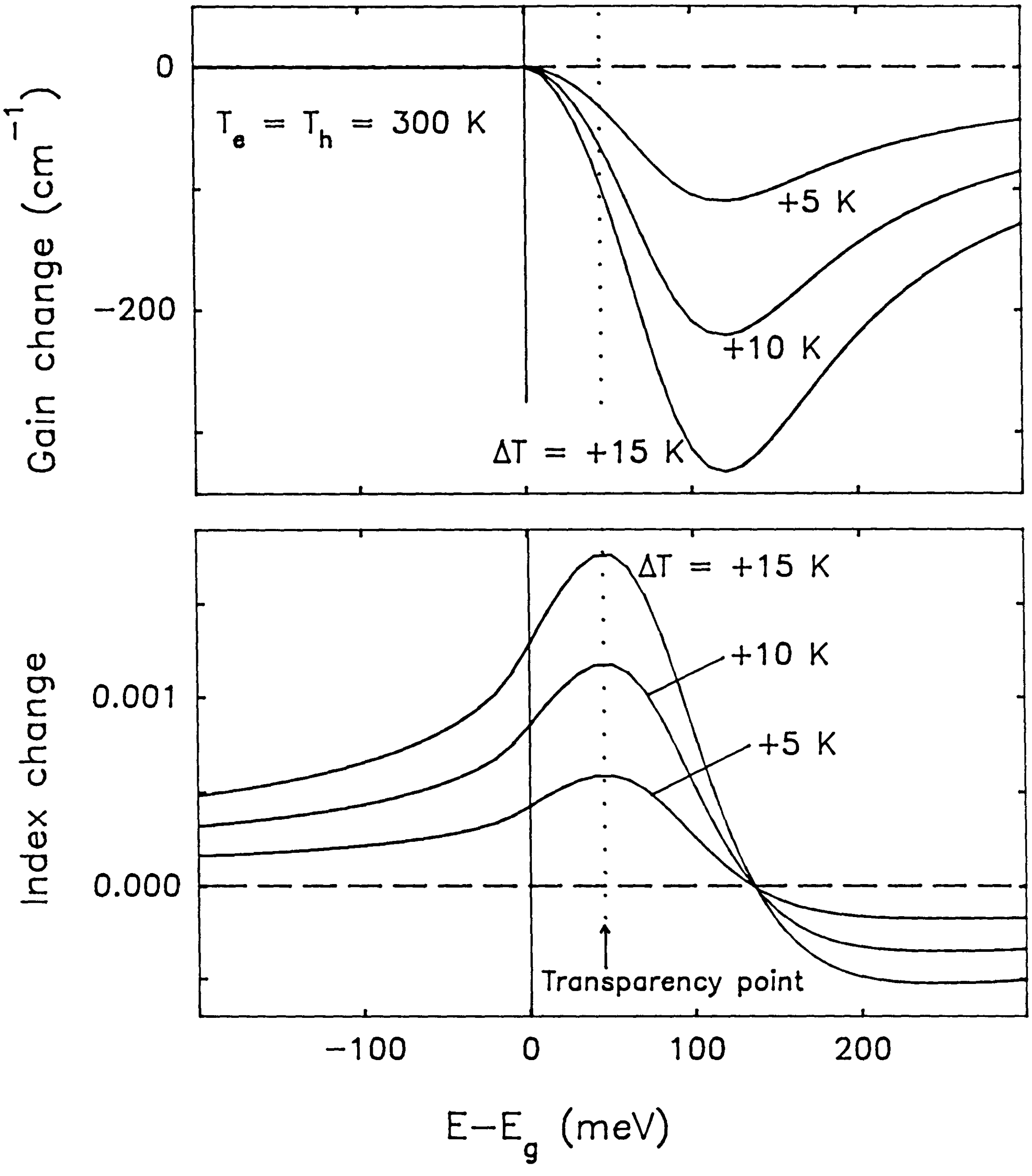

Figure 2.16: Gain and refractive index changes resulting from carrier temperature increases of 5, 10, and 15 K. The carrier density is fixed at 2×10^{18} cm^{-3}, and the initial carrier temperature is 300 K. The location of the transparency point is indicated by the dotted line.

the sign flip in the refractive index response was never observed. Again, although the gain change below the band edge is zero, the refractive index exhibits a nonzero below-band response to the heating of carriers in above-band states.

To summarize, an increase in the carrier density causes a positive gain change and a negative refractive index change. And when the carriers are heated, the gain decreases and the index increases. Finally, as we shall see later, the sensitivity of the below-band refractive index to the above-band carrier dynamics allows interesting below-band pump-probe measurements to be performed.

Chapter 3

Pump-Probe Measurement Technique

This chapter presents an overview of the pump-probe measurement technique. Pump-probe experiments are a common method for making time-resolved measurements of ultrafast processes in materials. A pump-probe experiment employs a short optical pulse called the pump to perturb a sample in some way. Since the processes of interest are generally too fast to be measured electronically, a second pulse called the probe is used to measure the response of the material to the pump pulse. By monitoring the probe pulse as the time delay between pump and probe is varied, one can extract time-resolved information about a material's optical properties. We begin the chapter with a general introduction to the theory of pump-probe measurements. Then, the specific techniques used in this thesis for measuring gain and refractive index dynamics in a waveguide are detailed. And finally, we spend some time studying an artifact in the refractive index measurement that is caused by chirp on the pulses.

3.1 Theory of pump-probe measurements

We begin by describing pump-probe measurements of absorptive nonlinearities [1]. In this case, a pump pulse with intensity profile $I_p(t)$ perturbs a sample. The absorption response of the sample to excitation by an impulse of light is described by the response function $h(t)$. The absorption change $\Delta\alpha(t)$ produced by the pump pulse is then the sample's impulse response function convolved with the pump intensity profile:

$$\Delta\alpha(t) \;=\; \int_{-\infty}^{\infty} dt_1\, h(t-t_1)\, I_p(t_1)\,. \tag{3.1}$$

This pump-induced absorption change is measured by a probe (or signal) pulse $I_s(t)$. The probe is generally a weaker version of the pump, delayed in time by τ. So, given the laser pulse intensity profile $I(t)$, the pump pulse is written $I_p(t) = I(t)$ and the probe pulse is written $I_s = \delta I(t-\tau)$. We take $\delta \ll 1$ to indicate that the probe is a weaker version of the pump pulse. When $\tau < 0$ (negative delay), the probe travels in front of the pump pulse; and when $\tau > 0$ (positive delay), the probe travels behind the pump. If we assume a small pump-induced absorption change ($|\Delta\alpha L| \ll 1$), then the change in probe intensity can be written

$$\Delta I_s(t) \;=\; [I_s(t)]_{\text{pump on}} - [I_s(t)]_{\text{pump off}} \;=\; -\Delta\alpha(t)\,\delta\,L\,I(t-\tau)\,, \qquad (3.2)$$

where L is the sample length. Unless otherwise specified, the measurements presented later on employ small pump perturbations, so this expression is valid.

After the pump and probe have traveled through the sample, the probe beam is monitored with a slow detector which integrates the signal over time. Thus, the measured signal S at a given pump-probe delay τ is

$$S(\tau) \;=\; -\delta L \int_{-\infty}^{\infty} dt\, I(t-\tau) \int_{-\infty}^{\infty} dt_1\, h(t-t_1)\, I(t_1)\,. \qquad (3.3)$$

We can cast this equation into a more meaningful form by making a change of variables: $t - t_1 = t' + \tau$. After substituting and interchanging the order of integration we get

$$S(\tau) \propto \int_{-\infty}^{\infty} dt\, h(t+\tau) \int_{-\infty}^{\infty} dt_1\, I(t_1)\, I(t_1+t) \;=\; \int_{-\infty}^{\infty} dt\, h(t+\tau)\, G^{(2)}(t)\,. \qquad (3.4)$$

Thus, the signal that we measure in a pump-probe experiment is the pulse intensity autocorrelation function, $G^{(2)}(t)$, convolved with the impulse response of the sample.

Often, the aim of a pump-probe measurement is to determine $h(t)$, the impulse response function of a given material. The procedure for pulling out the response function $h(t)$ from the measured $S(\tau)$ involves convolving a measured pulse autocorrelation with a guess for $h(t)$. In our case, the gain and refractive index response functions of AlGaAs can be described by a sum of decaying exponentials representing the various relaxation processes. This theoretical signal $S(\tau)$ is overlaid on the measured pump-probe data and by trial and error, the form for $h(t)$ is revealed. We will discuss this fitting procedure in more detail later on.

One shortcoming of the above analysis is that we have not considered coherent interactions between the pump and probe pulses when they are overlapped in time [1, 80, 81, 82, 83, 84]. These coherent interactions can give rise to signals that contribute to the measured signal $S(\tau)$ around zero delay. The physical mechanism for this "coherent artifact" is the grating created by interference between the pump and probe electric fields. This grating can scatter light between the pump and probe pulses, causing an artifact to appear in the measured pump-probe signal.

In the case where the pump and probe pulses are polarized parallel to one another, there is always an artifact signal generated. However, the experiments described here employ orthogonally polarized pump and probe pulses. In this case, an artifact may or may not be present, depending on the terms that make up $\chi^{(3)}(t)$, the third-order electrical susceptibility tensor. Given a y-polarized pump pulse and a x-polarized probe pulse, the pump-probe signal that we measure can be written:

$$S(\tau) \;\propto\; \gamma_{\perp}(\tau) \;+\; \beta_{\perp}(\tau)\,, \tag{3.5}$$

where

$$\gamma_{\perp}(\tau) \;=\; \int_{-\infty}^{\infty} dt'\, A_{xxyy}(t'+\tau) \int_{-\infty}^{\infty} dt\, |E(t)|^2\, |E(t+t')|^2\,, \quad \text{and} \tag{3.6}$$

$$\beta_{\perp}(\tau) \;=\; \int_{-\infty}^{\infty} dt \int_{-\infty}^{\infty} dt'\, E^{*}(t-\tau)\, E(t)\, A_{xyyx}(t-t')\, E^{*}(t')\, E(t'-\tau)\,. \tag{3.7}$$

The $\perp$ symbol indicates that this is the signal for perpendicularly polarized pump and probe pulses. The $A(t)$ response function term is proportional to the $\chi^{(3)}(t)$ tensor element indicated. The first term $\gamma_{\perp}$ is the standard pump-probe signal that was derived above (Eq. (3.4)). The response function A_{xxyy} couples the y-polarized pump to the x-polarized probe. The second term $\beta_{\perp}$ is the coherent artifact signal. This artifact signal is created by mixing of the pump and probe electric fields through the A_{xyyx} term. Notice that the coherent artifact is only present when the pump and probe are overlapped in time. In the case of perpendicular pump-probe measurements, coherent coupling of the pump and probe only occurs for times faster than the polarization reorientation time of the material. As scattering occurs, the carriers lose their polarization memory, thus washing out the coherent artifact. In organic dyes, this reorientation time is a relatively slow process, and the artifact given by $\beta_\perp$ has been observed experimentally [80, 81, 82]. However, in semiconductors, the coherent artifact for perpendicular polarization measurements is believed to be less important because the scattering times are very fast (~10 fs) [85, 86]. One exception may be for instantaneous nonlinearities such as two-photon absorption and the optical Stark effect. For these processes, there may actually be some coherent artifact that contributes to the measured pump-probe signal in the experiments.

3.2 Measurement of gain dynamics

The experimental setup for measuring gain dynamics in active waveguides is shown in Fig. 3.1. A single pulse from the laser is split into two pulses, the pump and the probe. The probe polarization is rotated to horizontal with a half-wave plate, while the pump remains vertically polarized. The two pulses are coupled through the waveguide using microscope objectives. The coupling efficiency into the waveguide was never very high – in the range of 6%. Still, getting good coupling efficiency was not an important goal since the laser system generated plenty of power, and we generally wanted small powers in the waveguide anyway. Of course, if someone were to build an all-optical device based on these nonlinearities, the optical coupling efficiency becomes an important issue.

After traveling through the waveguide, the pump is filtered out with a polarizing beam splitter (PBS), and the average power in the probe beam is detected with a slow detector. The pump beam is chopped with a mechanical chopper, and then a lock-in amplifier is used to detect the pump-induced change in the probe power. By mechanically delaying the pump pulse with respect to the probe pulse with a computer controlled micron-precision delay stage, we can measure the pump-induced gain dynamics in the waveguide. The signal that we measure is given above by Eq. (3.4).

One complication that occurs in performing these measurements is interference between the pump and probe electric fields. After traveling through the waveguide the pump polarization ratio is generally around 20:1. Because of this low polarization discrimination, the pump pulse can never be completely eliminated by the PBS. Thus, a fraction of the pump power leaks onto the detector along with the probe. Some

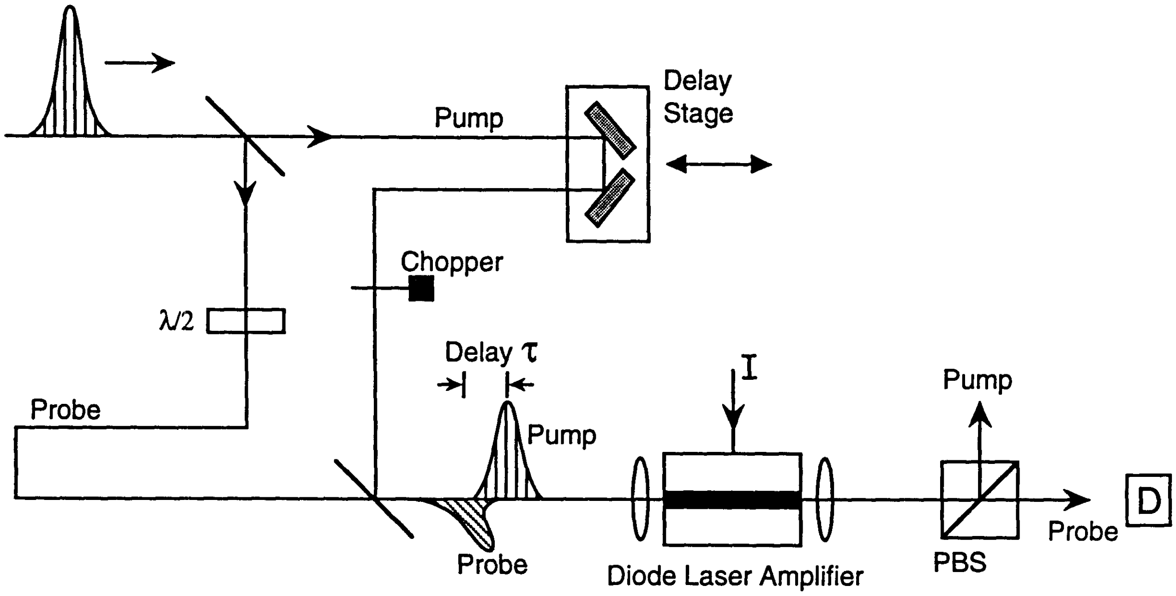

Figure 3.1: Experimental setup for pump-probe measurement of gain nonlinearities. After traveling through the waveguide, the polarizing beam splitter (PBS) selects the probe pulse for measurement by the detector (D).

of this polarization cross-talk is probably caused by coupling between the TE and TM modes in the waveguide structure. In any case, some residual pump pulse – horizontally polarized, like the probe – was always present on the detector along with the probe. So, around zero-delay, the pump and probe electric fields interfere at the detector.

Typical pump-probe data for this case is shown in Fig. 3.2. As the pump power (measured just before the waveguide) is reduced, the pump-probe signal gets smaller but maintains its general shape. However, superimposed on the pump-probe signal is an oscillatory signal caused by pump-probe interference. The relative size of this interference increases as the pump power is reduced. The reason for this is that the pump-probe signal scales like intensity squared: $I_p \cdot I_s$ (see Eq. (3.4)), but the interference signal scales like intensity: $E_p \cdot E_s$. Thus, at low powers the interference signal dominates the pump-probe signal. This interference is a problem because we usually want to perform measurements with low pump and probe powers so that we induce a small perturbation in the sample. Pump powers in the 0.3 to 0.6 mW range were generally desirable because they induced absorptive changes on the order of 5%.

The solution to this problem was found by introducing an acousto-optic modulator

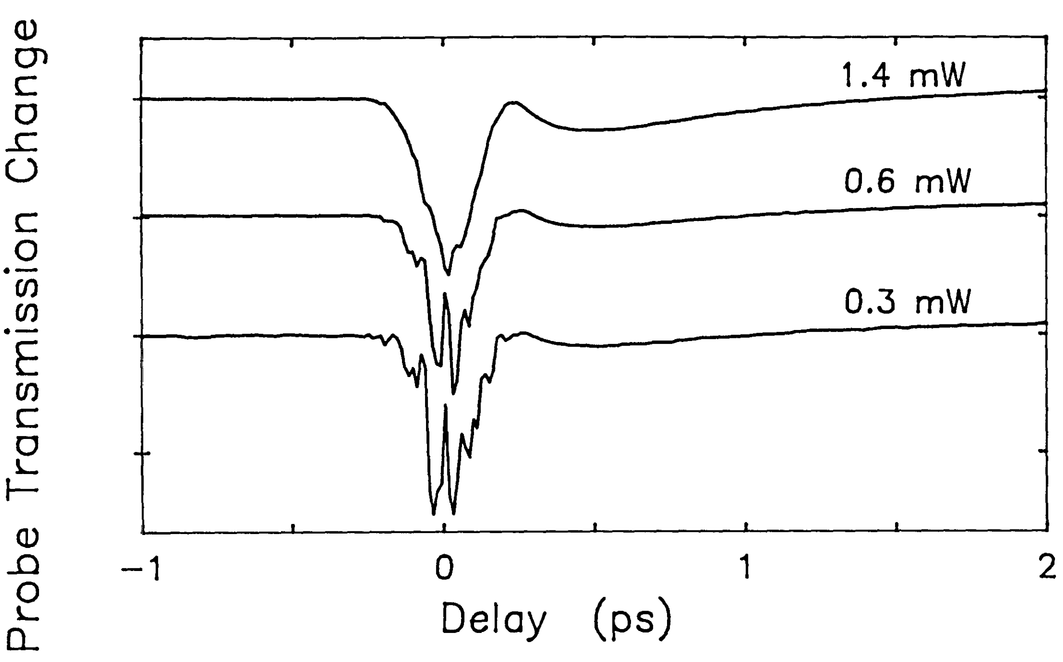

Figure 3.2: Measured probe transmission through the waveguide without an AOM. The pump power just before the waveguide is indicated above each plot. The diode laser bias current was 30 mA, and the pump-probe wavelength was 827 nm.

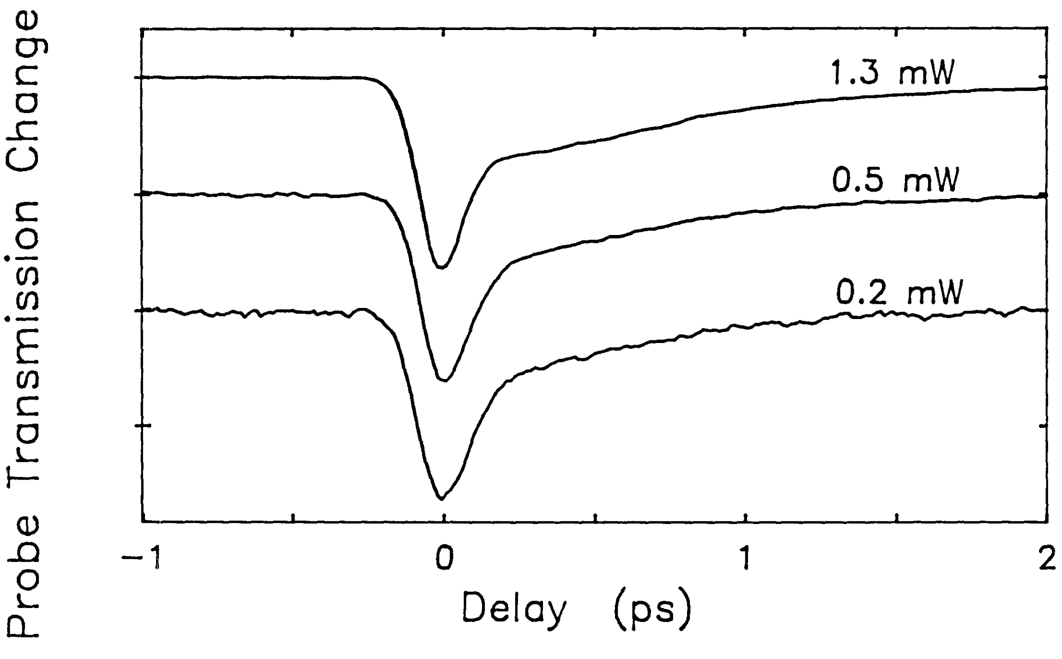

Figure 3.3: Measured probe transmission through the waveguide with an AOM used to upshift the probe frequency by 40 MHz. The pump power just before the waveguide is indicated above each plot. The diode laser bias current was 33 mA, and the pump-probe wavelength was 826 nm.

(AOM) into the setup. A beam sent through the AOM has some of its power deflected at a small angle from the primary beam. This deflected beam has its carrier frequency upshifted by 40 MHz, the drive frequency of the AOM. In the measurements, the undeflected beam was used as the pump, and the upshifted beam was used as the probe. Then, when the pump and probe electric fields interfere, they generate an interference signal that oscillates at 40 MHz. This 40 MHz signal that shows up around zero delay is not seen by the detector and lock-in arrangement. So, the interference signal is still present – at 40 MHz, but it is not picked-up by the detection apparatus.

Data taken using an AOM to upshift the probe frequency is shown in Fig. 3.3. Note that the bias current and wavelength at which this measurement was performed is different from the data shown in Fig. 3.2, and thus, the shape of the pump-probe signal is different here. But the important point is that the interference signal has disappeared, allowing us to perform measurements with 0.2 mW of pump power without any pump-probe interference problems. The size of the probe transmission change is about 2% for the 0.2 mW case. Now, we are limited only by noise generated by the laser system itself, and so, sensitive measurements are easily accomplished. The refractive index measurements described in the next section were also susceptible to this pump-probe interference problem. And so, in all of the measurements that we describe in this thesis the AOM was used to eliminate the pump-probe interference signals.

3.3 Measurement of index dynamics

Conceptually, pump-probe measurements of refractive index dynamics are similar to the gain measurements described above, but they are a bit more tricky to perform. In addition to the pump and probe pulses, we introduce a third pulse, called the reference, which acts as a phase reference for the probe. After traveling through the waveguide, we measure the probe *phase* change (rather than the transmission change) as a function of pump-probe delay. The probe phase shift is measured by interfering the probe pulse with the reference. By monitoring shifts in the probe-reference interference pattern, we can deduce the pump-induced phase shift of the probe pulse. The measured probe phase shift ($\Delta\phi$) is related to the pump-induced refractive index change (Δn) through the relation $\Delta\phi/2\pi = \Delta n L/\lambda$, where L is the device length (300 μm).

Since the induced refractive index changes measured here are usually quite small ($\sim 0.005\%$), one must be able to accurately measure small phase shifts. This ability is realized with an instrument called the time-division interferometer (TDI). A schematic of the TDI is shown in Fig. 3.4. The TDI is an interferometer formed by separating the probe and reference pulses in time rather than space. This is accomplished by the arrangement of half and quarter wave plates and polarizing beam splitters shown in the TDI schematic. In the TDI, both the probe and reference travel through the waveguide, separated in time by about 360 picoseconds. Thus, the reference and probe pulses see the same environment, except for the pump-induced phase shift experienced by the probe. Since the pulses travel mostly over the same path, thermal artifacts arising from slow temperature changes in the diode laser [87] are eliminated and mechanical interferometer noise is reduced a great deal. This results in a remarkably stable interferometer that allows the accurate measurement of phase shifts as small as $\pi/1000$ radians. Previously, the TDI was used in optical fiber measurements and below-band measurements of passive waveguides [25, 26, 27].

A detailed look at the TDI after the pulses emerge from the waveguide is shown in Fig. 3.3. After traveling through the waveguide, the probe and reference pulses are overlapped in time. Then, a half-wave plate rotates the pulse polarizations by 45 degrees and a polarizing beam splitter then generates a probe-reference interference pattern that is monitored by two detectors (D_1 and D_2). The signal at the detectors is composed of a constant voltage due to the pump and a voltage that oscillates sinusoidally as the probe-reference phase is varied. The signal from the two detectors is subtracted, eliminating the DC pump voltage and leaving the oscillatory component. A piezoelectric transducer (PZT) is used to precisely set a $\pi/2$ phase difference between the probe and reference. As shown in the next section, the $\pi/2$ probe-reference phase offset results in an output signal that is proportional to the probe phase shift. The pump pulse is chopped, and a lock-in amplifier is used to detect the pump-induced probe phase shift. The stabilization circuit and PZT stabilize the interferometer against low frequency vibration and drift. The stabilization circuit responds to frequencies below about 100 Hz. Since the pump beam is chopped at around 1.5 kHz, the stabilization circuit does not see or try to stabilize away the 1.5 kHz signal that we want to measure.

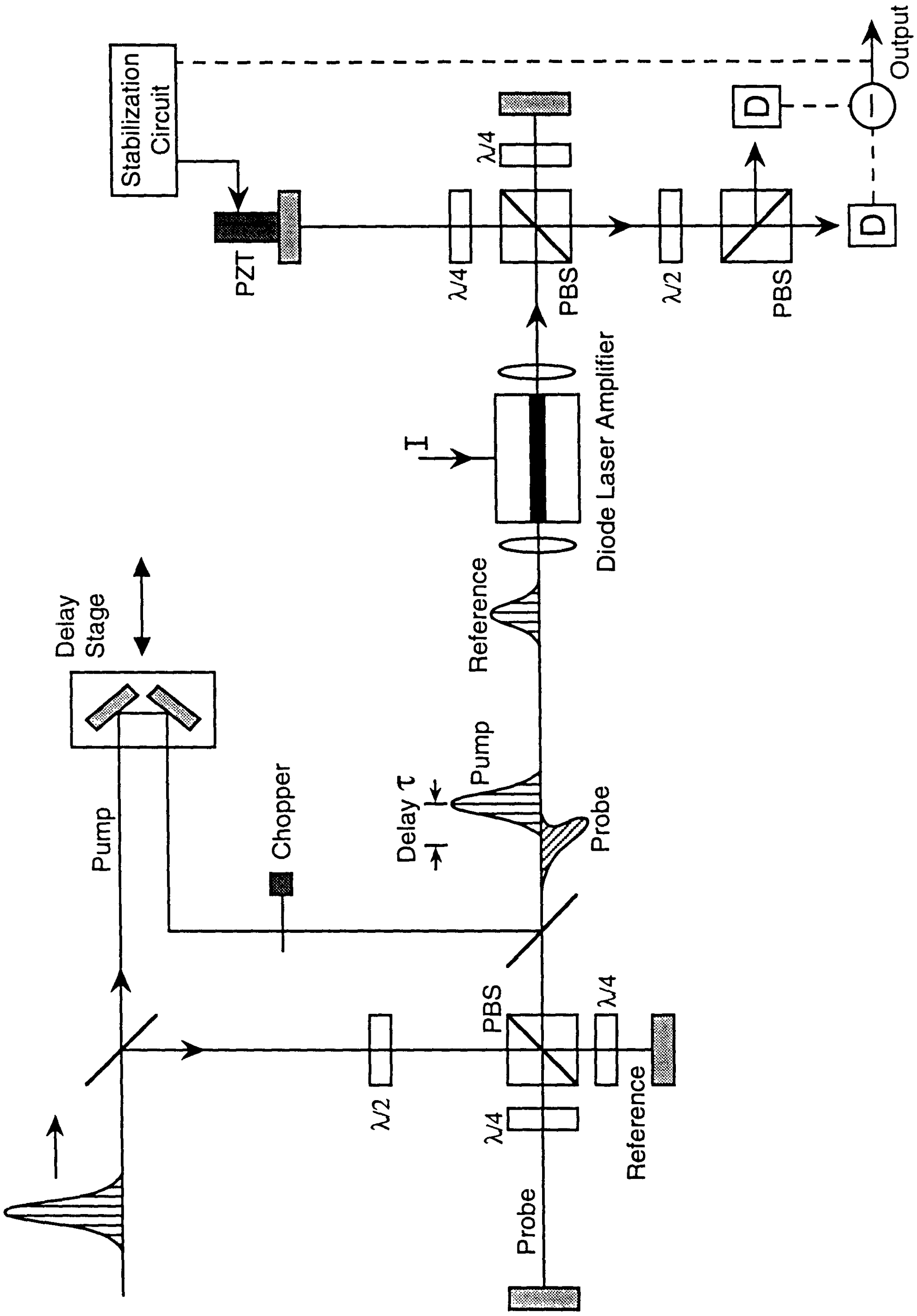

Figure 3.4: Schematic of the time division interferometer (TDI) for measurement of refractive index dynamics in waveguides.

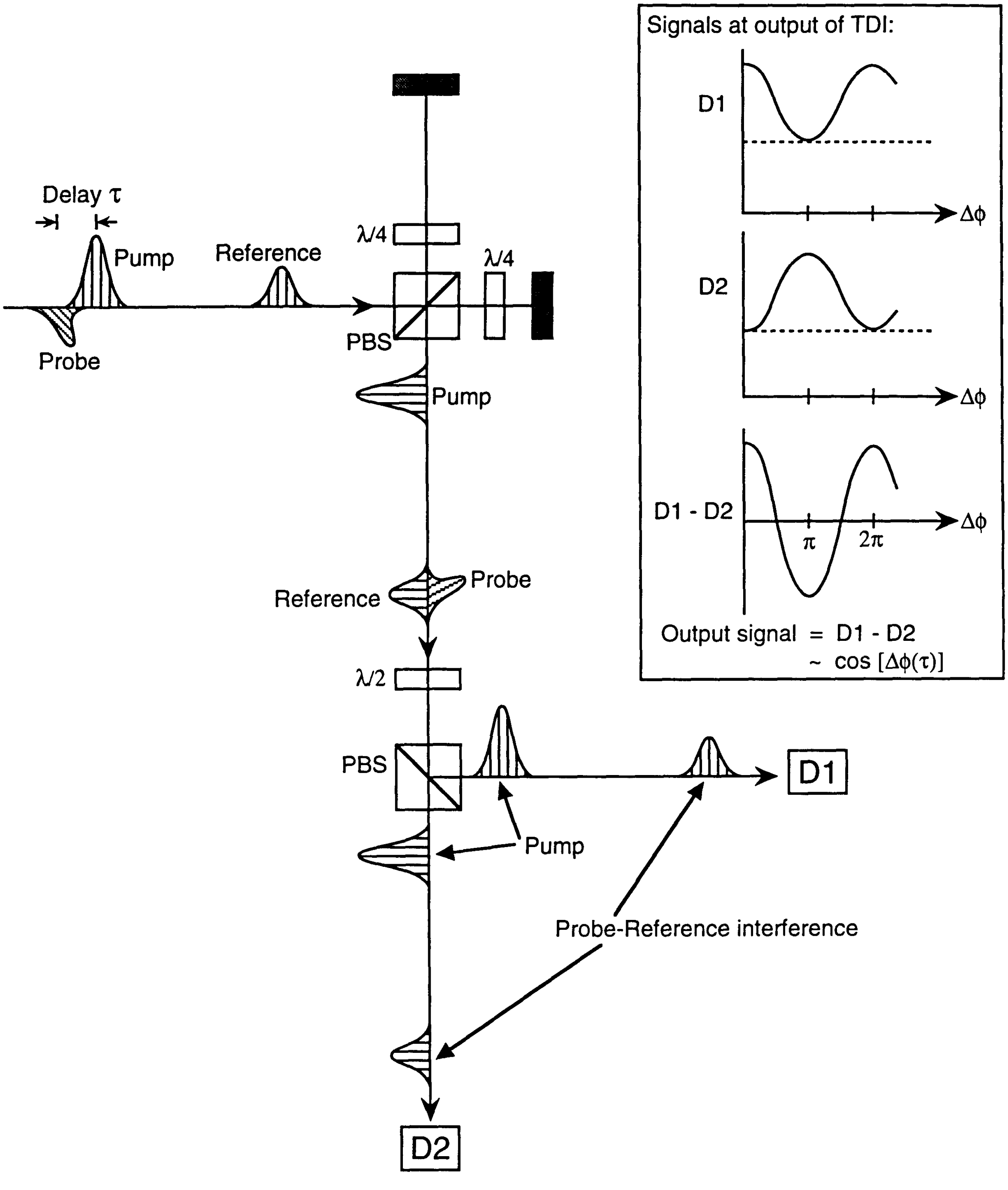

Figure 3.5: Expanded view of the TDI after pulses emerge from the waveguide. The signals at the two detectors as a function of probe-reference phase difference are shown in the inset.

3.4 Theory of index measurements

The mathematical description of the signals generated by the TDI begins with the effect of the pump on the refractive index. The pump induces a refractive index change Δn that causes a phase shift $\Delta\phi_{\mathrm{nl}}$ of the probe pulse. This pump-induced nonlinear phase shift can be written

$$\Delta\phi_{\mathrm{nl}}(t) = \left[\frac{2\pi L}{\lambda}\right]\Delta n(t) = \left[\frac{2\pi L}{\lambda}\right]\int_{-\infty}^{\infty} dt_1\, h'(t-t_1)\, I_p(t_1)\,, \tag{3.8}$$

where $h'(t)$ is the refractive index impulse response function of the material. The signal at the two detectors is

$$|E_s + E_r|^2 + |E_p|^2 \quad \text{and} \quad |E_s - E_r|^2 + |E_p|^2\,, \tag{3.9}$$

where E_s is the probe electric field, E_r is the reference electric field, and E_p is the pump electric field. The slow detectors integrate these signals over time, and then, subtracting the detector outputs eliminates the constant background pump signal. The output signal is then

$$S(\tau) = 4\,\mathcal{R}e\int_{-\infty}^{\infty} dt\, E_s(t)\, E_r^*(t)\,. \tag{3.10}$$

If the electric field of the pump pulse is $E(t)$, then the electric field of the delayed probe is $E_s = E(t-\tau)e^{i\Delta\phi_{\mathrm{nl}}(t)}$. And the electric field of the reference is $E_r = E(t-\tau)e^{i\phi_{\mathrm{bias}}}$, where ϕ_{bias} is the bias phase between the probe and reference that is set and maintained by the stabilization circuit. Then, for the output signal we obtain

$$S(\tau) \propto \mathcal{R}e\int_{-\infty}^{\infty} dt\, |E(t-\tau)|^2\, e^{i[\Delta\phi_{\mathrm{nl}}(t)-\phi_{\mathrm{bias}}]} = \int_{-\infty}^{\infty} dt\, I(t-\tau)\, \cos[\Delta\phi_{\mathrm{nl}}(t) - \phi_{\mathrm{bias}}]\,. \tag{3.11}$$

If the bias phase is set at $\pi/2$ and if we assume that $\Delta\phi_{\mathrm{nl}} \ll \pi$, then the output signal becomes

$$S(\tau) \propto \int_{-\infty}^{\infty} dt\, I(t-\tau)\, \sin[\Delta\phi_{\mathrm{nl}}(t)] \approx \int_{-\infty}^{\infty} dt\, I(t-\tau)\, \Delta\phi_{\mathrm{nl}}(t)\,. \tag{3.12}$$

Thus, if the pump-induced phase shifts are small, the output signal is directly proportional to the probe phase shift. Also, notice that when there is no nonlinear phase shift present, the output signal is zero. Subtracting the signals from the two detectors eliminates the laser noise present in the pump. This is true provided the pump pulse is split evenly between the two detectors. If this is not the case, there will be a residual pump signal present. Thus, it is important to properly null out the pump before beginning a measurement. Finally, when we substitute in the expression for $\Delta\phi_{\text{nl}}$ from Eq. (3.8), we obtain the output signal for the TDI:

$$S(\tau) \;\propto\; \int_{-\infty}^{\infty} dt\, h'(t+\tau) \int_{-\infty}^{\infty} dt_1\, I(t_1)\, I(t_1+t) \;=\; \int_{-\infty}^{\infty} dt\, h'(t+\tau)\, G^{(2)}(t)\,. \quad (3.13)$$

This is the signal obtained from a pump-probe measurement of refractive index dynamics, analogous to Eq. (3.4), the signal derived for the gain measurements.

From Eq. (3.11) we see that if the interferometer is instead biased at $3\pi/2$ or at $-\pi/2$, the output signal flips sign. Indeed, this reversal of the signal is observed experimentally. Fig. 3.6 shows two probe phase shift signals measured versus pump-probe delay. The solid curve shows the signal when the TDI is biased at $\pi/2$. And the dashed curve shows the signal when the bias phase is changed by $\pm\pi$ (or ± 180 degrees, as indicated in the figure).

One issue to address is how the absorptive nonlinearities that are also present on the probe pulse affect the measured TDI signal. It turns out that changes in the probe amplitude do appear in the output TDI signal. But, if the TDI is biased at the $\pi/2$ operating point and if the induced absorption changes are small, then the appearance of absorptive dynamics in the TDI measurement is a second order effect that can be neglected. This conclusion is only valid if we are using pulses that have zero chirp, which we have assumed throughout the preceding analysis. As we will see in the next section, it turns out that the gain dynamics can mix in with the measured index dynamics when we have pulses that are chirped.

Before addressing that issue, we first want to describe the effect of temporal offsets between the probe and reference pulses. In the above analysis, we assumed that after traveling through the waveguide, the probe and reference pulses were overlapped right on top of one another. This is what we tried to do in all the measurements that follow. However, just to characterize the TDI signal, we will now analyze how shifts in the

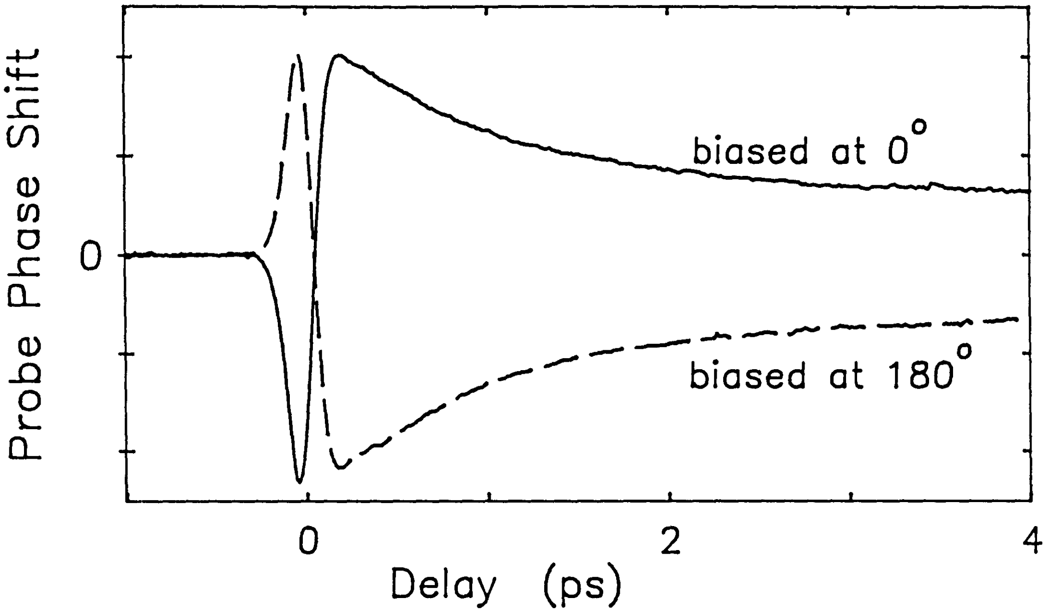

Figure 3.6: Probe phase shift versus pump-probe delay measured with the TDI. The interferometer is biased at two different operating points 180 degrees out of phase. The diode laser bias current was 27 mA, and the pump-probe wavelength was 832 nm.

probe-reference overlap affect the measured signal. We assume a Gaussian shape for the laser pulse electric field envelope: $E(t) = E_0 e^{-at^2} e^{-i\omega_0 t}$. We write the probe pulse as $E_s = E(t-\tau)e^{i\Delta\phi_{\rm nl}}$. The reference pulse is shifted in time with respect to the probe pulse by T, where T corresponds to an integral number of wavelengths ($T = 2n\pi/\omega_0$). So, the reference is written $E_r = E(t-\tau-T)e^{i\phi_{\rm bias}}$. When $T > 0$, the reference is delayed with respect to the probe, and when $T < 0$, the reference is advanced. Then with the bias phase set at $\pi/2$ the output signal Eq. (3.10) can be written

$$S(\tau) \propto e^{-aT^2/2} \int_{-\infty}^{\infty} dt\, e^{-2a[(t-\tau)-T/2]^2}\, \Delta\phi_{\rm nl}(t)\,. \tag{3.14}$$

The exponential outside the integral just indicates that the signal magnitude decreases as the probe-reference offset T increases. This makes sense, because as the probe and reference are pulled apart from one another, the size of their interference signal decreases. So, for a given phase shift, a smaller signal from the TDI is observed. The exponential inside the integral says that the measured signal will shift in time by $T/2$

for a given probe-reference delay of T. This means that shifting the reference pulse around will shift the measured signal around in time as well. The signal is shifted by $T/2$ – half the amount of the probe-reference offset. What matters is the location of the maximum interference between the probe and reference, and this moves half as fast as the distance T between the peaks of the pulses.

Fig. 3.7 shows the measured effect of moving the reference pulse with respect to the probe pulse. The reference is moved by simply translating the reference arm of the interferometer after the waveguide. The reference pulse was moved by approximately ±100 femtoseconds, measured by reading the scale on a hand-turned stage (very approximate). The curves in Fig. 3.7 are shifted by 30 to 40 fs. Thus, the TDI behaves as expected when the probe and reference pulses are offset from one another.

3.5 Chirp artifact in index measurements

In the previous sections, we assumed that the pulses were transform-limited. Now, we consider the effect of pulse chirp on the pump-probe index measurements [82, 88]. It turns out that chirped pulses give rise to an artifact. However, this is not a "coherent" artifact like we described in Section 3.1. Rather, this artifact arises because the gain response mixes in with the refractive index measurement due to the pulse chirp.

Let us first look at how chirped pulses affect the experimentally measured pump-probe refractive index dynamics; then an explanation will be sought. Fig. 3.8 shows measured probe phase shifts for chirped pulses with the probe and reference advanced and delayed with respect to one another. The pulses were passed through a prism pair before entering the experimental setup. By varying the amount of prism insertion into the beam, the chirp on the pulses just before being coupled into the diode laser could be monitored with the autocorrelator and set as desired. The pulses were broadened to about 150 femtoseconds, approximately 50% over transform limit. All the pulses – pump, probe, and reference – were chirped the same amount. The delay T between the probe and reference was set at approximately ±100 femtoseconds.

When the probe and reference are overlapped, the measured probe phase shift is nearly identical for positively and negatively chirped pulses. We observe a positive refractive index change that recovers with a ~ 1.1 picosecond time constant. This signal is caused by carrier heating, and we will have much more to say about it in the next chapter. Just note that if the probe and reference pulses are overlapped, there is

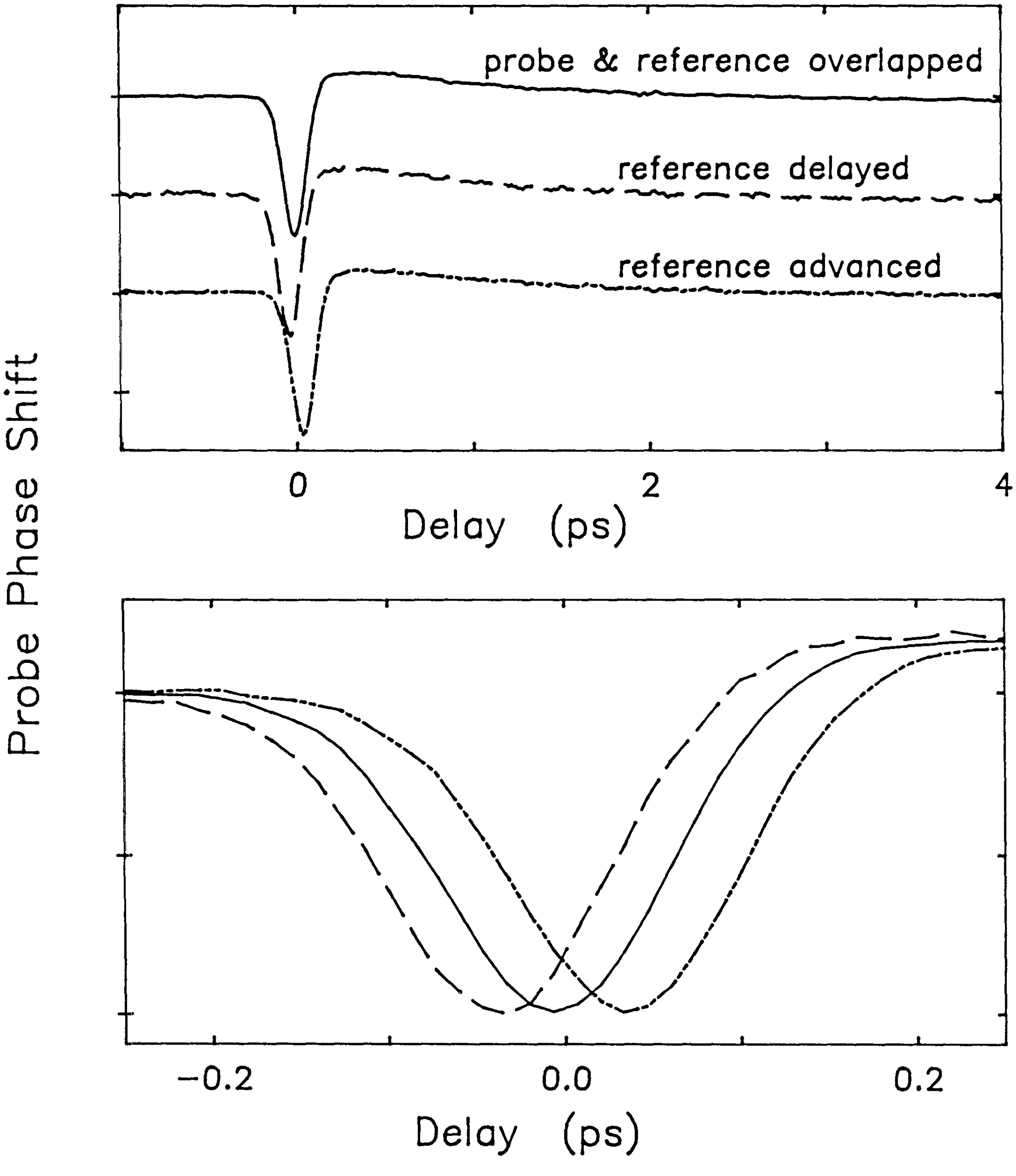

Figure 3.7: Measured probe phase shift with the probe and reference pulses overlapped (solid line), reference delayed to back part of probe (dashed line), and reference advanced to front of probe (dashed-dotted line). The diode laser bias current was 10 mA, and the pump-probe wavelength was 871 nm. The lower plot shows the same data on an expanded time scale.

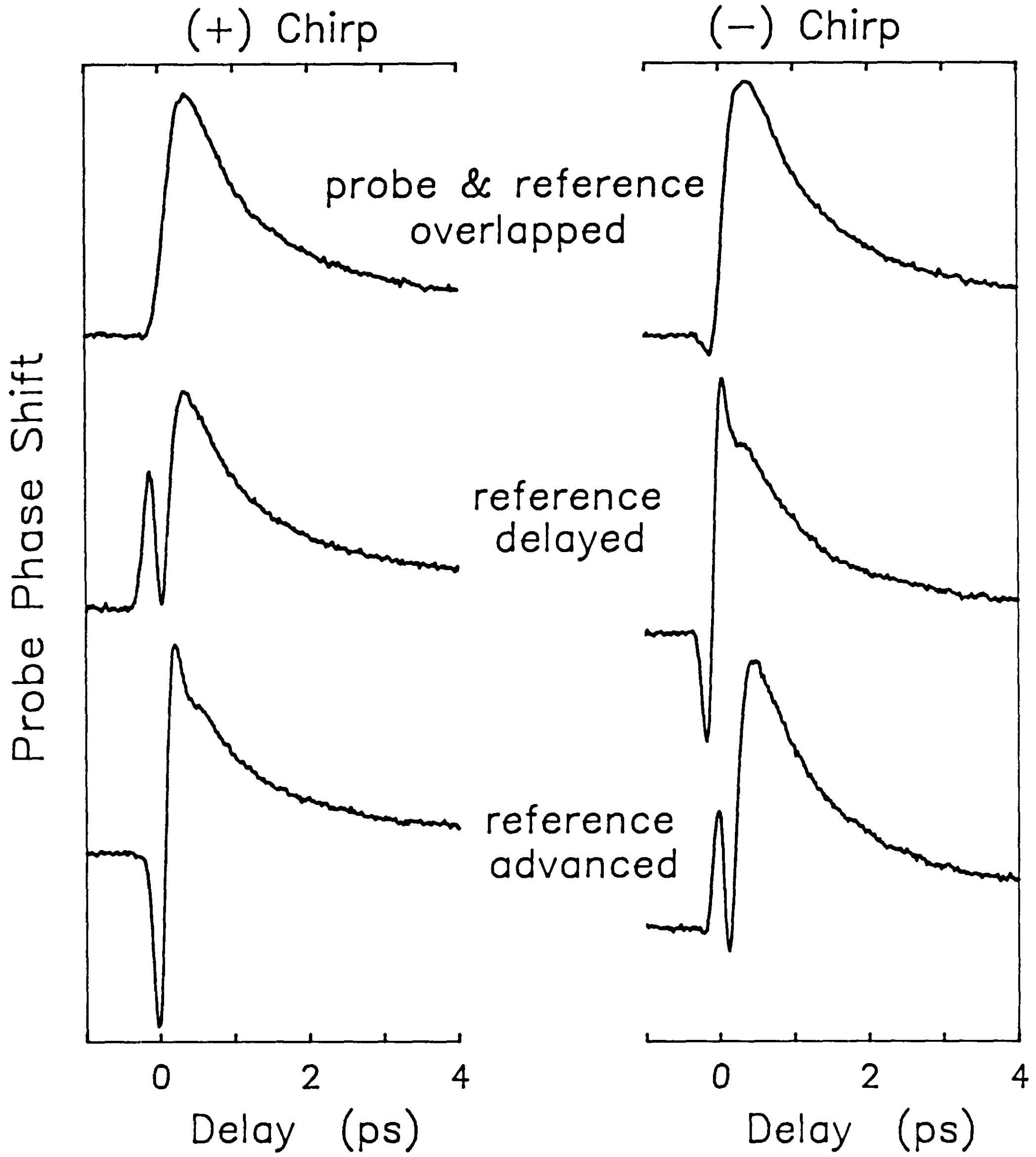

Figure 3.8: Measured probe phase shifts for positively and negatively chirped pulses at various probe-reference offsets. The diode laser bias current was 30 mA, and the pump-probe wavelength was 882 nm.

little or no artifact present, regardless of the pulse chirp. Now, as the reference pulse is advanced and delayed with respect to the probe pulse, we develop a fast dynamic around zero delay that looks like a pulse derivative feature added to the real signal. This is an artifact that is not related to any real index changes. Notice that the artifact exhibits symmetric behavior with respect to pulse chirp and probe-reference delay. The artifact for *positively* chirped pulses with the reference *delayed* is similar to the signal for *negatively* chirped pulses with the reference *advanced* (and vice versa).

Having characterized the index artifact experimentally, we will now try to understand it using the pump-probe formalism outlined in the previous section. Although the Ti:sapphire system produces sech(t)-shaped pulses, for calculational simplicity we assume the pulses have a Gaussian shape. Gaussian pulses with a frequency chirp can be written $E(t) = E_0 e^{-(a+ib)t^2} e^{-i\omega_0 t}$. The pulse width is determined by a, and the pulse chirp is described by b. The chirp arises because the e^{-ibt^2} term is a time-dependent phase, which gives a linear frequency sweep across the pulse. $b > 0$ indicates a positive chirp (in time, the red wavelengths lead the blue wavelengths), and $b < 0$ indicates a negative chirp. As in the previous section, the delayed reference pulse is written as a pulse shifted in time by an integral number of periods T with respect to the probe pulse: $E_r = E(t-T)e^{i\phi_{\mathrm{bias}}}$. To make the equations that follow somewhat easier to read, we write the pump pulse as delayed by τ with respect to the probe: $I_p(t) = I(t+\tau)$.

Now, we consider the effect on the probe pulse of the refractive *and* the absorptive nonlinearities induced by the pump pulse. The pump pulse causes a change in the complex phase of the probe $\Delta\Phi$ that can be written:

$$\Delta\Phi(t,\tau) = \left(\frac{2\pi L}{\lambda}\right)\Delta n + iL\Delta\alpha \tag{3.15}$$

$$= \left(\frac{2\pi L}{\lambda}\right)\int_{-\infty}^{\infty} dt_1\, h'(t-t_1)I(t_1+\tau) + iL\int_{-\infty}^{\infty} dt_1\, h(t-t_1)I(t_1+\tau)\,. \tag{3.16}$$

The first term contains the real contribution from the refractive index response function $h'(t)$ and the second term contains the imaginary contribution from the absorptive response function $h(t)$. For small perturbations, the effect of this complex phase on the probe pulse is

$$E_s \;=\; E(t)\,e^{i\Delta\Phi} \;\simeq\; E(t)\left[1 \,+\, i\Big(\frac{2\pi L}{\lambda}\Big)\Delta n \,-\, L\Delta\alpha\right]. \tag{3.17}$$

From Eq. (3.10) the signal at the output of the TDI is then

$$S(\tau) \;\propto\; \mathcal{R}e\int_{-\infty}^{\infty} dt\, E_r^*(t)\, E(t)\left[1 \,+\, i\Big(\frac{2\pi L}{\lambda}\Big)\Delta n \,-\, L\Delta\alpha\right]. \tag{3.18}$$

This expression can be broken into two parts:

$$S(\tau) \;\propto\; \mathcal{R}e\int_{-\infty}^{\infty} dt\, E_r^*(t)\, E(t) + \mathcal{R}e\int_{-\infty}^{\infty} dt\, E_r^*(t)\, E(t)\left[i\Big(\frac{2\pi L}{\lambda}\Big)\Delta n - L\Delta\alpha\right]. \tag{3.19}$$

The first integral can be ignored because it is a signal that is not modulated by the pump pulse, and so it is not measured in a pump-probe experiment. In any case, this first integral time-averages approximately to zero.

The second integral is the signal that is measured in a pump-probe experiment, and after substituting in the expression for the delayed reference and setting the bias phase to $\pi/2$, this signal can be written

$$S(\tau) \;\propto\; \gamma(\tau) \,+\, \beta(\tau)\,, \tag{3.20}$$

where

$$\gamma(\tau) \;=\; \mathcal{R}e\left(\frac{2\pi L}{\lambda}\right)\int_{-\infty}^{\infty} dt\, E^*(t-T)\, E(t)\int_{-\infty}^{\infty} dt_1\, h'(t-t_1)\, I(t_1+\tau)\,, \quad \text{and} \tag{3.21}$$

$$\beta(\tau) \;=\; \mathcal{I}m\; L\int_{-\infty}^{\infty} dt\, E^*(t-T)\, E(t)\int_{-\infty}^{\infty} dt_1\, h(t-t_1)\, I(t_1+\tau)\,. \tag{3.22}$$

The first expression $\gamma(\tau)$ contains $h'(t)$ the refractive index response function. This is the phase signal that we wish to measure (similar to Eq. (3.13)). The $\gamma(\tau)$ signal is distorted by the pulse chirp, but this effect is minor. So, it turns out that the pump-probe signals given by Eqs. (3.21) and (3.13) are nearly identical.

The second expression $\beta(\tau)$ contains $h(t)$ the response function for absorptive nonlinearities. This is the artifact signal that appears because of the chirped pulses and the delay between the probe and reference. If the pulses pulses were un-chirped, then all the terms in Eq. (3.22) would be real, and $\beta(\tau)$ would vanish because we take the imaginary part. So, by setting the bias phase to $\pi/2$, the absorptive nonlinearities are eliminated and we measure just the index nonlinearities. However, introducing chirped pulses produces a nonzero imaginary part to the integral in $\beta(\tau)$, and this causes the absorptive nonlinearities to appear in the index measurement.

Notice that the artifact signal $\beta(\tau)$ does not necessarily vanish as we move away from zero delay. This is in contrast to the behavior of a coherent artifact signal (Eq. (3.7)) which appears only when the pump and probe electric fields are overlapped. However, the index artifact $\beta(\tau)$ is not a coherent artifact; it is just a mixing of the absorptive response into the phase measurement. And if the absorption contains responses longer than the pulse width, then the artifact will appear for times longer than the pulse width.

Now we will use Eq. (3.22) to calculate $\beta(\tau)$ the artifact signal that we expect to observe. First, we need to assume a form for the absorptive response function $h(t)$. The measurements shown in Fig. 3.8 were performed below the band edge of the active region of the AlGaAs waveguide structure. As we shall see in the next chapter, below the band edge, the only nonlinear process that the absorption is sensitive to is two-photon absorption (TPA). Since TPA causes an instantaneous reduction in transmission, we will make the absorption response function an impulse: $h(t) = -\delta(t)$. For this response function, the artifact will only appear near zero delay. Substituting the expressions for chirped Gaussian pulses given above into Eq. (3.22), for the artifact signal we obtain:

$$\beta(\tau) \;=\; e^{-aT^2/2} \int_{-\infty}^{\infty} dt\, e^{-2a(t-T/2)^2} e^{-2a(t+\tau)^2} \sin(2bTt)\,. \qquad (3.23)$$

Notice that if either the chirp is zero ($b = 0$) *or* if the probe-reference offset is zero ($T = 0$), then the artifact signal vanishes.

The theoretical signals for the index response $\gamma(\tau)$ and the artifact signal $\beta(\tau)$ were computed numerically. For the index response function, we assumed a simple exponential carrier heating response. Adding the computed index response and artifact signal gives us the curves plotted in Fig. 3.9. The conditions were set to approximately those for the experimental data shown in Fig. 3.8: 100 fs pulses chirped to 150 fs, and a probe-reference delay of $T = 100$ fs. Notice that the agreement between

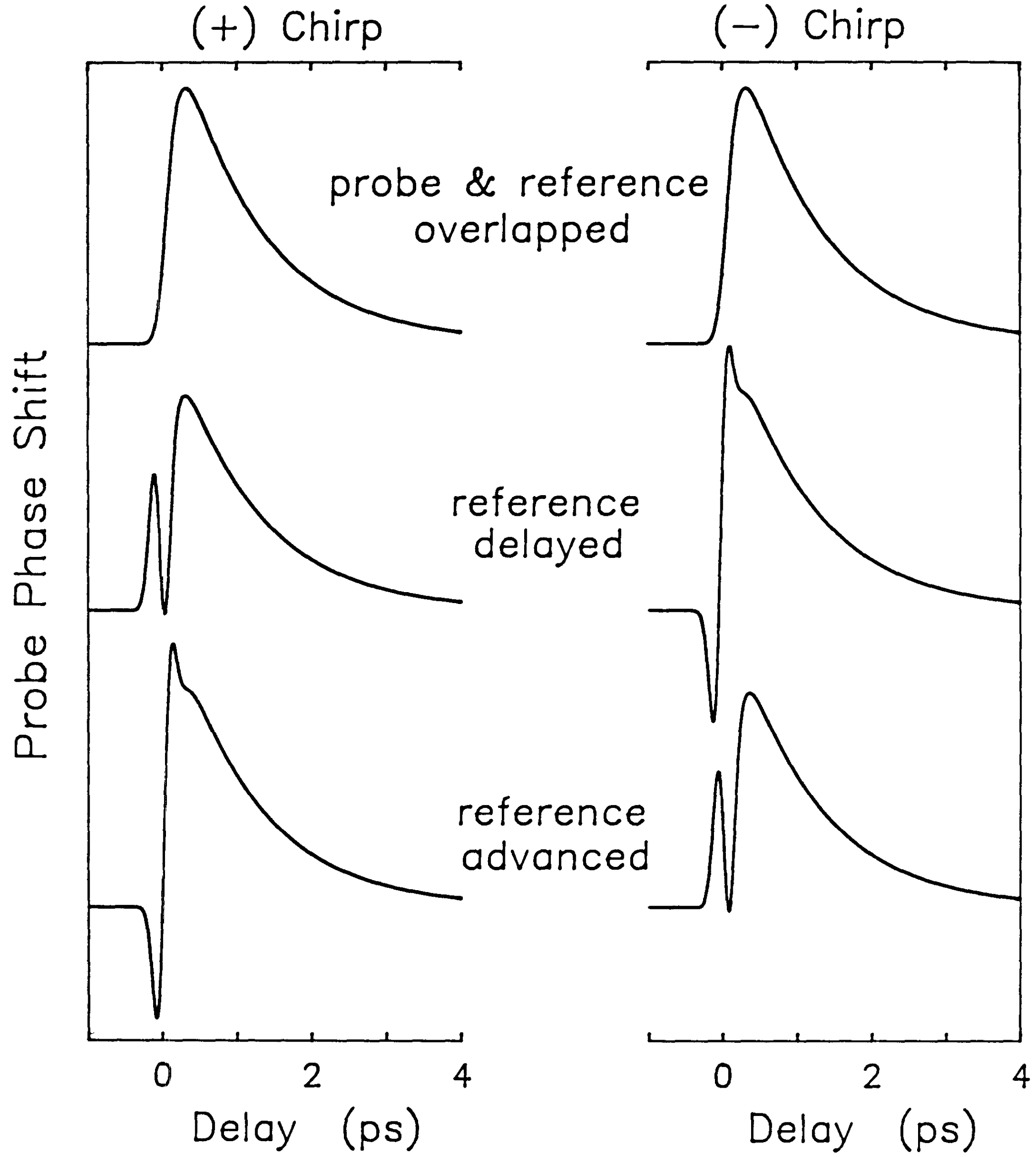

Figure 3.9: Theoretical probe phase shifts for positively and negatively chirped pulses at various probe-reference delays as indicated. Compare with Fig. 3.8.

the experimental data in Fig. 3.8 and the computed signals in Fig. 3.9 is very good. As expected, the artifact disappears when the probe and reference are overlapped.

To summarize, the index artifact results from mixing in of the gain dynamics into the measurement of the probe phase. This is caused by the chirped and delayed probe-reference pulses. This mismatch of the probe and reference phases produces a sweep in the interferometer bias about the $\pi/2$ bias point. When the interferometer bias point is swept away from $\pi/2$, the pump-induced changes in the probe amplitude show up to first order in the output signal. The sign of the bias sweep in time, positive to negative or vice versa, is determined by the sign of the pulse chirp b and the sign of the probe-reference offset T. This explains why the artifact flips sign if the pulse chirp changes sign or if the probe-reference offset is reversed. When the probe and reference pulses are chirped but not offset, no artifact is produced because the pulse phases are matched, and there is no sweeping of the interferometer. When the pulses are not chirped but are offset, again there is no artifact because the probe and reference are phase matched over their entire duration.

Thus, the index artifact is caused by absorptive nonlinearities mixing in with the refractive index measurement. In order to minimize this artifact, we need to use pulses with a minimum amount of chirp, and we need to make sure that after the TDI, the probe and reference are precisely overlapped in time. This was done in all the measurements that are described in the following chapters. As it turns out, however, an additional artifact was encountered in the refractive index measurements. This artifact generally appears at high bias currents in both the above- and below-band measurements, and it has a shape similar to the artifact that was just described. However, it could not be eliminated by playing with the pulse chirp or the probe-reference delay. This effect is not understood, but somehow the probe and reference pulses experience different phase distortions while traveling through the waveguide, and these phase distortions increase with increasing carrier density. This artifact made the performance of measurements at high carrier densities difficult, and so the bias current to the diode was generally kept below 50 mA.

3.6 Summary

At first glance, the pump-probe measurement technique appears to be an elegant and straightforward method for making time-resolved measurements of ultrafast processes.

When we consider carefully the theory behind pump-probe measurements, a number of complications arise. First, one must be sure to operate at low pump and probe powers so that the optical nonlinearities are measured in the perturbational limit. Another thing to consider is coherent artifacts caused by mixing between the pump and probe electric fields around zero delay. Finally, we have seen that measurements of refractive index dynamics can include an artifact that adds in the absorptive dynamics to the measurement. This is not a "coherent" artifact because it does not involve mixing of the pump and probe electric fields. Rather, chirp on the pulses and a probe-reference offset are the origin of this new artifact. This artifact is eliminated by minimizing pulse chirp and making sure that the probe and reference pulses are precisely overlapped in time.

Chapter 4

Below- and Above-band Measurements

The previous chapter outlined the technique for measuring ultrafast gain and refractive index dynamics in a waveguide structure. Before that, Chapters 1 and 2 detailed some of the ultrafast processes in semiconductors that are important in pump-probe measurements. To summarize, these include free carrier absorption, stimulated transitions, two-photon absorption, and the optical Stark effect (see Fig. 1.5 on page 20). We have also speculated how various dynamics will be manifested in the gain and refractive index measurements. For instance, carrier heating causes a gain compression for above-band wavelengths and a positive refractive index change that extends well below the band edge (see Fig. 2.16 on page 51).

With these preliminaries in mind, the next three chapters present various pump-probe measurements of gain and refractive index dynamics in an active AlGaAs waveguide. This chapter describes a series of above- and below-band measurements. The below-band measurements allow us to turn off effects associated with stimulated transitions and study the remaining processes separately.

4.1 Below-band gain measurements

We begin by describing below-band measurements of gain dynamics. This is a good starting point because the data is fairly easy to interpret. Below the band edge of the AlGaAs waveguide active region, the waveguide material appears transparent. For the device studied here, the band-edge was at about 855 nanometers wavelength (1.45 eV). Of the assorted ultrafast processes of interest, two-photon absorption is the only nonlinearity expected to appear in a below-band gain measurement. This is almost the case – to make things interesting, an additional small dynamic is also observed.

The measured below-band pump-probe gain dynamics should be insensitive to variations in carrier density and wavelength. Fig. 4.1 shows a series of pump-probe transmission measurements performed at 890 nanometers with the diode laser bias current varied as shown. Fig. 4.2 shows pump-probe measurements performed at a constant 30 mA bias current with the pump-probe wavelength varied as shown. As expected, the dominant ultrafast dynamic observed is an instantaneous negative transient caused by two-photon absorption. For these measurements, the average power of the pump beam in the waveguide was about 25 μW. This corresponds to a pump energy of 0.3 pJ per pulse and a peak pump power of 2.7 watts. At this level of pump excitation, we observe a probe transmission change ($\Delta T/T$) of about 6%.

In Fig. 4.2 as we approach the band edge at around 855 nm, above-band dynamics begin to appear in the data. In particular, the carrier heating dynamic and a long-lived step caused by stimulated transitions begin to appear in the response. However, for wavelengths longer than 855 nm the experimental traces all look the same. Further, Fig. 4.1 shows that the dynamics are independent of bias current as well. And so, for the below-band gain dynamics two-photon absorption is the dominant nonlinearity.

These below-band gain measurements are of interest for a few other reasons. Since the response of the two-photon absorption nonlinearity is instantaneous, the pump-probe signal $S(\tau)$ that we measure is a pump-probe cross-correlation. This can be seen by substituting $h(t) = -\delta(t)$ for the response function in Eq. (3.4) on page 54. This is a convenient way to measure how much the pulses broaden in traveling through the waveguide. Typically, a pump-probe measurement performed with 85 fs pulses yielded a signal with a 160 fs FWHM. Assuming sech(t)-shaped pulses, this deconvolves to a 104 fs pulse. Thus, pulse spreading through the diode is on the order of 22%. This pulse spreading causes the peak intensity of the pulses to decrease as they travel through the waveguide. Later on, when we compute values for n_2 the nonlinear refractive index coefficient, this pulse intensity decrease will have to be taken into account.

Below-band light allows us to determine the absorption coefficient associated with free carrier absorption. This is accomplished by measuring the power transmitted through the waveguide as a function of bias current. From this we find that the free carrier absorption coefficient α_{FCA} (cm^{-1}) is related to the diode laser bias current

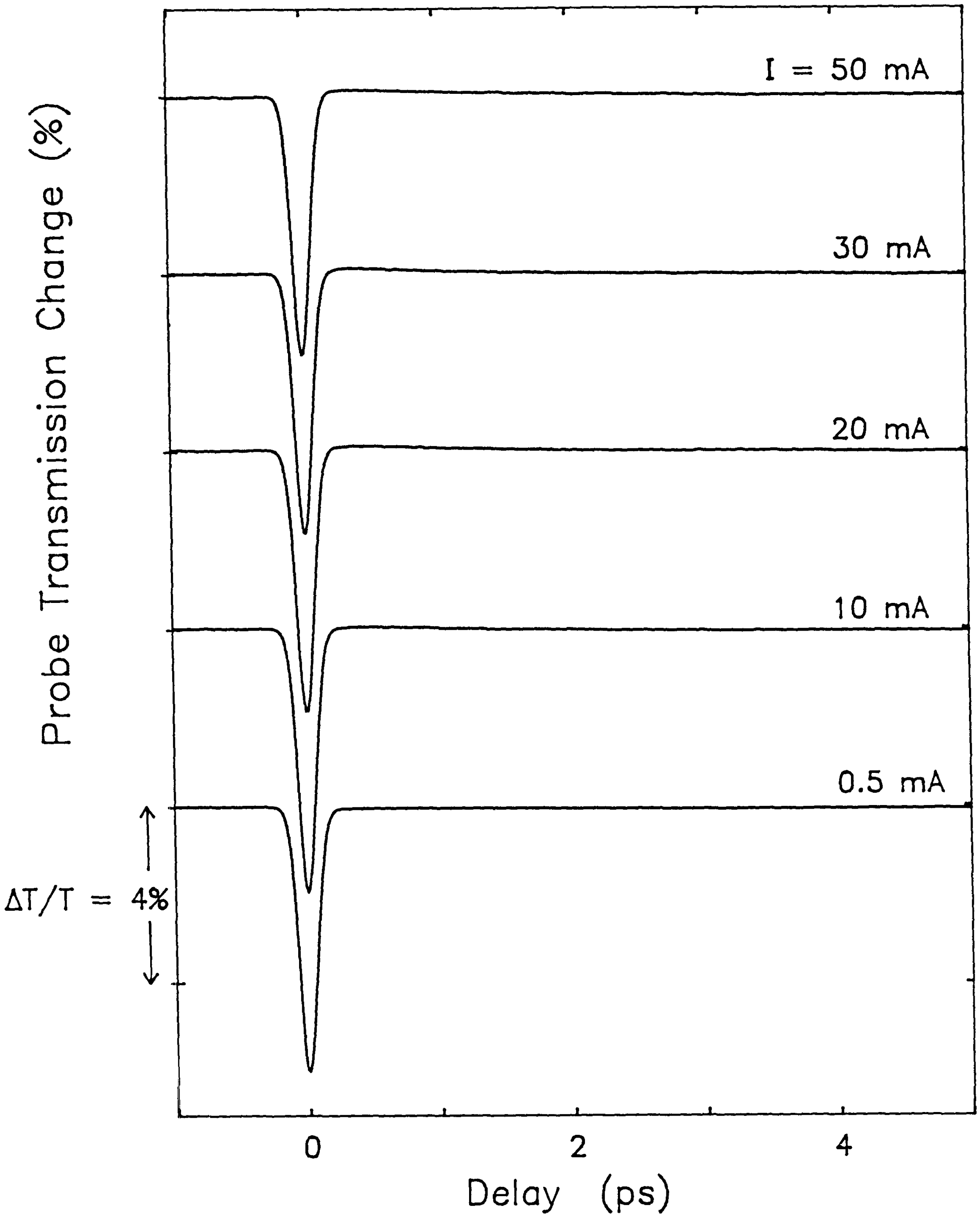

Figure 4.1: Below-band gain dynamics at 890 nanometers. The diode laser bias current is varied from 0.5 mA to 50 mA as indicated.

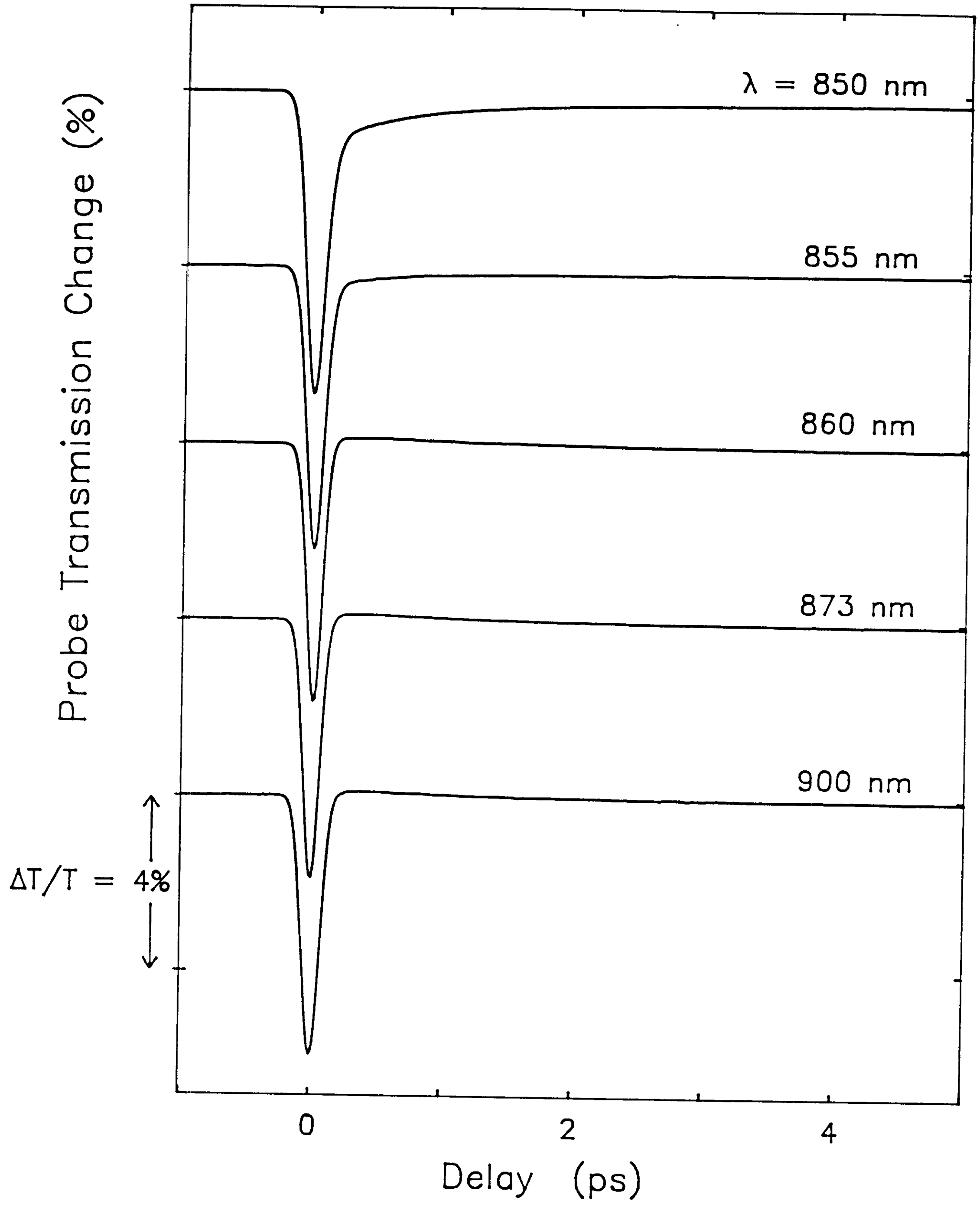

Figure 4.2: Below-band gain dynamics at 30 mA bias current. The pump-probe wavelength is varied from 900 nm to just above the band edge at 850 nm.

(mA) by $\alpha_{\text{FCA}} = 0.14I$. So, at 50 mA bias current the absorption coefficient is 7 cm^{-1}, which means that a pulse loses 19% of its energy through free carrier absorption as it propagates through the waveguide. This carrier density-dependent loss due to free carrier absorption is a non-trivial amount, and again, it will be taken into account when computing values for n_2. The cross section for the free carrier absorption process σ_{FCA} can also be determined. We use the relation $\alpha_{\text{FCA}} = \sigma_{\text{FCA}} N \Gamma$, where N is the carrier density in the active region, and Γ is the mode confinement factor. Assuming $\tau = 1$ nanosecond for the carrier lifetime, the electron and hole carrier densities at 50 mA bias current are $\sim 4 \times 10^{18}$ cm^{-3}. With $\Gamma = 0.1$, we find $\sigma_{\text{FCA}} \sim 10^{-17}$ cm^2 for the average free carrier absorption cross section for elecrons and holes.

Finally, it turns out that there is a little more than just two-photon absorption going on in these below-band gain measurements. A small, unexpected dynamic is seen when we zoom-in on the data. Fig. 4.3 shows a close-up of the constant wavelength data from Fig. 4.1, and Fig. 4.4 shows a close-up of the constant current data from Fig. 4.2. The data has been magnified by about 10 times, and a small upward gain transient is evident. This dynamic relaxes with a $\sim$ 1.1 picosecond time constant – as we shall see later on in this chapter, this is the same time constant associated with the recovery of carrier heating. As we approach the band-edge in Fig. 4.4, the positive gain change is washed-out by the above-band carrier heating dynamic.

The most likely explanation for this positive gain dynamic involves focusing and de-focusing of the waveguide mode caused by refractive index changes [89, 90]. As we shall see in the next section, heating of the carriers through free carrier absorption causes a positive refractive index transient which recovers with a $\sim$ 1.1 picosecond time constant. The amount of refractive index change is proportional to the carrier density present (notice in Fig. 4.3 how the gain transient increases with bias current). The positive index transient is localized to the active region where the carriers are confined. Increasing the refractive index causes the mode to be more tightly confined, and thus the probe propagates through the waveguide with reduced loss. As the carriers cool back to equilibrium, the index recovers – so, the mode returns to its original shape, and the probe transmission recovers to normal.

The long-lived decrease in probe transmission is attributed to carrier generation through two-photon absorption. This increase in carrier density is accompanied by a decrease in the refractive index of the active region (see Fig. 2.15 on page 51).

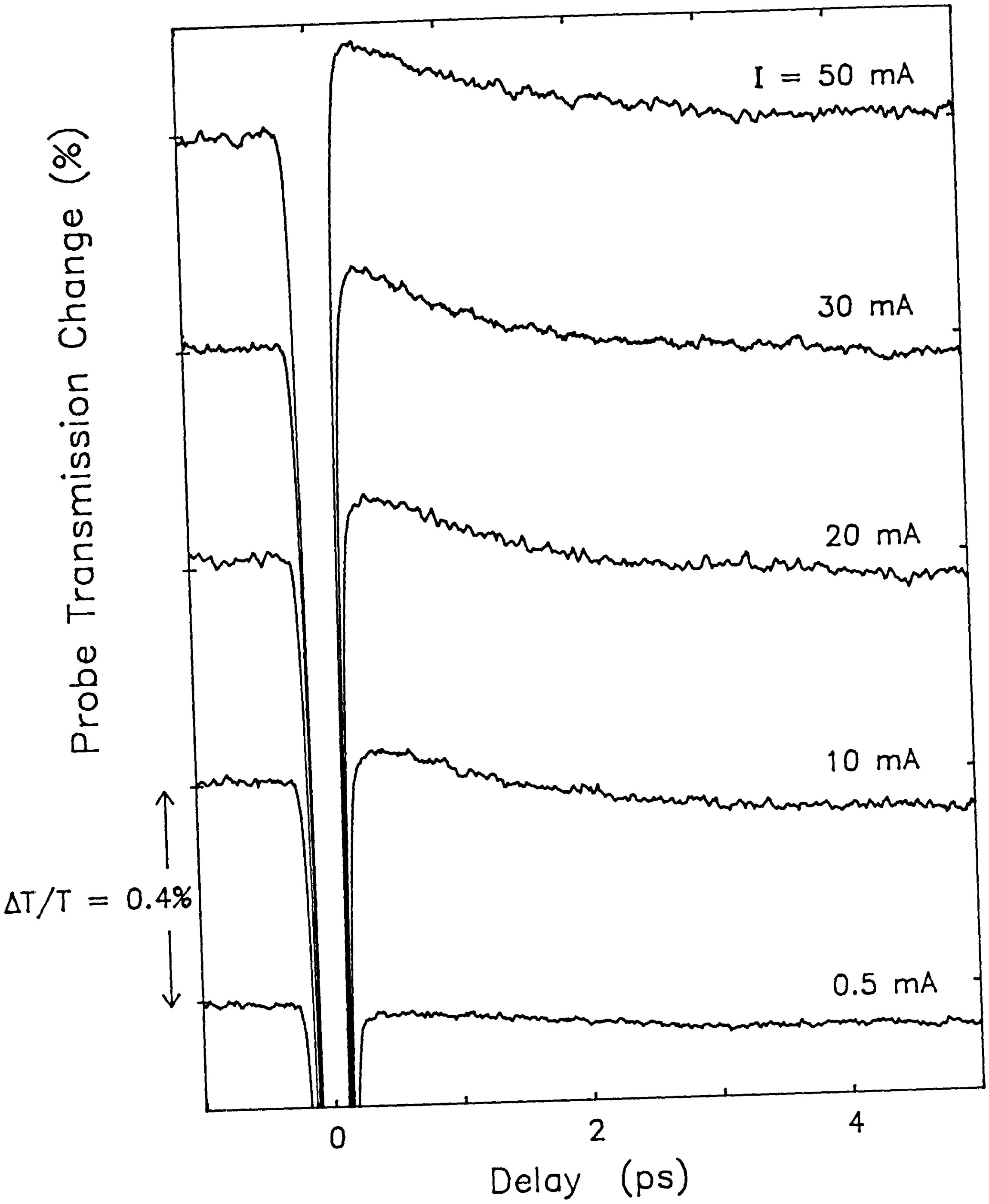

Figure 4.3: Below-band gain dynamics at 890 nanometers – close-up of data shown in Fig. 4.1.

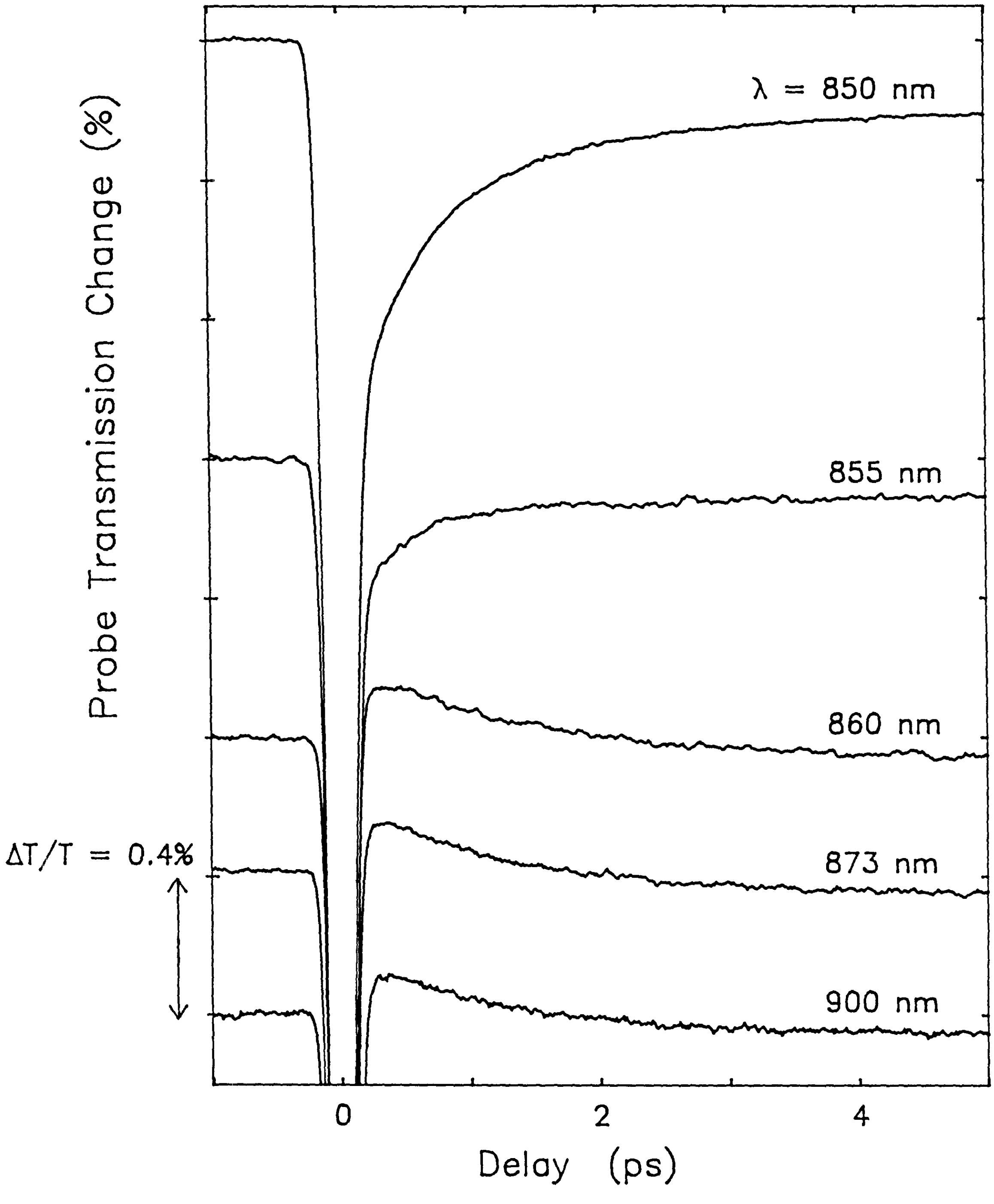

Figure 4.4: Below-band gain dynamics at 30 mA bias current – close-up of data shown in Fig. 4.2.

Decreasing the refractive index results in poorer mode confinement, and so the probe transmission decreases. This is a long-lived effect because it recovers as carriers recombine which takes on the order of a nanosecond.

Finally, there is some support for this idea of dynamic changes in the mode profile induced by carrier heating and carrier density changes. Work by Van Der Ziel [89] has shown that self-focusing of the optical mode can be caused by depletion of the carrier density. Here, we suspect that the opposite is happening – increasing the carrier density leads to defocusing of the mode. Also, a recent paper by Botkin *et al.* [90] supports the idea that ultrafast carrier temperature changes can cause ultrafast changes in the optical mode.

4.2 Below-band index measurements

To complete the investigation of below-band dynamics, this section presents the results of below-band refractive index measurements. As in the previous section, these measurements are performed as a function of wavelength and carrier density. Unlike the below-band gain dynamics, however, the below-band refractive index measurements reveal a great deal about processes that occur above-band. The reason for this is that the below-band refractive index is affected by the above-band processes. This happens because, as elucidated by the Kramers-Kronig transform, the refractive index at a given wavelength depends on the gain at *other* wavelengths. Figs. 2.15 (page 50) and 2.16 demonstrate this for carrier density changes and carrier temperature changes. And so, while the below-band gain does not sense carrier density or carrier temperature changes, the below-band refractive index exhibits a response to these above-band effects.

Fig. 4.5 shows the measured probe phase shift at 882 nm with the diode laser bias current varied from 1 mA to 45 mA. Recall that the probe phase shift is directly proportional to the pump-induced refractive index change in the waveguide through $\Delta\phi/2\pi = \Delta nL/\lambda$. In contrast to the below-band gain dynamics, the index exhibits more than just an instantaneous response, and the dynamics are strongly affected by the carrier density in the active region. At low currents, there is an instantaneous negative transient that disappears as the current is increased. This dynamic is attributed to the optical Stark effect. As the current is increased, a positive index change appears and eventually dominates the index response at the higher currents.

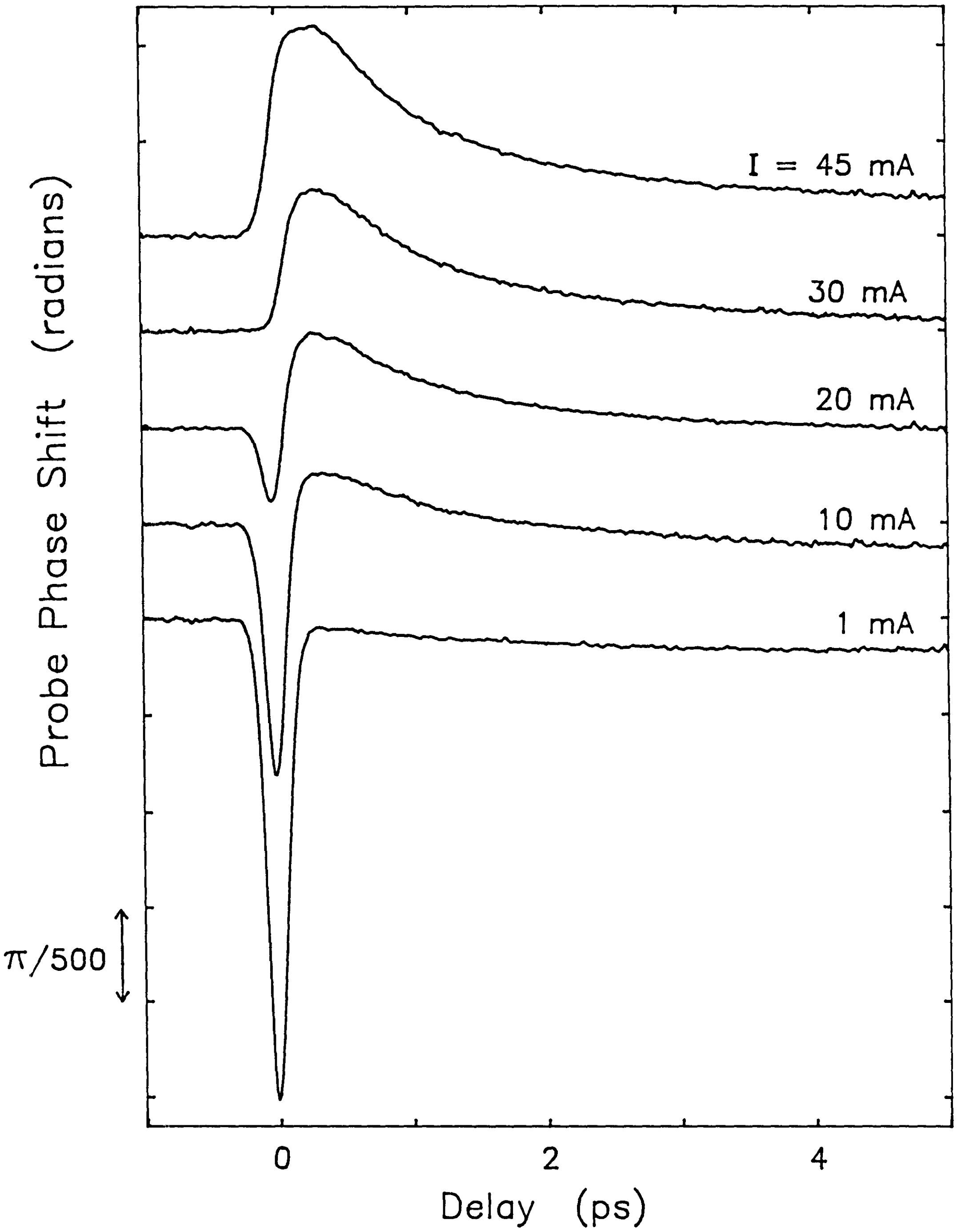

Figure 4.5: Below-band refractive index dynamics at 882 nanometers. The diode laser bias current is varied from 1 mA to 45 mA as indicated.

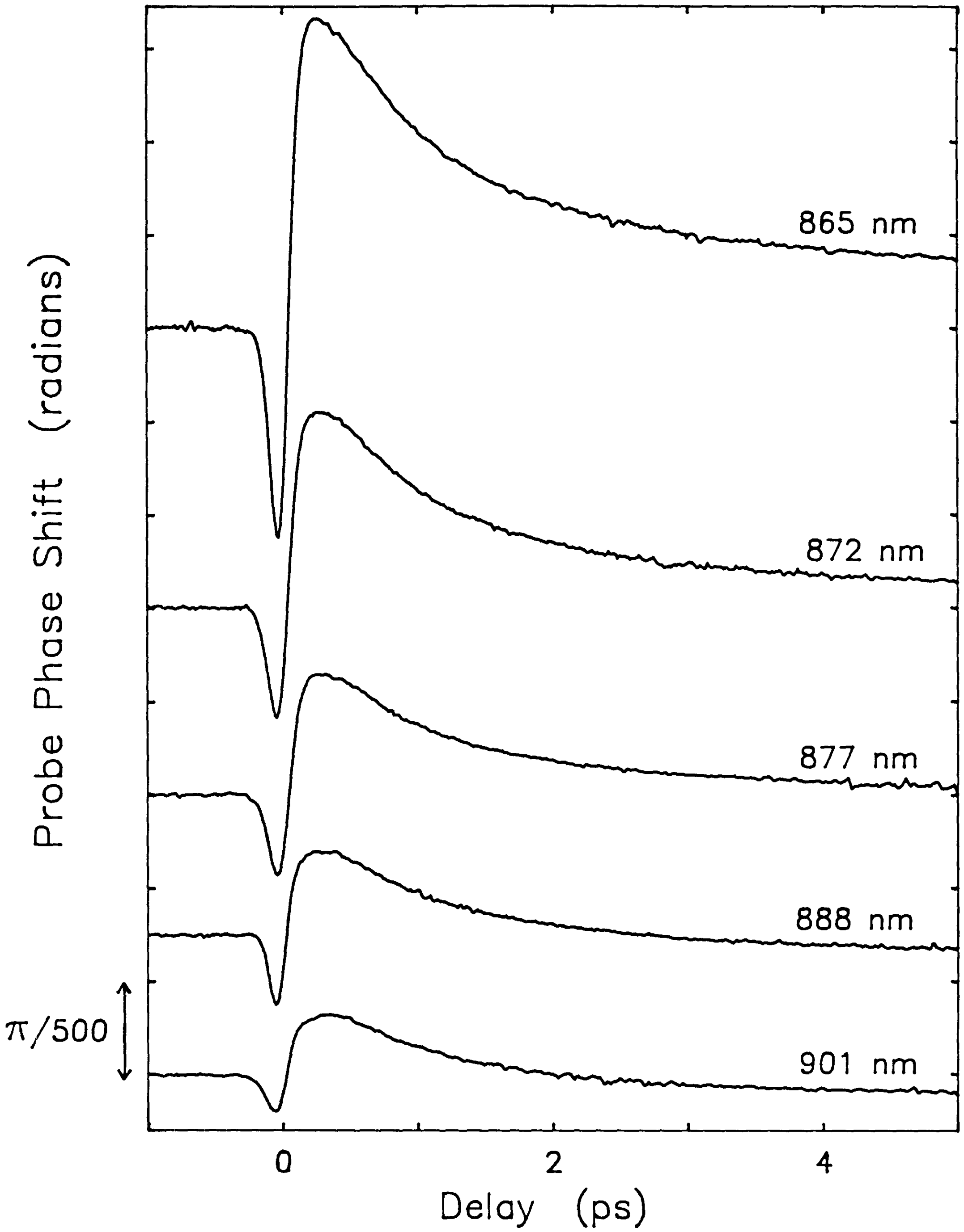

Figure 4.6: Below-band refractive index dynamics with the diode laser bias current fixed at 20 mA. The pump-probe-reference wavelength is tuned from 901 nm to 865 nm.

This positive index change is caused by carrier heating, and the ~1.1 ps time constant recovery is associated with the cooling of the carriers back to equilibrium.

Fig. 4.6 shows the wavelength dependence of the below-band index dynamics. The bias current is set at 20 mA, and the pump-probe-reference wavelength is tuned from about 46 nanometers below the band edge to about 10 nanometers below the band edge. Again, the negative instantaneous transient and the positive carrier heating dynamic are present throughout this wavelength range. As we tune away from the band edge, the size of these dynamics decreases. This is consistent with the resonant behavior of the Kramers-Kronig relation – the size of the index changes falls off as we tune away from an absorptive feature. In this case, the absorptive features are above-band carrier dynamics such as carrier heating.

One thing to notice in Figs. 4.5 and 4.6 is that the TDI can resolve probe phase shifts as small as $\pi/1000$ radians (0.18 degrees). This corresponds to a modal refractive index change of $\sim 10^{-6}$ (or $\Delta n/n \sim 4 \times 10^{-7}$). This high resolution is an indication of both the sensitivity of the TDI measurement technique as well as the stability of the Ti:sapphire laser system.

Since stimulated transitions do not occur with below-band excitation, the only mechanisms for heating the carrier distribution are free carrier absorption and two-photon absorption. Both processes put up carriers high into the bands. As these excited carriers relax, they scatter with and lose energy to the sea of free carriers at the bottom of the band, resulting in a heated carrier distribution. In Fig. 2.16 on page 51 we saw that heating the carriers leads to a positive refractive index change. As the carriers cool back to their equilibrium temperature through phonon emission, the refractive index recovers as well. The carrier cooling is seen in the data as the tail that recovers after about 4 picoseconds. When the data is fit to a response function (as described later on in this chapter), we see that this recovery process has a time constant of $\sim$ 1.1 picoseconds. All of the carrier cooling dynamics we will see exhibit this characteristic 1.1 picosecond time constant.

One thing that is not evident from looking at the data is a delay in the turn-on of the carrier heating process. That is, there is a delay of about 120 fs in the response of the carrier heating dynamic – the carriers do not heat up instantaneously. Rather, it takes a finite amount of time for the excited carriers to interact with and heat up the carrier distribution that sits at the bottom of the band. These findings are based on the fits to be presented at the end of this chapter.

Although both free carrier absorption and two-photon absorption of the pump pulse contribute to carrier heating, the data in Fig. 4.5 suggests that free carrier absorption is the dominant process in these perturbational measurements. The two-photon absorption process is not strongly dependent on carrier density, as we saw in Fig. 4.1. Free carrier absorption, however, is directly proportional to the carrier density. We see in Fig. 4.5 that the carrier heating dynamic increases with carrier density. As the carrier density goes up, the amount of free carrier absorption increases, resulting in a larger carrier heating dynamic. This suggests that free carrier absorption is primarily responsible for the carrier heating dynamic seen here. Of course, at high pump excitation, one would expect two-photon absorption to eventually dominate because of its I^2 dependence. Indeed, this effect is observed experimentally in measurements with large pump powers. These high power measurements will be discussed two chapters from now.

The other nonlinearity of interest in these measurements is the negative instantaneous index dynamic that decreases as the carrier density is increased. We attribute this response to the optical Stark effect, although there may be additional contributions from the two-photon absorption process [91, 92, 93]. The optical Stark effect is a virtual process in which an electromagnetic excitation modifies the electronic energy levels of a material. In atoms, optical excitation below a transition energy results in the repulsion of the two energy levels. In semiconductors, although the situation is much more complicated, the result is similar. Below-band excitation causes an instantaneous blue-shift of the band edge – the electronic states are pushed away from the optical excitation. The Kramers-Kronig relations show that the blue-shifting of an absorption feature causes a negative refractive index change. And since this is a resonant process, the closer we approach the absorption edge, the larger the index response is. This is consistent with our observation of a negative instantaneous index transient that increases as we tune towards the band edge (Fig. 4.6). Furthermore, by injecting carriers into the active region, the absorption edge is effectively shifted away in energy from the probe wavelength. Again, this is consistent with our observation that the instantaneous dynamic decreases as we turn up the diode laser bias current, since this is just like tuning away from the absorption edge (Fig. 4.5).

Theoretical support for this interpretation of the instantaneous index transient is provided in work by Sheik-Bahae *et al.* [91, 92, 93]. Using a two-band model to compute absorption changes and then applying a Kramers-Kronig transform, Sheik-

Bahae calculates the dispersion of the nonlinear refractive index coefficient n_2. Our results are in good agreement regarding the existence and dispersion of this negative refractive index transient. One discrepancy is that we do not observe a predicted sign flip of this transient at high carrier densities. It is possible, however, that the carrier density in these measurements was not high enough to observe this. Also, Sheik-Bahae has predicted a delay in the response of the optical Stark effect, analogous to the delay in the onset of carrier heating that we observe. However, based on our fits to the data, such a delay has not been observed. This delay may be faster than 100 fs, in which case, the pulses used here may not be short enough to resolve such a process.

Finally, there are long-lived index dynamics that appear in these below-band measurements. In Fig. 4.5 at low carrier densities we observe a negative index change for long delay times. This index decrease is caused by carriers generated through two-photon absorption. Eventually, at higher carrier densities the index change turns positive. This positive index change is attributed to the heated carriers giving off their heat to the lattice, which results in a long-lived positive index change. The amount of carriers put up through two-photon absorption does not vary much with carrier density. However, at high carrier densities, the carrier heating dynamic is large, resulting in a larger lattice temperature increase. Thus, at high carrier densities the lattice heating eventually dominates the negative index change caused by two-photon absorption.

4.3 Above-band gain and index measurements

Having performed below-band measurements where we saw the effects of two-photon absorption, carrier heating, and the optical Stark effect, we now tune above the band edge. In addition to all the previous dynamics, we now have effects associated with stimulated transitions: carrier density changes, spectral hole burning, and carrier heating and cooling. The starting point for understanding the above-band gain and index dynamics is the semiconductor gain curve shown in Fig. 2.9 on page 43. If we fix the diode laser amplifier bias current, we can tune the laser wavelength to investigate the gain, transparency, and absorption regimes. The results of this investigation are presented in Figs. 4.7 and 4.8.

Fig. 4.7 shows the above-band gain dynamics, and Fig. 4.8 shows the above-band refractive index dynamics. In both figures the bias current is set at 28 mA, and the wavelength is tuned to the gain, transparency, and absorption regimes. The pump, probe, and reference powers used in these above-band measurements were approximately the same as for the below-band measurements. Notice that the above-band phase shifts are about 10 times larger than the below-band phase shifts, a result of the enhancement of the index change as we tune towards and into the band.

The long-lived gain dynamics in Fig. 4.7 can be understood in terms of carrier density changes. In the gain regime, the pump pulse is amplified, causing a *decrease* in carrier density. The probe pulse following the pump sees a reduced gain, and so there is a long-lived decrease in probe transmission. This step gain change recovers on a nanosecond time scale as the carrier densities recover to their quasi-equilibrium levels. In the absorption regime, the pump pulse generates carriers causing an *increase* in the carrier density. This results in a long-lived transmission increase for the probe. And finally, between the gain and absorption regimes sits the transparency point where the optical gain and loss are equal. The pump does not stimulate any net carrier density change at transparency, and so the probe experiences no long-lived gain change. The transparency point is an interesting operating point because the stimulated transitions are effectively turned off even though we are operating above the band edge.

The long-lived index changes in Fig. 4.8 follow the same analysis. In the gain regime, the pump-induced reduction in carrier density is accompanied by an increase in the refractive index. The absorption regime sees an index decrease caused by increasing the carrier density. And finally, at the transparency point there is little or no index step. (In the next chapter, we will see that there is actually a small thermally-induced index step at the transparency point, but for now it is not important.)

Moving on to the ultrafast dynamics, let us look at how carrier heating shows up in the gain and index response. Heating up the carriers results in a uniform gain compression across the gain curve (see Fig. 2.11 on page 45). Indeed, in Fig. 4.7 in all three regimes of operation we see a gain decrease that recovers with a ~ 1.1 picosecond time constant. From Fig. 2.16 on page 51, we see that carrier heating causes a positive refractive index change. And in Fig. 4.8 we see a positive index transient in all three regimes of operation that also recovers with a ~ 1.1 picosecond time constant. The fact that the time constant for the recovery of this dynamic is the same for both the gain and index helps confirm that a single process is responsible

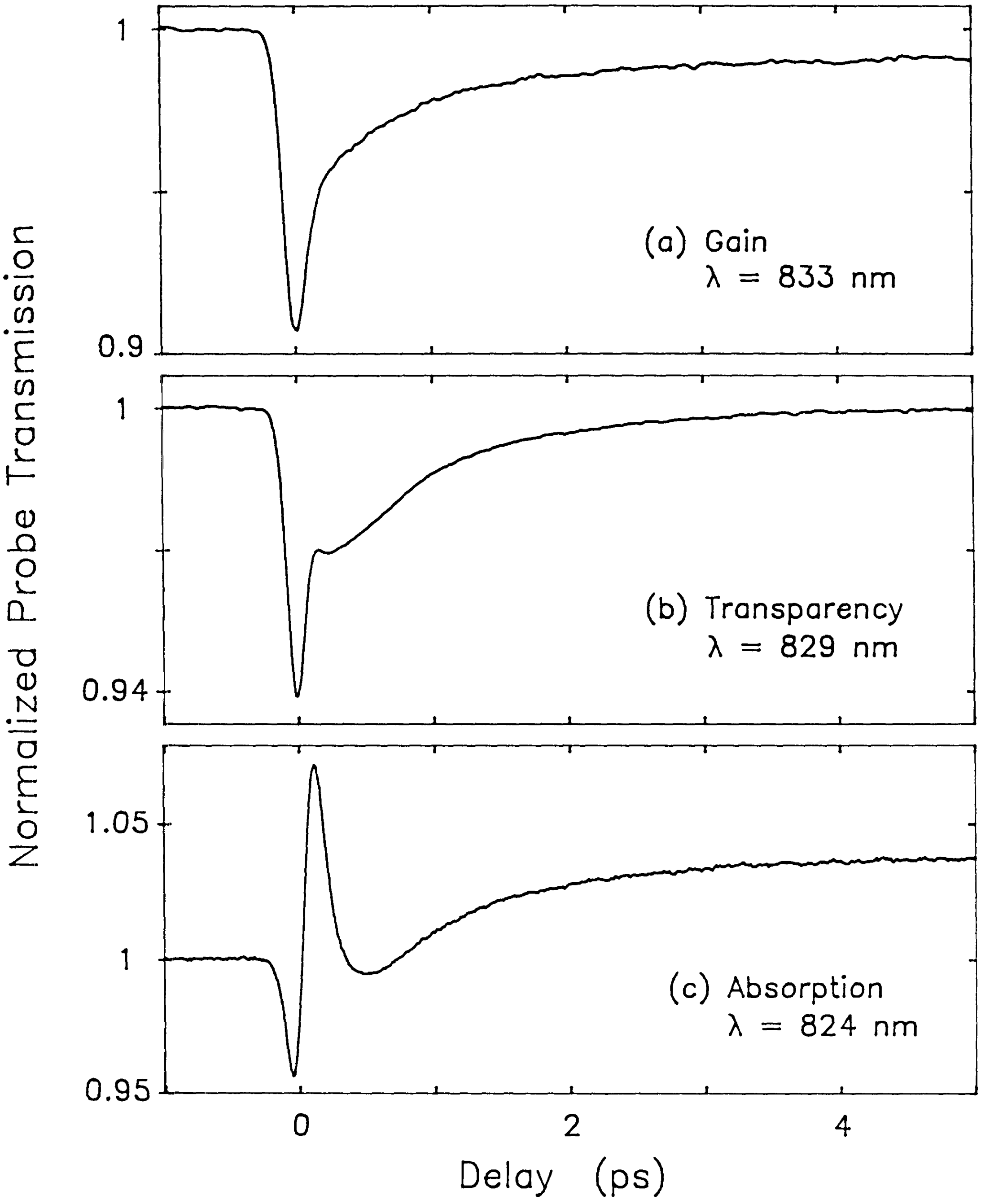

Figure 4.7: Above-band gain dynamics with the diode laser bias current set at 28 mA. The pump-probe wavelength is tuned as indicated to access the (a) gain, (b) transparency, and (c) absorption regimes.

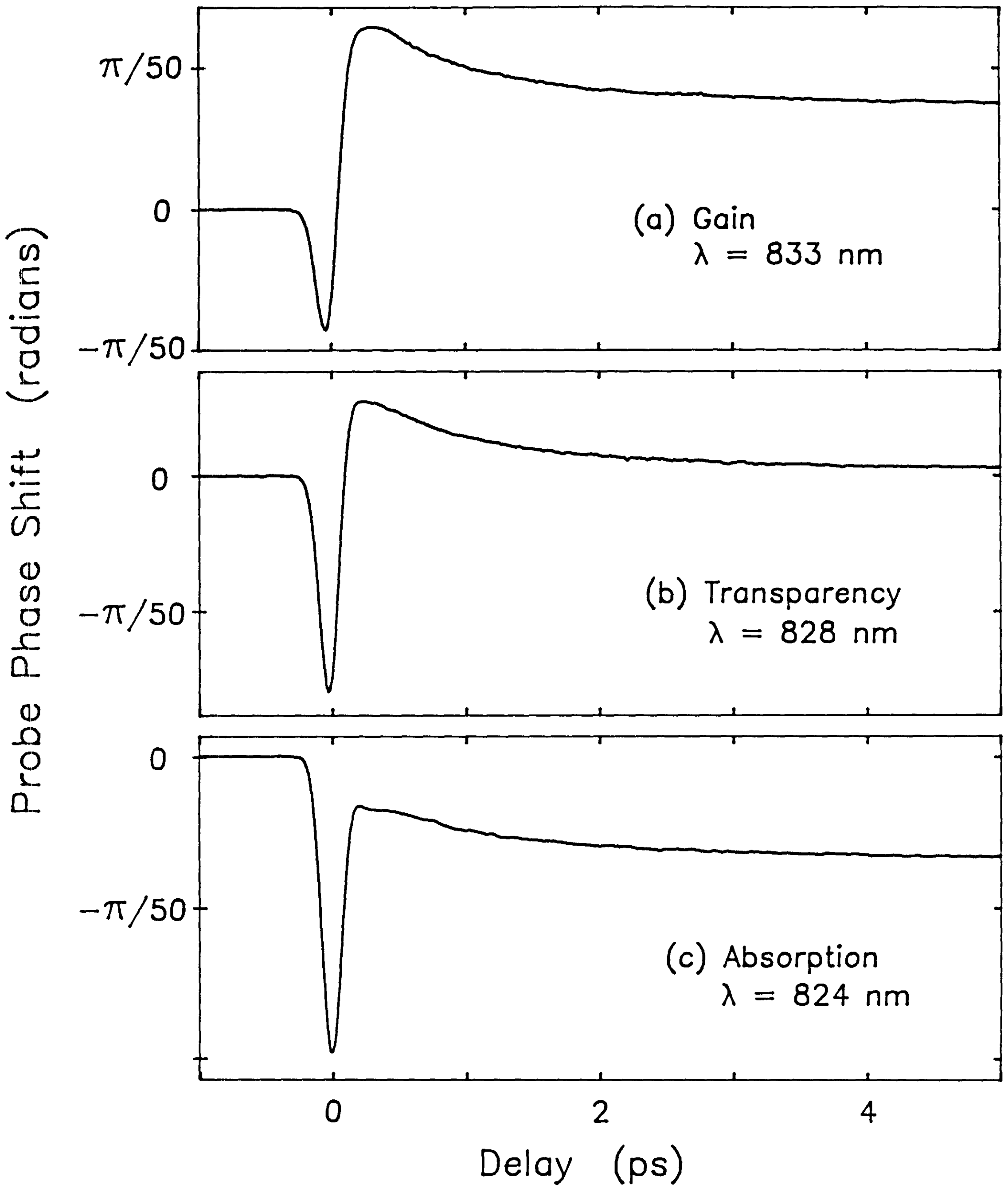

Figure 4.8: Above-band refractive index dynamics with the diode laser bias current set at 28 mA. The pump-probe wavelength is tuned as indicated to access the (a) gain, (b) transparency, and (c) absorption regimes.

for both dynamics. As we will discuss in the next section, fitting the data to a theoretical response function reveals that there is a delay in the turn-on of the carrier heating dynamic. The carrier heating response of the gain at the transparency point (Fig. 4.7b) exhibits a small cusp that is consistent with a delay in the carrier heating dynamic. In the next chapter, we will explore the gain dynamics at the transparency point in greater detail.

The next ultrafast dynamic of interest is an instantaneous transient that appears in both the gain and index. The negative gain transient is caused by two-photon absorption – the same process that dominates the below-band gain measurements. The negative index transient is the same dynamic we observe in the below-band index measurements, and we attribute this to the optical Stark effect as well as two-photon absorption [91, 92, 93]. The size of this index change is larger than in the below-band case because we are above the band-edge and close to the large density of absorbing states that lie at higher energies.

Finally, in the gain measurements we observe a strong positive transient in the absorption regime (Fig. 4.7c). This transient recovers with a $\sim$ 120 femtosecond time constant. There is no evidence for a similar response in the refractive index data. The likely cause for this feature is spectral hole burning. In the absorption regime, the pump puts up carriers because it is partially absorbed. In the long-lived gain dynamics, this causes a positive step response. However, before these carriers relax to an equilibrium distribution, they remain for a short time in a narrow spectral range roughly matching the spectrum of the pump. This causes the probe to see a transient gain increase. The carriers scatter and relax into a uniform distribution very rapidly, and so, the transient gain increase recovers rapidly as well. At the transparency point, there should be no spectral hole burning signal since there is no stimulated carrier density change. In the gain regime, there should be a negative gain change caused by the pump depletion of carriers in a narrow spectral range.

The theoretical fits to the data at transparency and in the gain regime do not contradict these observations, but they do not provide strong proof for spectral hole burning either. Since the spectral hole recovers on a time scale comparable to the pulse width, fitting the data is an ambiguous process. Fitting dynamics comparable to the pulse width can be tricky because small shifts in zero delay can give large changes in the response function one derives from the fit. Nevertheless, the gain response in the absorption regime does provide support for spectral hole burning. Since this feature has also been seen in InGaAsP devices operating at 1.5 μm [22, 32], we can be confident that it is not the result of any peculiarities of the device or material that we are studying.

Additional support for spectral hole burning is provided by the lack of any transients with a $\sim$ 120 femtosecond time constant in the refractive index data other than the delay in carrier heating. Given a spectral hole in the gain spectrum, the corresponding index response can be derived by performing a Kramers-Kronig transform. To the extent that the spectral hole is symmetric about the center wavelength of the pump, the index response will be zero at the center wavelength. Thus, a spectral hole should produce little index change as seen by a probe pulse at the same wavelength as the pump. The theoretical fits to the data support this idea – little or no spectral hole-like response is seen in the index data at any operating point.

4.4 Data fitting and analysis

In this section we outline the methods for fitting the data to a theoretical response function. This fitting technique allows us to pull out numbers from the pump-probe data. We can obtain the time constants of the dynamics, and we can quantify how the assorted dynamics change as the wavelength and carrier density are varied. This allows us to identify and characterize the physical processes that are the source of the various gain and refractive index dynamics. It also allows us to compare our data with experimental results obtained through other measurement techniques or on other devices. Fitting the data will also enable the measurement of the nonlinear refractive index coefficient n_2.

In this section, we also hope to convey some of the limitations of the data fitting procedure. As mentioned in the previous section, fitting the data is not an exact science. Small shifts in zero delay can alter the theoretical response function that is generated. Thus, we must be careful when dealing with the dynamics that occur on a time scale comparable with the pulse width. Other processes, such as the relaxation of the carrier temperature can be easily characterized by fits since this dynamic recovers on a picosecond time scale.

As discussed in Chapter 3 (Eq. (3.4)), the measured pump-probe signal $S(\tau)$ is the response function $h(t)$ convolved with the pulse intensity autocorrelation $G^{(2)}(t)$. This relation is outlined schematically in Fig. 4.9. The pulse autocorrelation and the pump-probe signal are obtained experimentally, and our goal is to pull out the response function $h(t)$. This is done by guessing a form for $h(t)$, performing the convolution, and comparing the computed $S(\tau)$ with the actual data. After iterating this procedure a few times, a response function is eventually found that gives a good fit to the data.

The form for the response function that is used to fit all the data presented in this thesis is:

$$h(t) = u(t)\left[a_0 + a_1(1 - e^{-t/0.12\mathrm{ps}})e^{-t/1.1\mathrm{ps}} + a_2 e^{-t/0.12\mathrm{ps}}\right] + a_3\delta(t)\,, \qquad (4.1)$$

where the unit step function $u(t)$ ensures causality: $h(t < 0) = 0$. Granted, this response function contains several adjustable parameters, which apparently provides a great deal of freedom in fitting the data. However, each term in the response function is attached to a specific physical process, and the fits are always constrained by the behavior expected for each of these processes. Figs. 4.9 and 4.10 break down the gain and refractive index response functions into the separate processes. The a_0 step function term represents the long-lived stimulated carrier density change. The a_1 term is the carrier heating response – the 0.12 ps term gives the delay in heating of the carriers, and the 1.1 ps term describes the cooling back to equilibrium. The a_2 term represents spectral hole burning – so, for the refractive index response function we set $a_2 = 0$. Finally, the delta function describes the instantaneous processes, two-photon absorption and the optical Stark effect. There is a certain amount of play in the time constants used in the fits. The delay in the heating-up of the carriers is described by an exponential term with a 120 femtosecond time constant. In some cases, good fits were obtained with time constants from 100 to 140 femtoseconds. In general, the time constants could be varied by $\pm 15\%$, and good fits were still obtained.

Only the a_0 and a_2 terms change signs depending on the operating regime. In the absorption regime, a_0 and a_2 are positive for the gain dynamics, and a_0 is negative for the index dynamics ($a_2 = 0$ for the index). These terms flip sign in the absorption regime, and at transparency $a_2 = a_0 = 0$, since there are no stimulated transitions. For carrier heating, $a_1 < 0$ for the gain response, and $a_1 > 0$ for the index response. And finally, $a_3 < 0$ for the instantaneous processes.

In Fig. 4.11, the theoretical pump-probe signal for the gain and refractive index data in the absorption regime is broken down into the separate dynamics. Adding to-

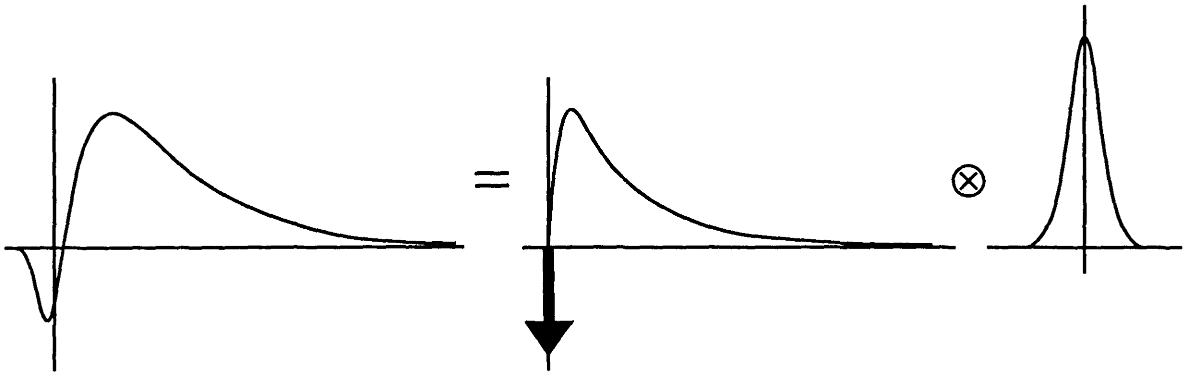

$$\text{Pump - probe signal:}\quad s(\tau) = h(t) \otimes G^{(2)}(t) = \int_{-\infty}^{\infty} dt\ h(\tau-t)\cdot G^{(2)}(t)$$

$G^{(2)}(t)$ = pulse intensity autocorrelation

$h(t)$ = response function

$= a_0$ stimulated carrier density change

$+ a_1\,[1-e^{-(t/0.12\text{ ps})}]\,e^{-(t/1.1\text{ ps})}$ carrier heating

$+ a_2 e^{-(t/0.12\text{ ps})}$ spectral hole burning

$+ a_3\,\delta(t)$ instantaneous response

Figure 4.9: Schematic of data fitting procedure. The pump-probe signal is generated by convolving the pulse intensity autocorrelation with a theoretical response function.

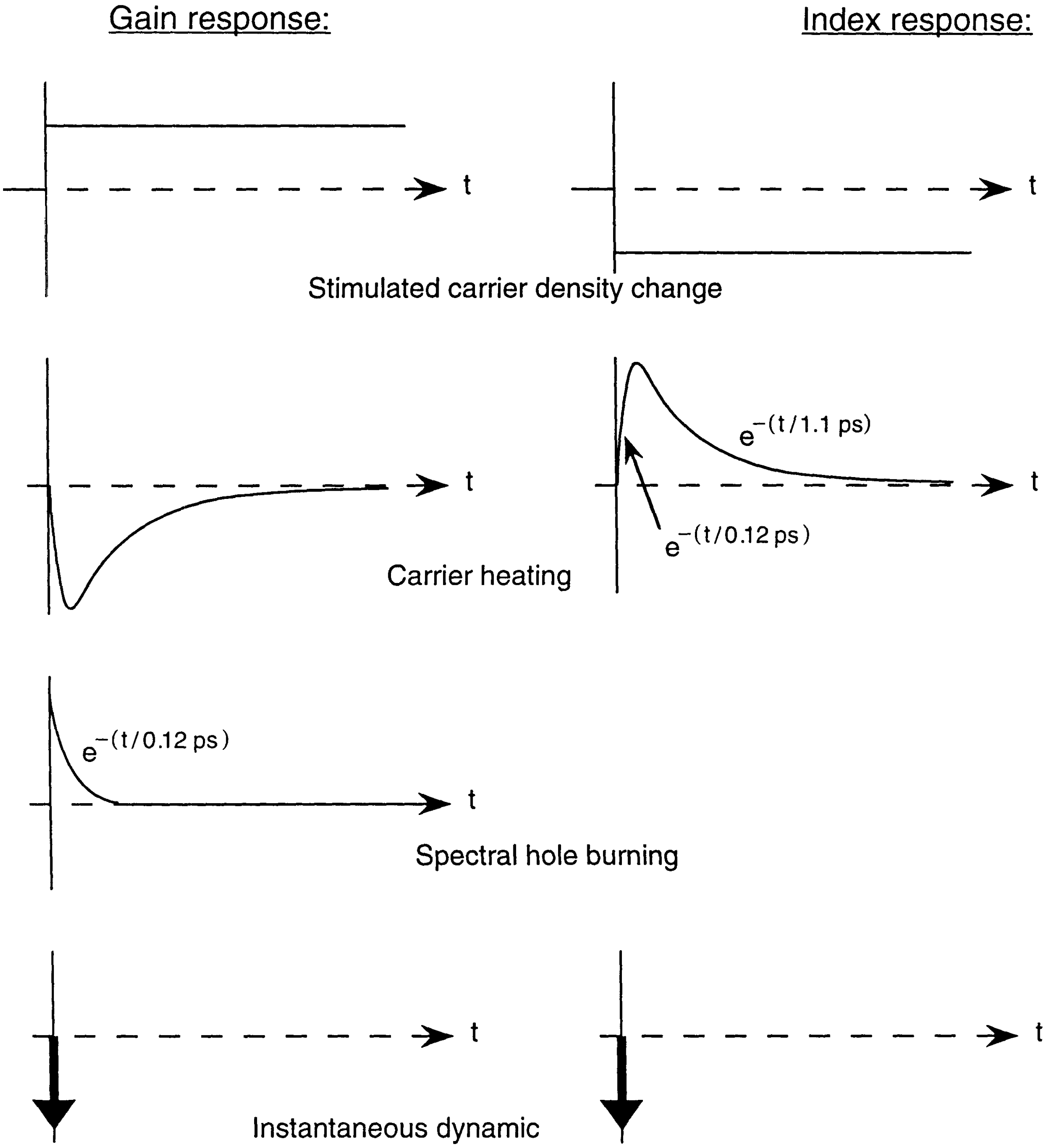

Figure 4.10: Response function used to fit the measured gain and refractive index dynamics. Stimulated carrier density changes have a step response. The carrier heating response contains a delay. Spectral hole burning is only present in the gain response. And instantaneous processes such as two-photon absorption and the optical Stark effect are modeled with a delta function.

gether the instantaneous, carrier heating, step, and spectral hole burning components gives the theoretical pump-probe signal $S(\tau)$.

Finally, the fits to the above-band gain and refractive index data are shown in Figs. 4.12 and 4.13. The solid lines are the data from Figs. 4.7 and 4.8, and the dashed lines are the theoretical fits obtained using the response function in Eq. (4.1). The fit to the cusp in the gain dynamics at the transparency point is provided by the delayed carrier heating response. Notice that just because Eq. (4.1) yields a good fit to the data does not prove it is the correct response function. Indeed, we could eliminate the delay in carrier heating but still fit the data at transparency by making a_2 nonzero. However, having spectral hole burning at the transparency point is nonphysical. Thus, although fitting the data is not conclusive, the response function that we obtain is appealing on physical grounds.

Carrier cooling is described by an exponential with a 1.1 ps time constant. However, carrier cooling is not necessarily an exponential process. Better fits to the carrier cooling dynamics were obtained using two exponentials with 2 ps and 0.6 ps time constants. This does not prove, however, that there are two distinct processes going on – for instance, electrons and holes cooling at two different rates. There is only so much information that can be pulled out of the pump-probe measurements. So, a 1.1 ps time constant was chosen because it provided the best one component fit to the data.

Fits to below-band refractive index data are shown in Fig. 4.14. The same response function from Eq. (4.1) is used with the spectral hole burning term a_2 set to zero. In the figure, two data traces are fit in two ways – with and without the carrier heating delay. The fits with delayed carrier heating round out the data at the peak and give a much better fit than without the carrier heating delay. Thus, these below-band fits provide strong evidence that there is indeed a delay in the onset of carrier heating. The above-band gain and index fits are not as definitive because there is always the possibility that the spectral hole burning process is creating an apparent carrier heating delay.

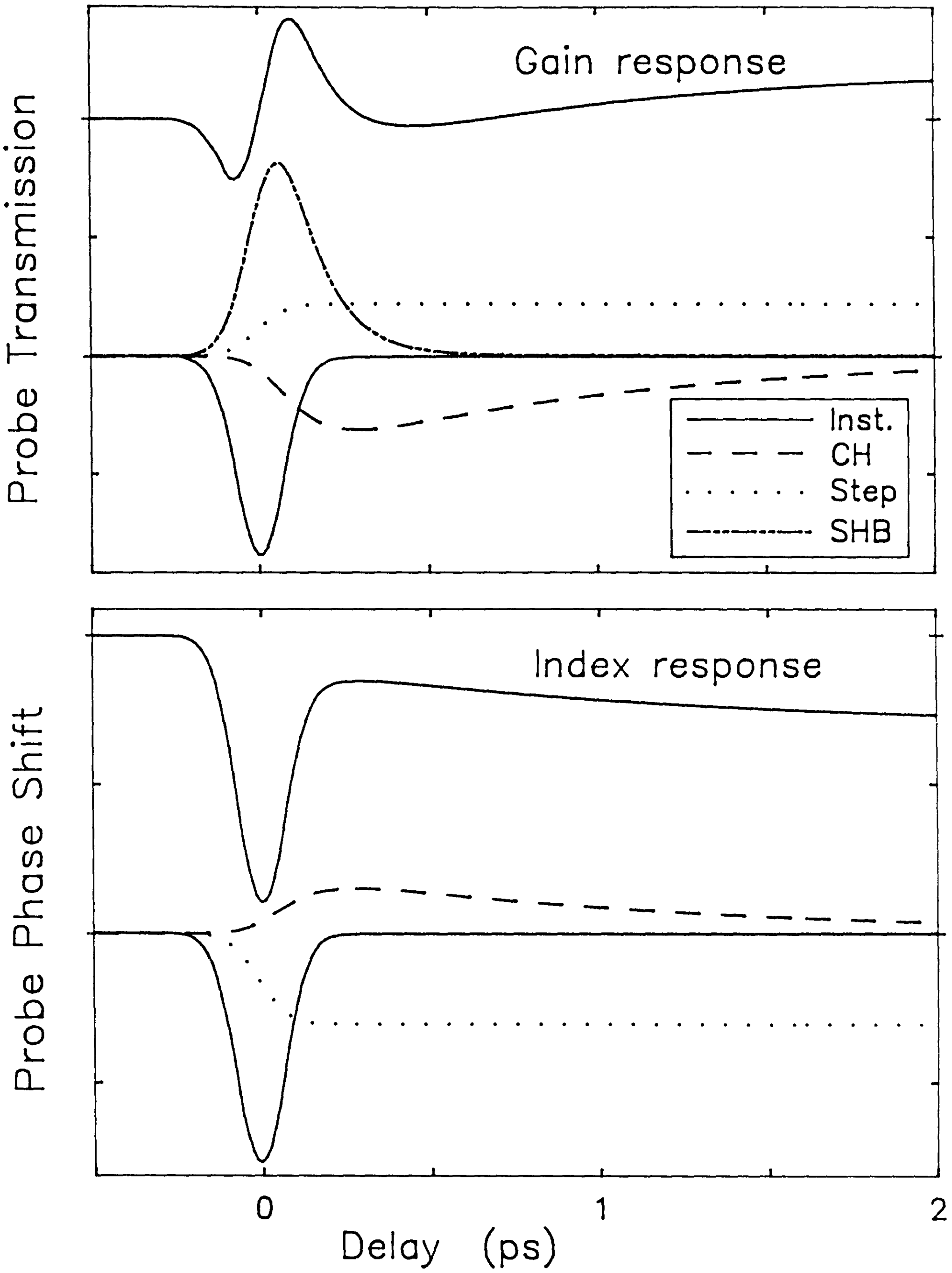

Figure 4.11: Fits to gain and refractive index data in the absorption regime broken down into the various processes. The solid line is the instantaneous contribution, the dashed curve is the carrier heating response, the dotted curve is the step response, and the dashed-dotted curve is the spectral hole burning dynamic. The solid curve at the top of each figure is the net response obtained by summing the individual responses below it.

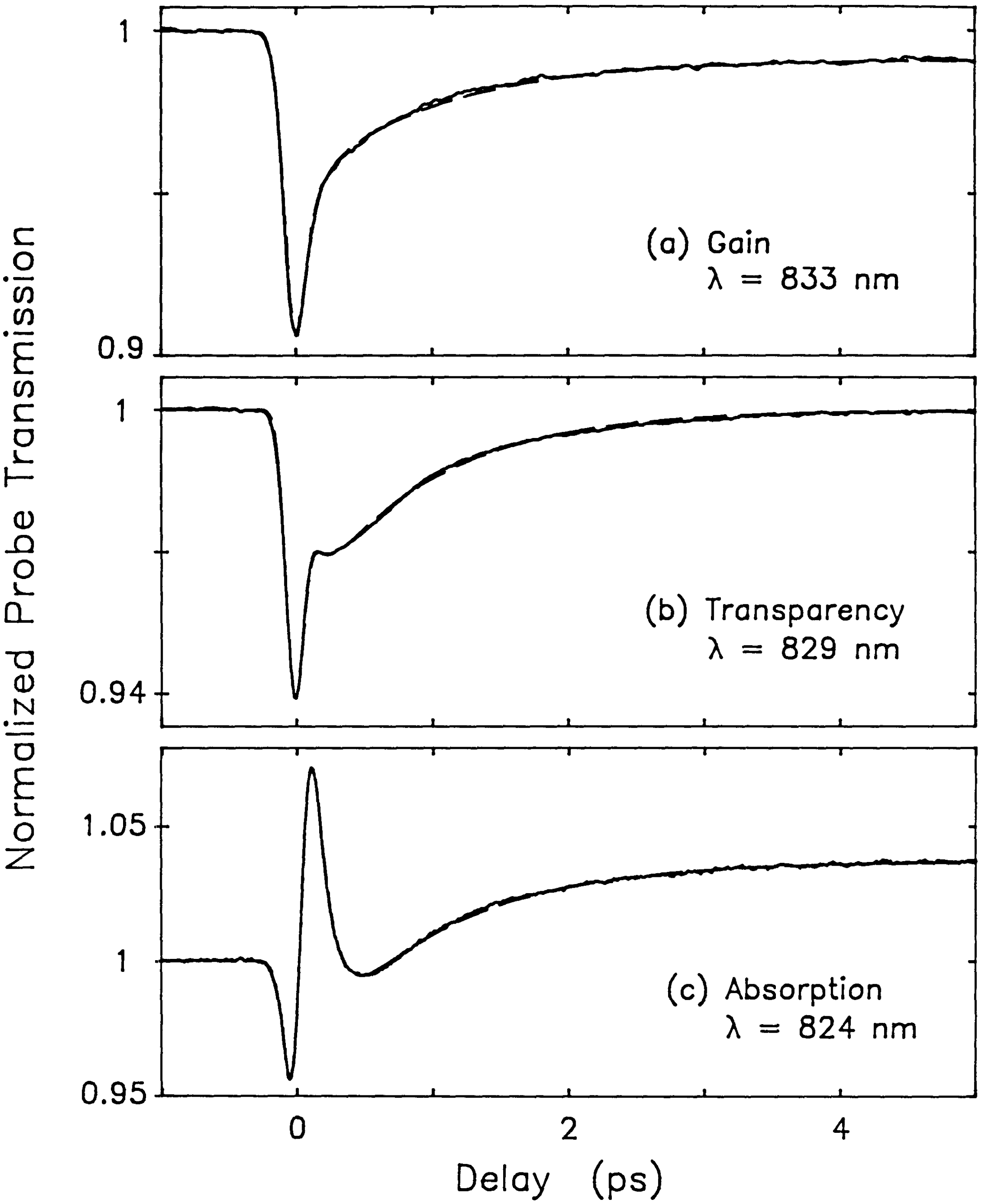

Figure 4.12: Measured above-band gain dynamics from Fig. 4.7 (solid lines) with fits overlaid (dashed lines).

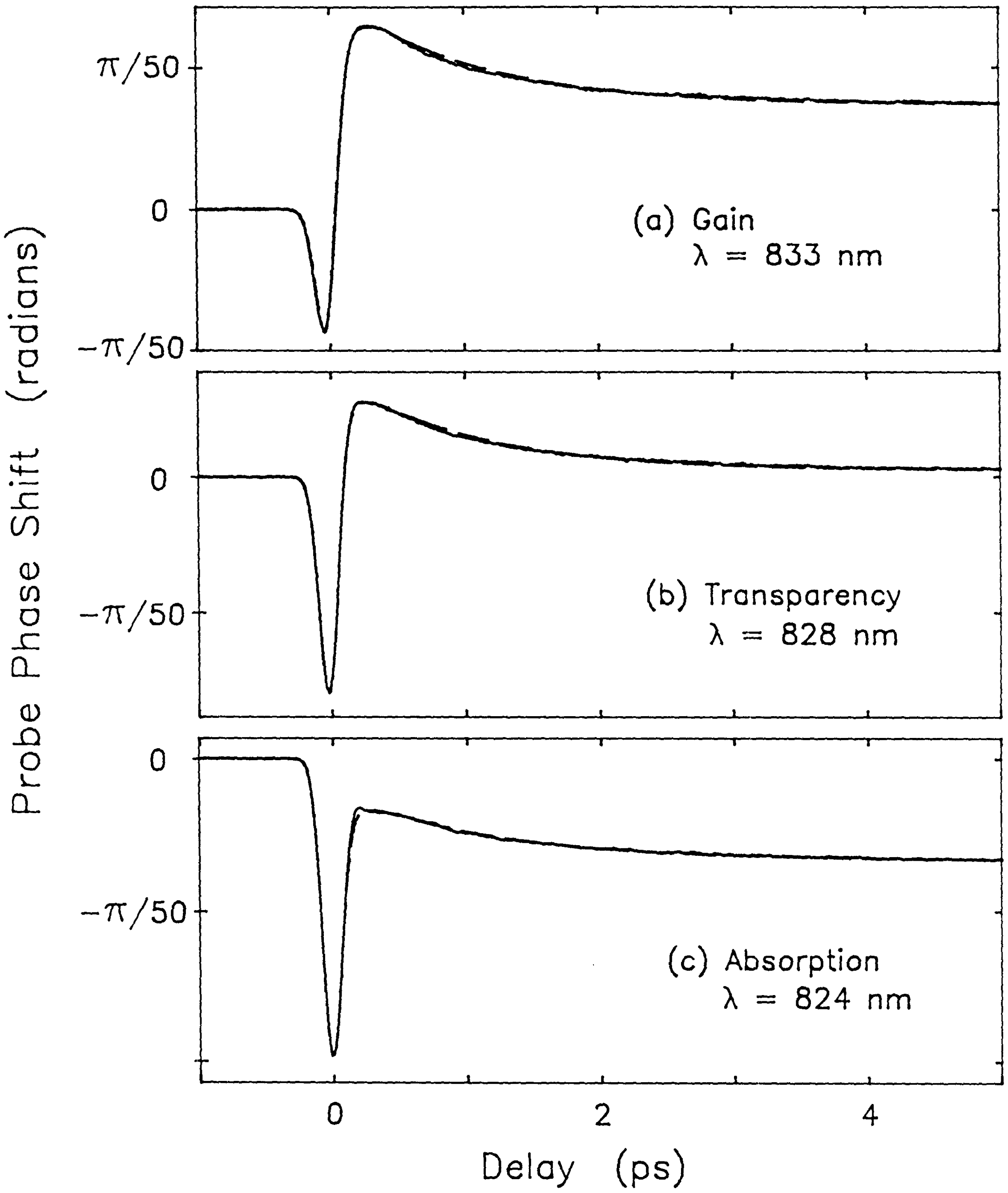

Figure 4.13: Measured above-band index dynamics from Fig. 4.8 (solid lines) with fits overlaid (dashed lines).

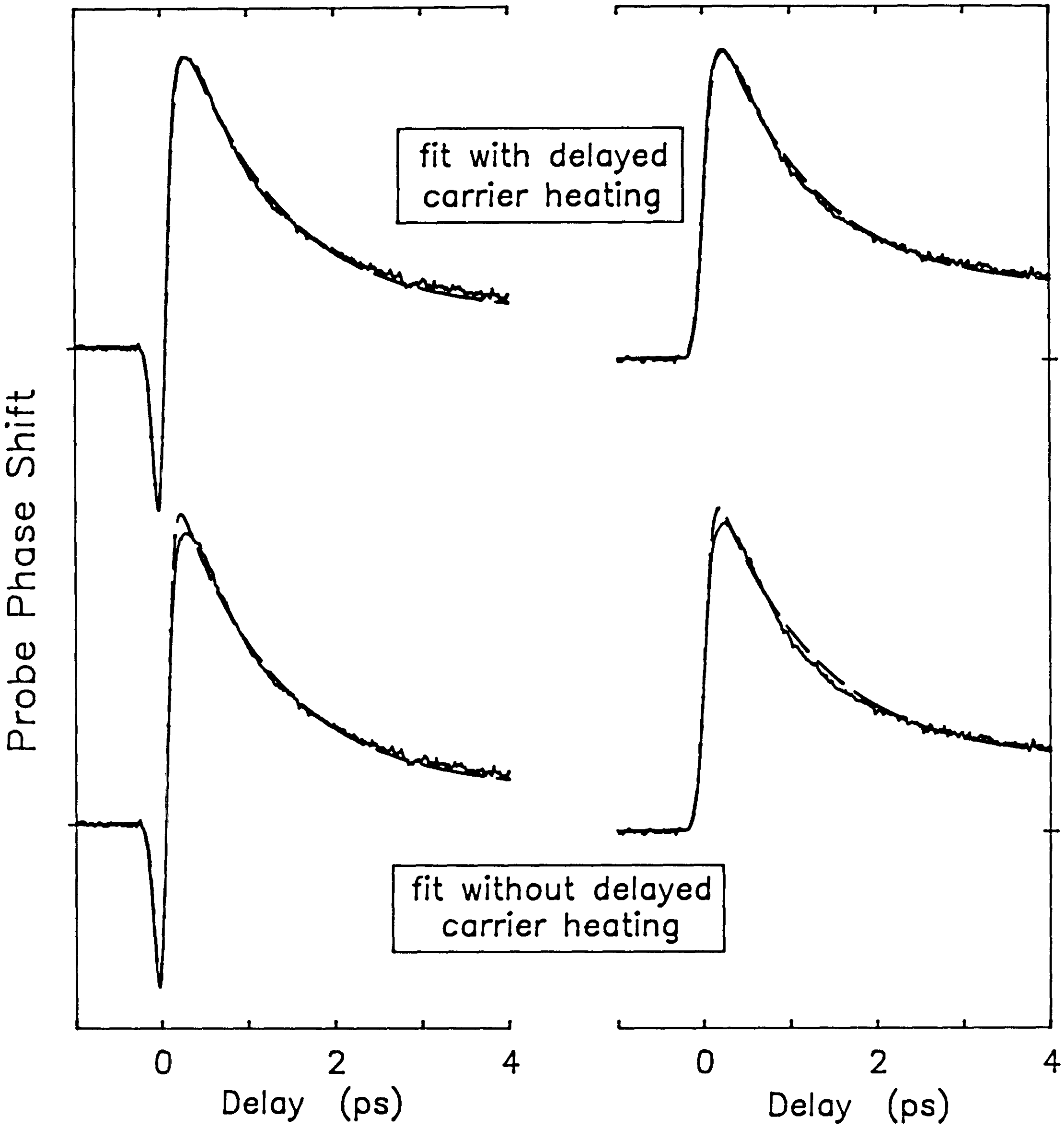

Figure 4.14: Measured below-band index dynamics (solid curves) with fits overlaid (dashed lines). The upper curves were fit using a response function *with* delayed carrier heating; the lower curves were fit *without* the delay. The data was taken at 872 nm with the diode bias current set at 20 mA (left side) and 30 mA (right side).

Chapter 5

The Transparency Point

Transparency is a useful operating point for pump-probe measurements because it allows the study of ultrafast above-band nonlinearities in the absence of stimulated carrier density changes. The transparency point is also potentially useful for high-speed device applications. Semiconductors exhibit large and ultrafast above-band optical nonlinearities which are often accompanied by long-lived effects due to carrier density changes. However, at the transparency point the long-lived effects are eliminated but the ultrafast dynamics remain. Thus, an optical switch, for example, operated at transparency would take advantage of the large optical nonlinearities, and yet it would not suffer from the long recovery times associated with parasitic carrier density changes.

In this chapter we take a detailed look at some interesting aspects of the transparency point. As it turns out, things are not so simple at transparency, especially when measurements are performed with spectrally broad sources. Fig. 5.1 brings this point home. The spectrum of a 100 femtosecond pulse is superimposed on a typical gain curve at the transparency point. From this figure it is readily apparent that the transparency point for a short pulse is really just a superposition of gain and absorption that add up to a net gain of zero. So, transparency is well-defined only for a spectrally narrow source. With this in mind, we proceed to a discussion of how the transparency point is identified in pump-probe measurements, the effect of changing the carrier density on the dynamics at transparency, and the effect of pulse chirp on the dynamics at transparency.

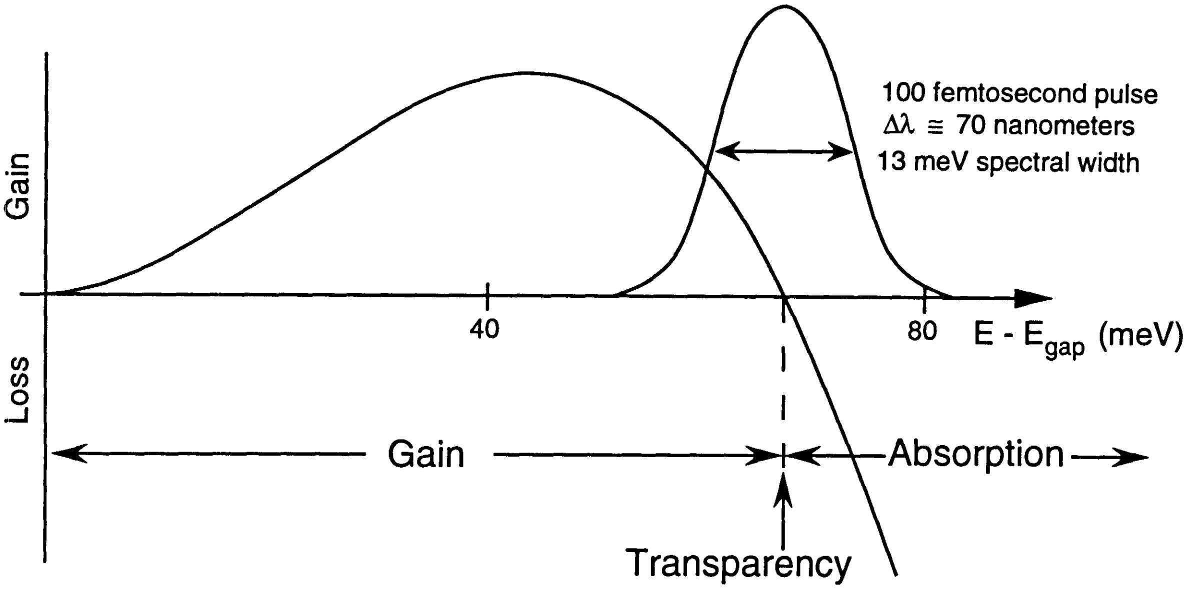

Figure 5.1: Typical AlGaAs gain curve with the spectrum of a 100 femtosecond pulse superimposed on it.

5.1 Locating the transparency point

There are three methods for finding the transparency point, all of which should give equivalent results. However, this is not the case, and in this section we discuss discrepancies between the three methods. Careful pump-probe measurements at and around the transparency point reveal that the gain and refractive index responses do not agree on the location of the transparency point. Fig. 5.2 shows measurements of gain and refractive index dynamics performed at 825 nanometers. With the bias current set at 27.8 mA, the gain response exhibits no long-term offset, indicative of the transparency point. However, the index response shows a substantial positive long-term refractive index change. With the bias current reduced by 1.5 mA, the refractive index settles to zero, but the gain exhibits a long-term positive step, indicating operating in the absorption regime.

Apparently, there is an additional long-lived process that affects either the gain or the absorption. It is likely that the gain response is the true indicator of the transparency point because the probe transmission is a direct measure of the gain. However, the index response can be affected by other phenomena such as changes in

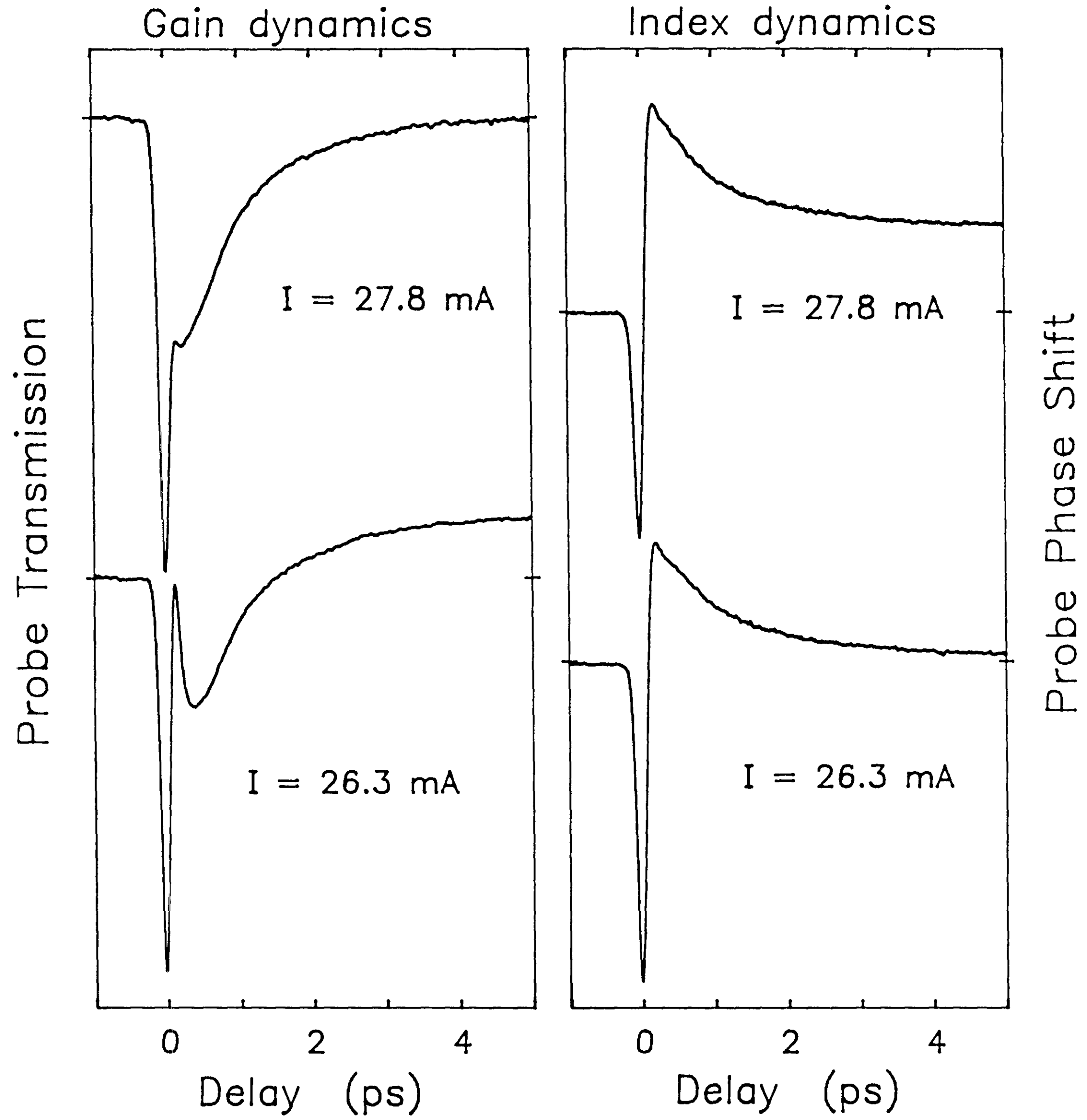

Figure 5.2: Gain and refractive index dynamics measured at 825 nanometers around the transparency point. The gain experiences transparency for 27.8 mA bias current, while the index is at transparency for 26.3 mA bias current.

the lattice temperature. The carriers that are heated through free carrier absorption give off their energy to the lattice. Increasing the lattice temperature does not have a significant effect on the gain but does cause a positive refractive index change. Thus, at transparency, the index has an additional long-lived positive contribution from lattice heating. This is the same positive index change that was observed in the below-band index measurements in the previous chapter.

The third method for finding the transparency point is bias-lead monitoring [94, 95, 96]. Bias-lead monitoring involves measuring the voltage drop across the *p-n* junction of an active waveguide. Monitoring any induced voltage changes caused by light propagating through the device is a potentially useful diagnostic and measurement technique. If light tuned to the gain regime propagates through an active waveguide, carriers are removed from the bands through stimulated recombination. This stimulated carrier density change induces a decrease in the voltage drop across the junction. In the absorption regime, increasing the carrier density causes an increase in the voltage drop. Finally, at the transparency point with no stimulated carrier density changes, there is no induced change in the voltage across the diode.

Thus, the transparency point can be set and maintained by monitoring the bias-lead voltage. This could be of practical use in operating a device which needs to sit at transparency – for example, an all-optical switch may need to be operated at transparency to avoid long-lived carrier density effects. To ensure that the device remains at the transparency point (to compensate for wavelength variation, temperature changes, device aging, etc.), one could electronically monitor the bias-lead voltage and feed this back to the current supply. This idea has merit, but it turns out that thermally induced voltage changes can mask the actual location of the transparency point.

A single beam of short pulses at 825 nanometers was sent through the active waveguide. The induced bias-lead voltages were on the order of 100 μV, and the induced voltage passed through zero at around 23 mA bias current, well below the actual transparency current. Thermal effects are believed to be the source for this discrepancy. The light incident on the diode heats up the device through absorption at the facet and inside the diode (the cladding is absorptive in these devices). Since we only couple about 6% of the incident light into the waveguide, a large amount of energy can be absorbed at the front facet.

Indeed, playing with the input coupling of the beam demonstrates that thermal effects are present. When the light incident on the front facet is slightly decoupled so that no light propagates through the waveguide, an induced voltage change is still observed. And this observed voltage change is insensitive to the current level. So, although light does not travel through the waveguide, it still hits the front facet or is absorbed by the cladding, resulting in heating. Finally, when light is coupled through the waveguide and the current is set at the true transparency point (as determined by the gain response), we observed a negative induced voltage change that does not change when the light is decoupled. And similarly, with below-band light, a negative induced voltage change is observed even though there are no stimulated transitions. The negative voltage change when the junction is heated agrees with the theory of p-n junctions [97]. At a constant bias current, a temperature increase causes the voltage across the diode to decrease.

So it seems that in our AlGaAs devices there is enough heating of the diode to induce a significant voltage change. This behavior was not observed in previous work by Hall *et al.* in InGaAsP waveguides [94]. There, the light was coupled into the waveguide with much higher efficiency ($\sim$ 50%) because a fiber lens was used. Also, the devices used in that work had claddings that were not strongly absorbing. However, in a recent paper by Davies *et al.* [98], a similar discrepancy in finding the transparency point was noted. This behavior was seen in an active InGaAsP directional coupler using fiber lenses for coupling. They attribute the discrepancy in transparency currents to the more complex nature of the coupler structure. Thermal effects are not mentioned, but they may lead to a more plausible explanation – perhaps the cladding or front facet was absorptive in their device.

5.2 Measurements at the transparency point

Next we look at how the gain and refractive index dynamics at transparency behave as we vary the carrier density. Fig. 5.3 shows gain dynamics as the current is increased from 18 mA to 42 mA. The pulses are tuned to shorter wavelengths as the current is increased to maintain operation at the transparency point. The pump power was kept at approximately the same level for all the measurements. The size of the two-photon absorption dynamic changes little as the carrier density is increased. However, the size of the carrier heating feature increases significantly. As the carrier density increases, more and more free carrier absorption occurs, causing a larger heating

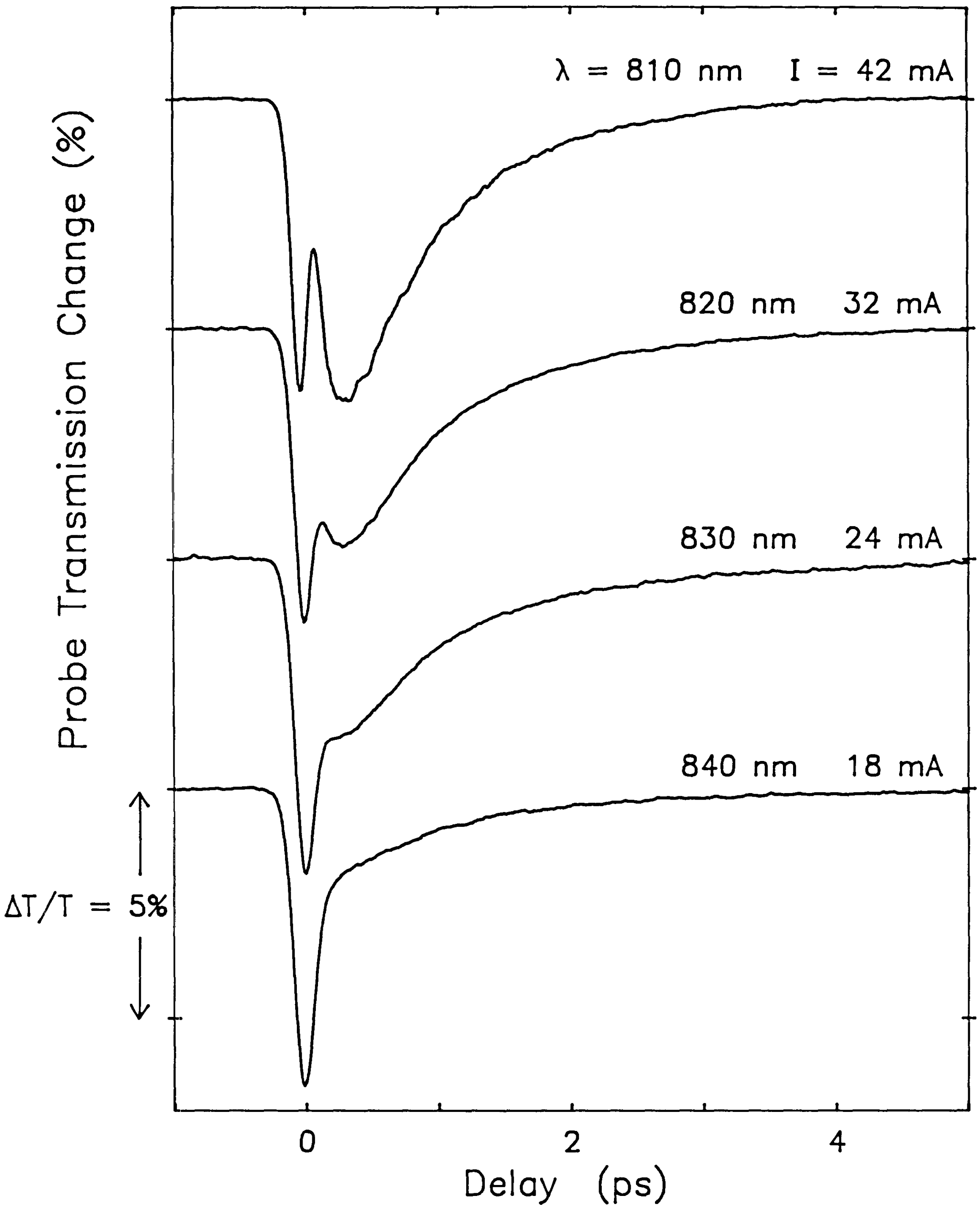

Figure 5.3: Gain dynamics at the transparency point for increasing carrier density.

dynamic. This is the same behavior that was observed in the below-band refractive index measurements as the bias current was increased (see Fig. 4.5 on 83).

Finally, the cusp feature, which was previously attributed to the delay in the onset of carrier heating, becomes more prominent as the carrier density is increased. The data can be fit using the response function Eq. (4.1), but the fits require adding some spectral hole burning component at the higher carrier densities or changing the time constant of the carrier heating delay. Neither of these fits is appealing on physical grounds. A likely explanation for the cusp comes from a recent paper by Mørk and Mecozzi [99] in which they analyze pump-probe measurements and take into account the slope of the gain curve. As their analysis describes, in addition to the gain dynamics, the probe pulse experiences a time-dependent phase $\phi(t)$. This leads to a frequency shift of the probe through: $\Delta\omega = -d\phi(t)/dt$. The dominant contribution to $\phi(t)$ at transparency is a phase that increases with time (positive slope). This causes a red-shifting of the probe wavelength, pushing it slightly into the gain regime. Thus, the probe experiences a transient increase in transmission. This would explain the cusp in the measured gain dynamics. And finally, as the carrier density increases, the slope of the gain curve at the transparency point increases. Notice in Fig. 2.10 (page 45) how the gain curve gets steeper at the transparency point with increasing carrier density. Thus, the size of the cusp at the transparency point should increase with carrier density, which is just what is seen in Fig. 5.3.

Thus, the cusp observed in the gain dynamics can be explained by some mixing-in of the phase dynamics. This does not mean that there is not a delay in carrier heating. It just means that the above-band gain dynamics measured at the transparency point are not helpful in proving or disproving the existence of a carrier heating delay.

To complete the picture, Fig. 5.4 shows the refractive index dynamics at the transparency point as the carrier density is increased. The data from Figs. 5.3 and 5.4 were obtained from different diode amplifiers, and so the locations of the transparency points between figures do not correspond. The refractive index exhibits an increase in both the instantaneous dynamic and the carrier heating dynamic as the carrier density is increased. The instantaneous dynamic increases because the pulses are being tuned to higher energies where there is a greater density of unoccupied states. The optical Stark effect that gives rise to this dynamic gets stronger as we tune closer to absorbing states. And the increase in the size of the carrier heating response agrees with the behavior of the gain dynamics as well as the below-band index dynamics.

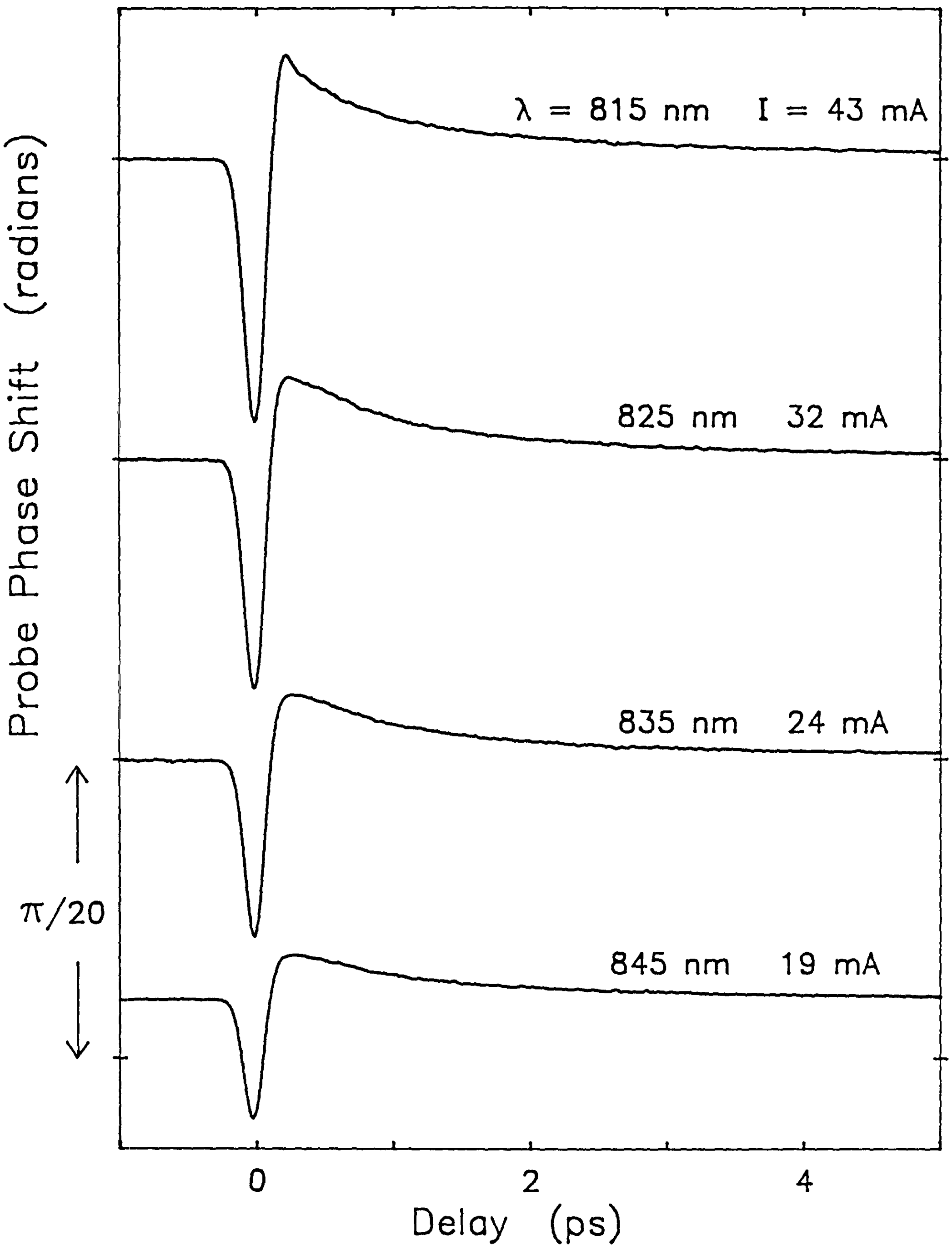

Figure 5.4: Refractive index dynamics at the transparency point for increasing carrier density.

5.3 Pulse chirp and transparency

In this section we briefly explore the effect of pulse chirp on the dynamics at the transparency point. Fig. 5.5 shows the gain and refractive dynamics at transparency for chirped and unchirped pulses. The chirped pulses were obtained by broadening with a prism pair from about 100 fs to 150 fs. The gain and index dynamics were performed at slightly different bias currents so the unchirped pulses exhibit transparency behavior. Notice how the long-lived response depends on the pulse chirp. Negatively chirped pulses (blue wavelengths in front, red wavelengths in back) behave as if they are slightly in the gain regime – the probe gain recovers to a lower value, and the index recovers to a higher value. The front part of the pump pulse is absorbed and puts up carriers, so the trailing part sees a slightly higher gain. The net effect of this is to decrease the carrier density, and so the probe pulse experiences a reduction in gain. The opposite occurs for positively chirped pulses where the pump undergoes net absorption. Thus, the chirp on a pulse can affect the location of the transparency point as indicated by the long-lived gain or index behavior.

The ultrafast refractive index dynamics are fairly insensitive to the pulse chirp. The positively chirped pulses give a broadened response because they continue to broaden while traveling through the waveguide due to the positive waveguide dispersion. The ultrafast gain dynamics, on the other hand, exhibit significant effects related to the pulse chirp. This behavior is not well understood, but it is likely due to an artifact caused by pulse chirp, similar to the index artifact that was detailed in Chapter 3. In this case, the chirp on the pulses could cause the refractive index dynamics to be mixed in with the measured gain dynamics.

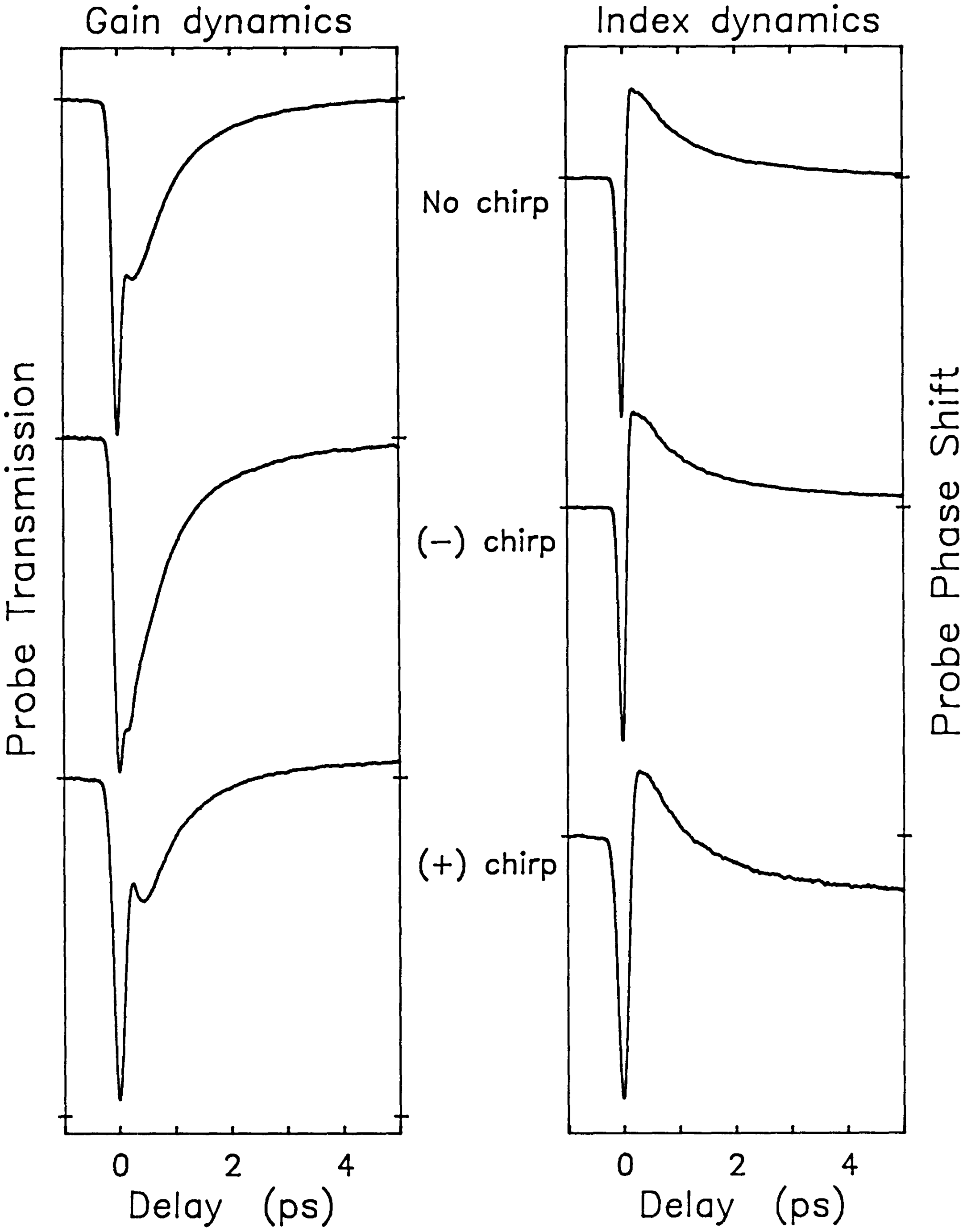

Figure 5.5: Gain and refractive index dynamics at the transparency point measured with chirped pulses.

Chapter 6

Additional Measurements

This chapter presents an assortment of measurements that add some depth to what we have learned in the previous two chapters. The effect of increasing the pump power is discussed. Then, we show evidence for cooling of the carriers through stimulated absorption. And lastly, gain measurements performed with a spectrometer placed after the diode laser amplifier reveal some interesting dynamics.

6.1 Power-dependent measurements

In the perturbational limit, the signal measured in a pump-probe experiment is linear in the pump power. That is, doubling the pump power doubles the signal size without introducing any distortions. As the pump power is increased beyond the perturbational limit, we enter a new regime of high intensity measurements, and new behavior can appear. The small-signal regime is a useful method for determining the impulse response function $h(t)$ and for identifying the ultrafast processes that are occurring. Having characterized the perturbational response in the previous two chapters, here we explore what happens as the pump power is increased.

Fig. 6.1 shows above-band gain dynamics measured at transparency as the pump power is increased. The signal does not scale up linearly with pump power. Rather, the carrier heating dynamic increases faster than the two-photon absorption dynamic. The two-photon absorption signal that is measured is the result of one pump photon and one probe photon being absorbed. So, clearly the instantaneous two-photon absorption dynamic that we measure in a pump-probe experiment scales linearly with the pump power. At the transparency point carrier heating can be caused by free carrier absorption and two-photon absorption. Heating through free carrier absorption of pump photons scales approximately linearly with pump power. However, two-photon

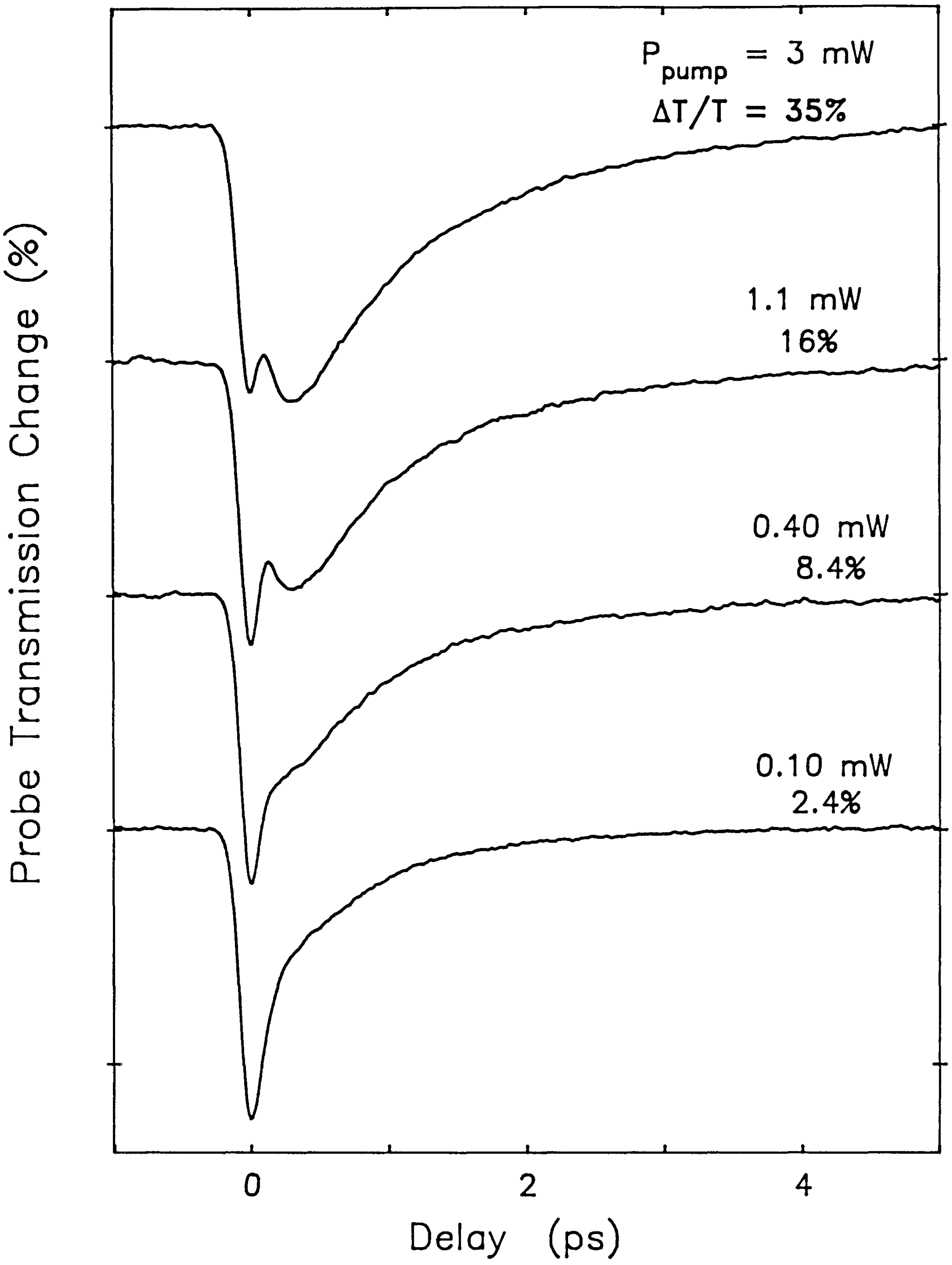

Figure 6.1: Above-band gain dynamics at transparency for increasing pump power. The pump power before the diode laser amplifier and the magnitude of the maximum probe transmission change are shown above each trace. The bias current was set at 29 mA, and the measurements were performed at 826 nm.

absorption of pump photons scales as $I^2_{\rm pump}$. Therefore, at high pump powers carrier heating caused by two-photon absorption of the pump will dominate the pump-probe signal. This explains why the carrier heating signal grows faster than the two-photon absorption signal as we go to higher pump powers. Similar results have recently been observed in pump-probe measurements on InGaAsP amplifiers at 1.5 μm [100]. It is also seen that the data in Fig. 6.1 can be fit by our original $h(t)$ (Eq. (4.1)), but the time constant that governs the carrier cooling process increases from 1 ps to about 1.3 ps at 3 mW pump power.

Figs. 6.2 and 6.3 show some below-band measurements of gain and refractive index dynamics versus pump power. As in the above-band case, the carrier heating dynamic begins to dominate the measured response as the pump power is increased. Fig. 6.3 demonstrates this dramatically – the 9 mW pump induces a large index change caused by carrier heating. Again, the $I^2_{\rm pump}$ dependence of two-photon absorption of the pump is responsible for this. The long-lived negative gain and index changes are caused by carriers put up through two-photon absorption of the pump pulse as well. As above, fitting this data shows that the carrier cooling time constant increases with pump power. Around 0.6 mW pump power the recovery time constant is 1.1 ps, and around 3 mW pump power the recovery time constant is 1.5 ps. And the below-band index response at 9 mW pump power shown in Fig. 6.3 has a carrier cooling time constant of about 2.4 ps. Thus, the time for carriers to cool increases significantly with increasing pump power. This suggests that there is some sort of bottleneck in the carrier cooling process. Similar increases in carrier cooling times have been reported in other work (Ref. [101] and references therein). Explanations for this effect include reabsorption of phonons by the carriers and carrier-carrier screening that reduces the coupling between carriers and phonons [101].

6.2 Stimulated cooling

Carrier temperature changes can be caused by three processes: two-photon absorption, free carrier absorption, and stimulated transitions. Two-photon absorption and free carrier absorption can only induce carrier heating. Stimulated transitions, on the other hand, can cause carrier heating *and* cooling, depending on the carrier density and the excitation wavelength. For example, if the pump pulse puts up carriers with energies less than the average energy of the carriers, this will result in a cooled distri-

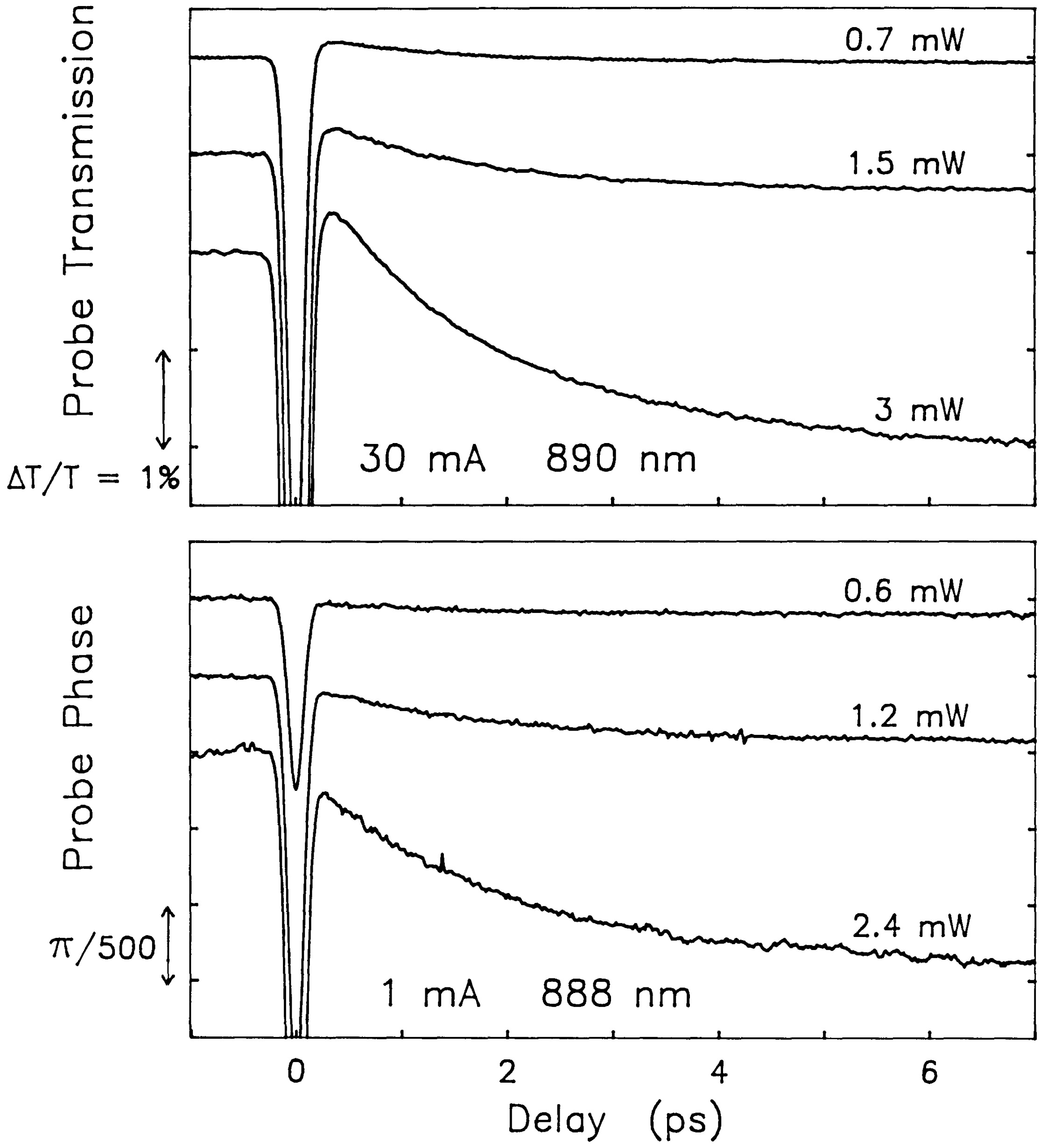

Figure 6.2: Below-band gain and refractive index dynamics as a function of pump power (measured just before the diode laser amplifier). The data is blown-up to show the behavior of the carrier heating response. Note that the gain and refractive index measurements are performed under different operating conditions as indicated.

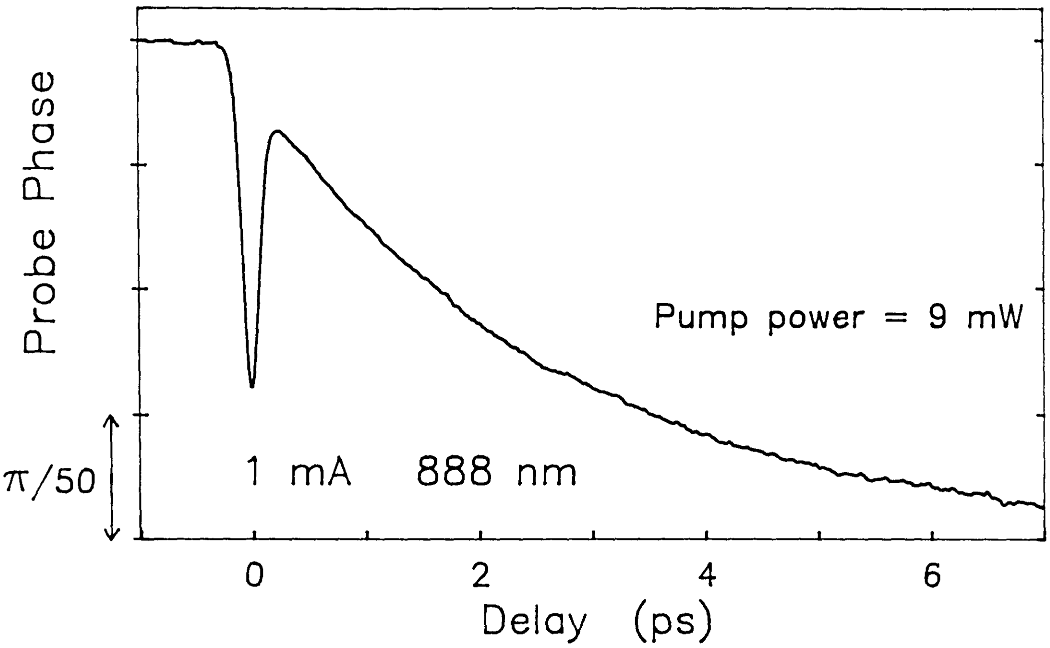

Figure 6.3: Below-band refractive index dynamics with 9 mW of pump power.

bution. Alternately, if the pump pulse removes carriers from the band with energies greater than the average energy, the distribution will also be cooled. Stimulated heating can occur as well, but it is difficult to distinguish experimentally from heating through other mechanisms.

Fig. 2.14 on page 48 illustrates the various regimes where stimulated heating and cooling can occur in AlGaAs. For example, as indicated in the figure, at 2.5×10^{18} cm^{-3} carrier density, stimulated cooling occurs for the pump tuned between 60 and 100 meV above the band gap energy. In this regime, the pump will be partially absorbed, and the carriers that are generated have energies less than the average energy of the distribution. Stimulated cooling in the gain regime only occurs after the two curves in Fig. 2.14 have crossed. This occurs above 5×10^{18} cm^{-3} carrier density. This is a rather high carrier density, and the spectral window where stimulated cooling occurs is narrow. So, the most promising approach for observing stimulated carrier temperature changes in a pump-probe experiment is to look for cooling in the absorption regime.

To demonstrate carrier cooling through stimulated transitions, measurements were performed in the strongly absorbing regime – at short wavelengths and low currents. Fig. 6.4 shows above-band gain and refractive index dynamics measured at 30 mA and

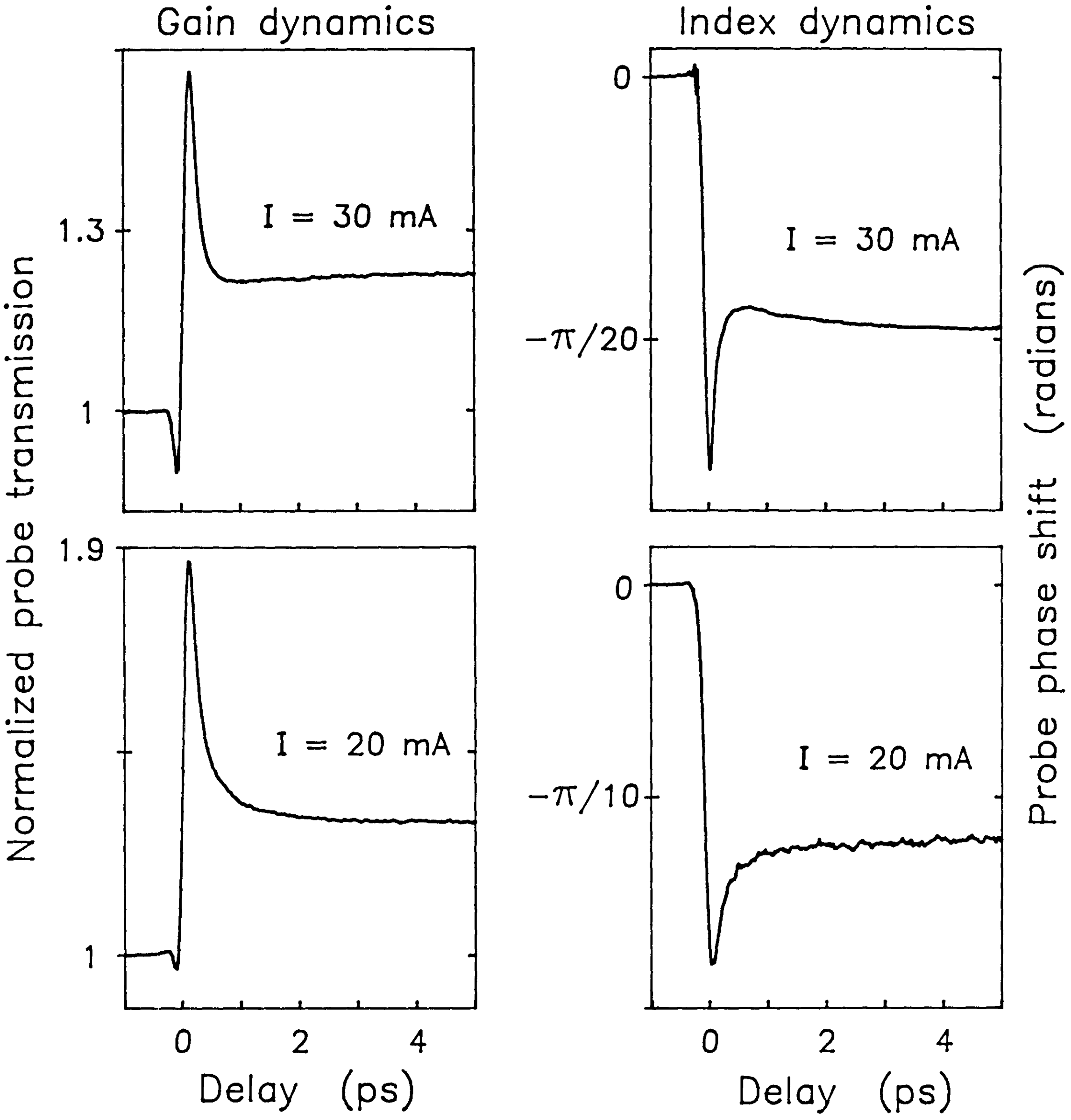

Figure 6.4: Stimulated carrier cooling: above-band gain and refractive index dynamics measured at 820 nm. At 30 mA bias current, a small carrier heating signal is seen. At 20 mA bias current, evidence for stimulated carrier cooling appears as the carrier temperature signal flips sign.

20 mA bias current. At 30 mA, the standard absorption behavior is seen – a small dip in the gain after the spectral hole burning feature indicates carrier heating. The index dynamics at 30 mA exhibit a small positive index change that also indicates carrier heating. Then, with the bias current lowered to 20 mA, the carrier temperature dynamic flips sign, indicating a transition from heating to cooling. Similar results have been obtained in pump-probe measurements of InGaAs amplifiers [20, 102, 100].

The carrier heating and cooling behavior is supported by fitting the data – all the carrier temperature signals can be fit with a $\sim$ 1.2 ps time constant, indicative of a carrier temperature recovery process. In addition, both the carrier cooling and heating dynamics are fit well with a delay term. Thus, it appears that stimulated cooling contains a delay in its turn-on just like the delay exhibited by carrier heating through free carrier absorption. However, this fitting procedure is not definitive due to the small size of the carrier temperature dynamics, and thus, the results are suggestive but not conclusive.

6.3 Gain measurements with a spectrometer

The last topic in this chapter concerns the addition of a spectrometer to the pump-probe setup. Measurements of gain dynamics are performed in the usual fashion (see Fig. 3.1 on page 57). However, after the pump has been filtered out with the polarizer and before the probe hits the detector, the probe beam is passed through a spectrometer. The spectrometer selects a narrow portion of the probe spectrum, and then the probe is sent to the detector. The measured gain dynamics from this experiment are shown in Fig. 6.5. The top curve is the regular pump-probe gain response at the transparency point with the pump-probe wavelength centered at 828 nm. The lower curves are pump-probe gain measurements with the spectrometer tuned to the wavelength indicated. The spectrometer was set to have about a 1 to 2 nm bandwidth so that it selects out a fraction of the probe pulse spectrum (the FWHM of the pulse spectrum is typically 9 nm). Notice that the data obtained with the spectrometer tuned to 829 nm – close to the center wavelength of the pulses – is fairly similar to the regular gain response at the top of the figure. However, the other curves display a variety of unusual dynamics which have not been seen before.

Somehow, the filtering action of the spectrometer introduces new dynamics into the pump-probe signal. The explanation for this lies in the refractive index dynamics,

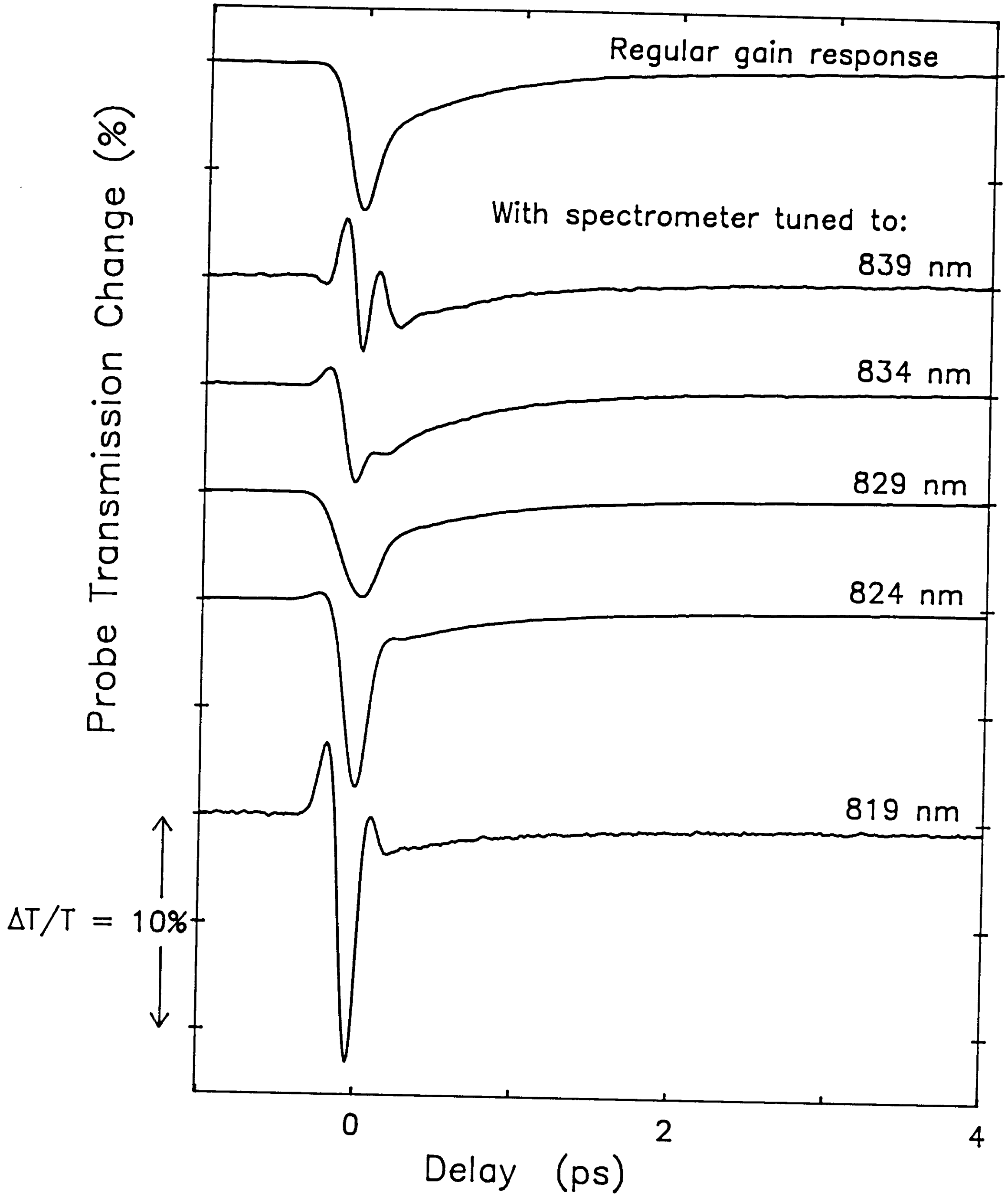

Figure 6.5: Above-band gain dynamics measured with a spectrometer after the diode laser amplifier. The probe pulses coupled out of the diode laser amplifier are sent through a spectrometer and then detected. The top curve is the usual pump-probe signal measured at 828 nanometers with the bias current at 33 mA. The lower five curves show the pump-probe gain signal measured with the spectrometer tuned to the wavelength indicated.

which are normally not present in a gain measurement. Index dynamics are non-dissipative – they affect the probe phase but not the probe amplitude. Thus, index dynamics do not show up in gain measurements because the gain measurements monitor the probe power. However, a spectral filter can cause index dynamics to get mixed into the gain signal. The phase shift that is imparted to the probe affects the probe spectrum. That is, the time-dependent probe phase shift does not affect the total probe power, but it can dynamically redistribute power within the probe spectrum. Normally, throwing around power in wavelength does not matter since the gain measurements look at the total probe power. However, with a spectral filter present the gain measurements become sensitive to changes in the probe spectrum. Thus, the spectrometer leads to the mixing in of refractive index dynamics.

To quantify the effects of a spectral filter, a simulation was performed. Using the formalism outlined in Chapter 3, the pump-probe signal was computed with a spectral filter inserted just before the detector. The response function includes the refractive and absorptive parts: $h'(t) + ih(t)$. The dynamics included in the gain and refractive index response functions are two-photon absorption, the optical Stark effect, and carrier heating with a delay. Convolving this complex response function with the pump pulse intensity profile $I(t)$ gives the time varying absorption change $\Delta\alpha$ and refractive index change Δn seen by the probe pulse. For a specific pump-probe delay τ, the effect on the probe pulse is found by multiplying the delayed probe electric field $E(t-\tau)$ by the pump-induced gain and refractive index changes:

$$\text{Probe after the diode} \;=\; E(t-\tau)\left[1 + i\left(\frac{2\pi L}{\lambda}\right)\Delta n(t) - L\Delta\alpha(t)\right]. \tag{6.1}$$

The probe electric field is then spectrally filtered by performing a Fourier transform, multiplying by a spectral filter function, and Fourier transforming back to the time domain. Finally, the detected signal is formed by taking the magnitude-squared of the spectrally filtered probe electric field and integrating over time. This entire procedure is repeated as a function of pump-probe delay τ. The signals that result from this operation are shown in Fig. 6.6.

The theoretical gain dynamics shown in Fig. 6.6 agree very well with the measured gain dynamics shown in Fig. 6.5. With the spectral filter set at the center wavelength, the gain dynamics are nearly the same as the regular dynamics measured without any filter. As the filter is tuned away from the center wavelength, fast oscillations

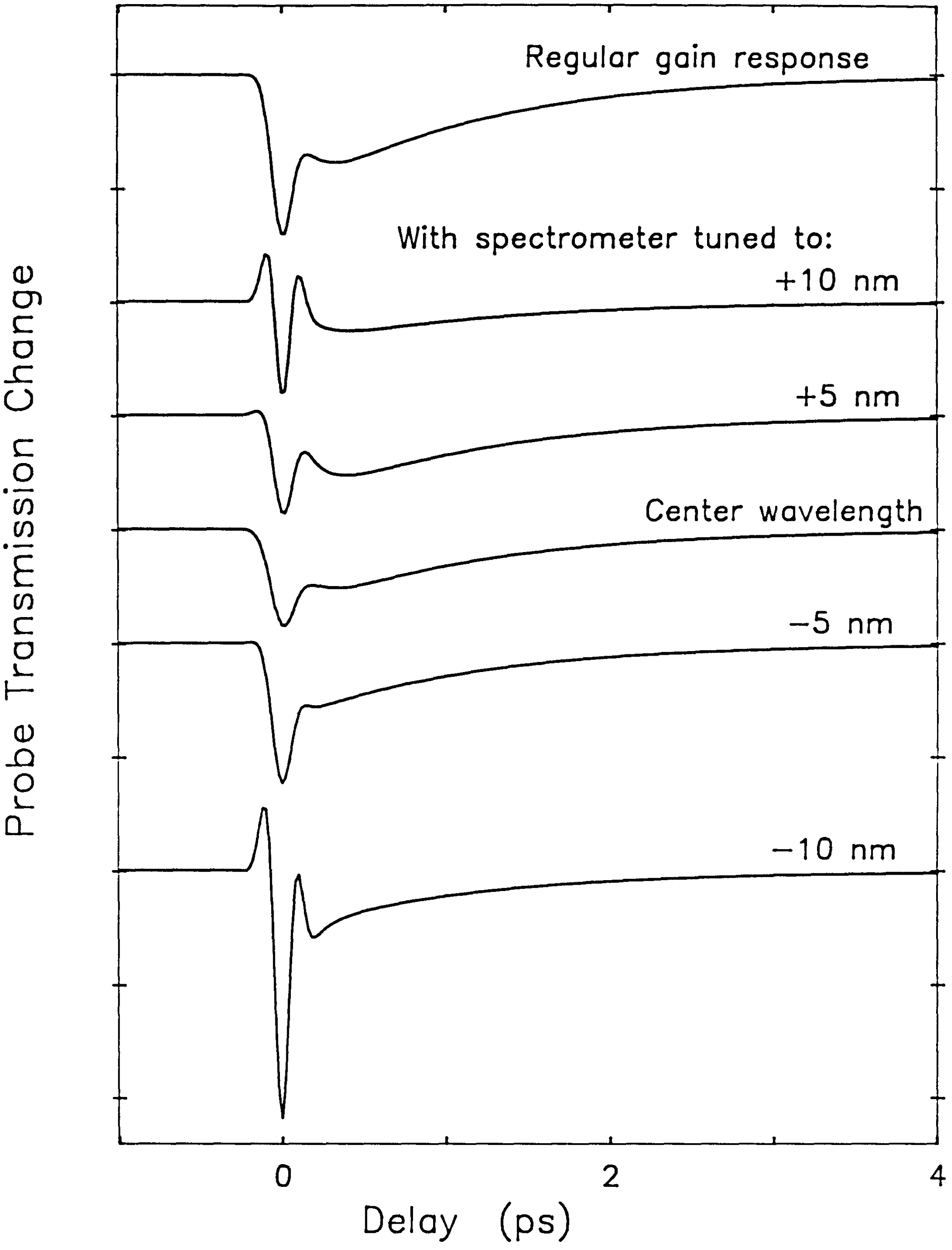

Figure 6.6: Theoretical signal for pump-probe measurement of gain dynamics with a spectrometer (compare with Fig. 6.5). The top curve is the usual pump-probe signal. The lower five curves show the pump-probe signal with a spectral filter set as indicated relative to the pulse center wavelength.

appear around zero delay. The general behavior of these oscillations agrees very well with the measured dynamics from Fig. 6.5. Thus, the presence of a spectral filter in a pump-probe gain measurement causes mixing in of the refractive index dynamics. One lesson learned from this exercise is that it is important to watch out for any wavelength selective elements in a pump-probe setup because they can lead to unwanted signals in the measured gain dynamics. Another observation is that it may be possible to deduce both the gain and refractive index responses from this sort of spectrally resolved pump-probe transmission measurement. Such a measurement technique would eliminate the need for a separate phase measurement to determine the refractive index dynamics.

Chapter 7

Discussion

In the previous three chapters, we described several experimental studies of ultrafast gain and refractive index dynamics in an AlGaAs diode laser amplifier. The purpose of this work is to gain a better understanding of ultrafast optical nonlinearities in AlGaAs. The approach that was employed entailed turning all the knobs available to us and and noting the various results. These knobs included variation of the carrier density, variation of the pump-probe wavelength, variation of the pump power, and variation of the pulse chirp. The effects of these changes were studied with below- and above-band pump-probe measurements of gain and refractive index dynamics. The aim of this chapter is to summarize the main results of these experiments. The important ultrafast processes and the gain and refractive index dynamics that they give rise to are reviewed. Then, the measured refractive index dynamics are distilled into a series of graphs of n_2, the nonlinear refractive index coefficient. Finally, for comparison we review the results of other related experimental investigations involving pump-probe techniques and four-wave mixing.

7.1 Summary of results

Pump-probe measurements on an active AlGaAs waveguide reveal a variety of ultrafast gain and refractive index dynamics. The dominant physical processes that are the source of these ultrafast dynamics include free carrier absorption, two-photon absorption, stimulated transitions, and the optical Stark effect. The data fitting procedure detailed in Chapter 4 helps to quantify the measured dynamics and allows comparison with data taken under various conditions. A summary of the ultrafast gain and refractive dynamics and what was learned about them follows.

When free electrons and holes absorb pump photons, these hot carriers scatter with the carriers at the bottom of the bands, resulting in a heated distribution. The carrier heating caused by this free carrier absorption process results in a transient gain decrease across the gain spectrum. This gain compression recovers with a ~ 1.1 picosecond time constant as the carriers cool back to equilibrium. Accompanying the gain response is a positive refractive index dynamic that also recovers with the same time constant. Carrier density dependent measurements show that the carrier heating signal increases with increasing carrier density. This is consistent with the free carrier absorption process which also increases linearly with carrier density. An interesting aspect of the carrier heating process is a delay in the turn-on of the carrier heating dynamic. The fits to the below-band refractive index data are qualitatively better when a 120 fs carrier heating delay is included. This suggests that it takes a finite amount of time for the hot carriers to scatter with and heat up the distribution of carriers that sits at the bottom of the bands.

Two-photon absorption causes an instantaneous reduction in gain at above- and below-band wavelengths. In addition, two-photon absorption causes an increase in carrier density. The energetic carriers generated through two-photon absorption can also induce carrier heating in the same way as free carrier absorption. At high pump powers, the two-photon absorption effects dominate the measured pump-probe signal because of the I^2 dependence of two-photon absorption.

With above-band photons, stimulated emission and absorption cause carrier density changes, spectral hole burning, and heating and cooling of the carriers. Above-band measurements in the absorption regime show evidence for spectral hole burning. In the gain regime, spectral hole burning is less apparent, but fits to the data support its presence. Stimulated cooling was also observed far in the absorption regime.

An instantaneous refractive index dynamic was observed in above- and below-band measurements. The negative sign of the dynamic and its variation with wavelength and carrier density suggest it is caused by the optical Stark effect. Still, there may be some contribution from two-photon absorption as well. Theoretical investigations of instantaneous refractive index nonlinearities in semiconductors have been performed elsewhere [91, 92, 93]. Our measurements agree very well with the results of these theories. One discrepancy is that a positive refractive index change is predicted at high carrier densities. This was not observed here, but the carrier density may not have been high enough for the index change to flip sign. Another prediction is that of a delay in the response of the optical Stark effect. This is caused by the time it takes for carriers to reach an equilibrium after the levels have been shifted in energy by the optical Stark effect. It is possible that the pulses used here are too long to observe this effect.

The transparency point is an interesting and potentially useful operating point for above-band measurements. It was found that in the AlGaAs devices studied here, the refractive index exhibited a long-lived dynamic at the transparency point. This is attributed to a thermally induced refractive index change that has little effect on the long-lived gain dynamics.

Finally, experiments performed with chirped pulses revealed an artifact in the measured refractive index dynamics. This dynamic occurs when the pulses are chirped and when the probe and reference pulses are not perfectly overlapped after the TDI. A theoretical analysis showed that the artifact is caused by gain dynamics mixing in with the refractive index measurements.

7.2 Measurements of n_2

A useful way to characterize the refractive index dynamics is with the nonlinear refractive index coefficient n_2. The method for pulling out values for n_2 from the measured refractive index dynamics was detailed in Section 2.2.3. Briefly, the measured probe phase shift $\Delta\phi$ can be related to the pump-induced refractive index change Δn through $\Delta\phi/2\pi = \Delta n L/\lambda$. This gives the pump-induced modal refractive index change. One key issue is whether to calculate $n_{2_{\mathrm{modal}}}$ or $n_{2_{\mathrm{material}}}$. The modal n_2 is important if, given our particular structure, we want to know what sort of phase shift can be realized. However, for comparing our results to measurements in other devices or other materials, knowing the material n_2 is more useful. To convert the modal refractive index change into the underlying refractive change in the active region, we use the results plotted in Fig. 2.7 on page 37. Then, n_2 is found from $\Delta n = n_2 I_{\mathrm{eff}}$, where I_{eff} is the effective intensity of the pump *in the active region.* Notice that the nonlinear refractive index coefficient that is measured here is actually $n_{2\perp}$ to indicate that the pump and probe pulses are cross polarized. If the pump and probe were co-polarized, we would expect a larger value for n_2 [31].

For the instantaneous index dynamic, the size of the pump-induced index change is proportional to the pump intensity, and so, n_2 has units cm^2/W. Here, we will also calculate values of the nonlinear refractive index coefficient for the non-instantaneous processes, carrier heating and the long-lived index response. This is not strictly valid since by definition n_2 assumes an instantaneous Kerr-type response. Still, for simplicity we will refer to the carrier heating and long-lived nonlinear index coefficients as n_2, keeping in mind that these are not instantaneous processes. For the carrier heating dynamic and the long-lived response, the size of the pump-induced index change is proportional to the *fluence* of the pump (in units joules/cm^2). That is, since the recovery times of these processes are longer than the pulse duration, n_2 depends on the time integrated pulse intensity. Thus, for these processes n_2 has units cm^2/J.

Fig. 7.1 shows the computed values for the material n_2 as a function of bias current. These measurements were performed below the band edge at 888 nm. At low bias currents the instantaneous n_2 reaches a maximum value of about -0.85×10^{-12} cm^2/W. The instantaneous n_2 falls off quickly as the bias current is increased. The optical Stark effect is a resonant process, and increasing the carrier density is effectively like pushing the band edge away from the probe wavelength. Thus, the instantaneous n_2 exhibits a resonant-like decrease for increasing carrier density. The n_2 for carrier heating increases in a fairly linear fashion as the bias current is increased. This makes sense because free carrier absorption increases linearly with carrier density. Finally, the long-lived n_2 is attributed to a combination of carrier density changes and lattice heating. Two-photon absorption of the pump increases the carrier density, which causes a negative n_2. This negative index change is gradually overtaken by lattice heating caused by the heated carriers giving off energy to the lattice. So, at high carrier densities the long-lived n_2 becomes positive.

Next, we look at how the nonlinear index coefficient varies with wavelength. Fig. 7.2 shows the material n_2 for the instantaneous and carrier heating dynamics. Below the band edge, the n_2 is shown at several different bias currents. And above-band, the n_2 at the transparency point is shown – as we tune to shorter wavelengths, the bias current is increased to maintain operation at transparency. At transparency, both the instantaneous and carrier heating n_2 increase as the bias current increases. In the case of the instantaneous index dynamic, tuning to shorter wavelengths pushes the probe closer to a large absorptive density of states – this is associated with a larger n_2. Below the band edge, the instantaneous and carrier heating n_2 both increase as the wavelength is tuned toward the band edge. Again, increasing the bias current decreases the instantaneous n_2 and increases the carrier heating n_2.

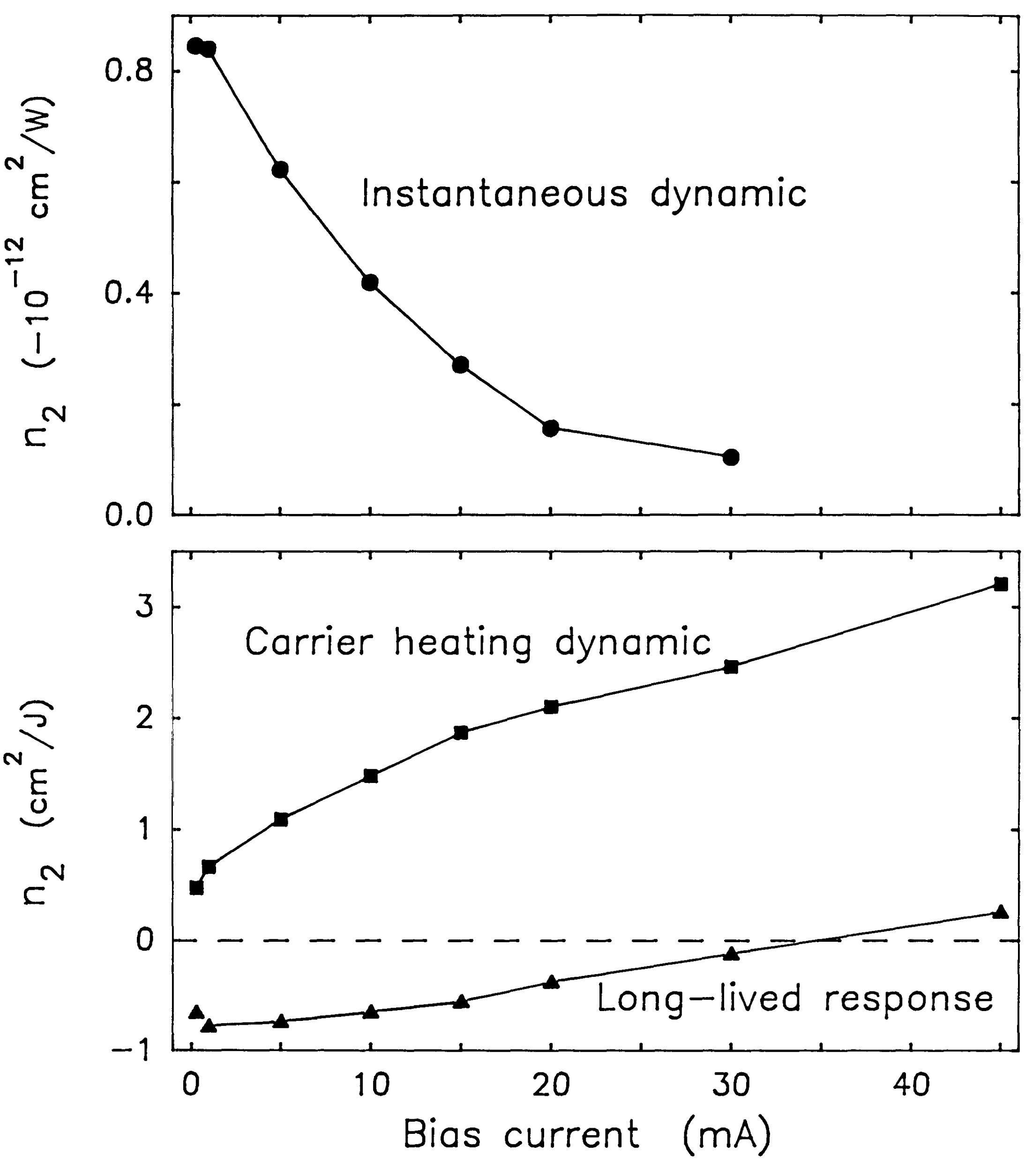

Figure 7.1: Below-band nonlinear refractive index coefficients n_2 measured versus bias current at 888 nm for the instantaneous dynamic, the carrier heating dynamic, and the long-lived response.

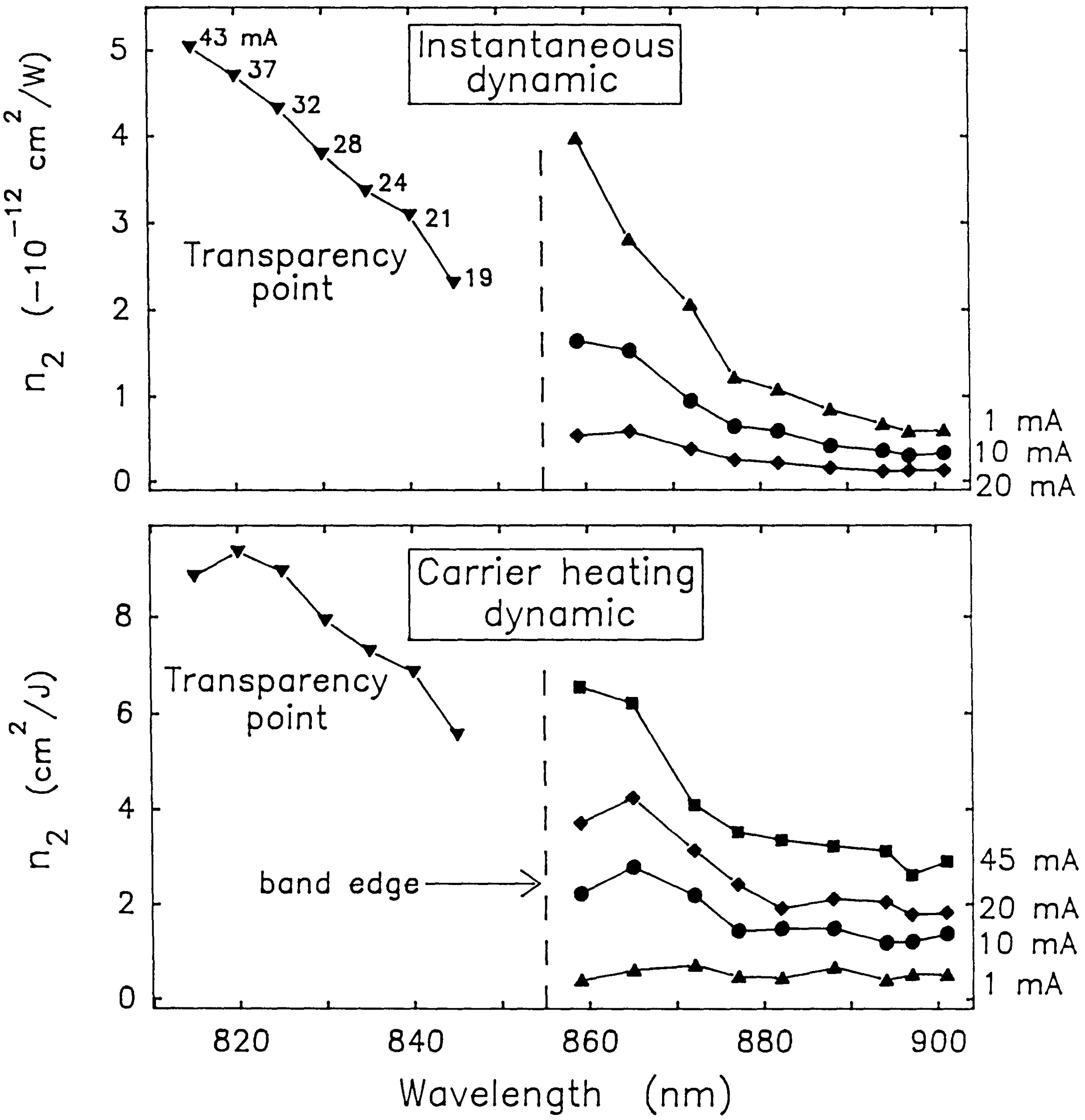

Figure 7.2: Nonlinear refractive index coefficients n_2 measured versus wavelength at several bias currents for the instantaneous dynamic and the carrier heating dynamic. The above-band measurements were performed at the transparency point, and the bias current is indicated beside each data point.

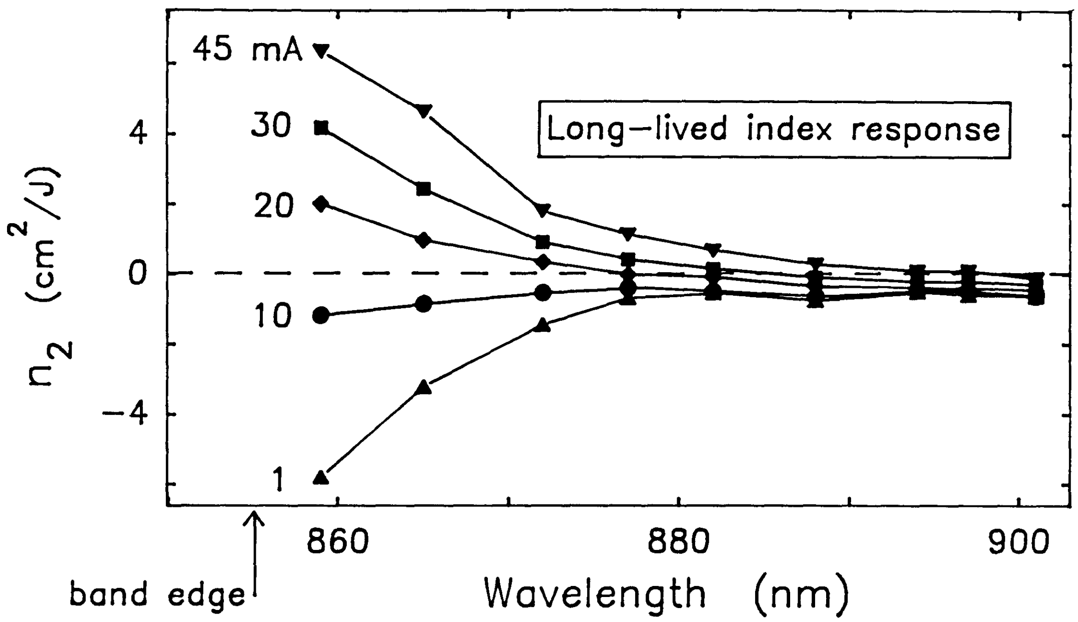

Figure 7.3: Nonlinear refractive index coefficients n_2 measured versus wavelength at several bias currents for the long-lived response.

Fig. 7.3 shows the below-band nonlinear index for the long-lived refractive index response. The negative n_2 is attributed to increasing the carrier density through two-photon absorption of pump photons. The positive n_2 indicates that heating of the lattice is dominating. Both effects fall off as we tune away from the band edge.

7.3 Other pump-probe studies

In this section we discuss and compare our results to other pump-probe studies of semiconductor waveguides. The first such measurements were performed by Stix, Kesler, and Ippen on AlGaAs diode laser amplifiers [12, 13, 14]. These pump-probe measurements of gain dynamics revealed the ultrafast gain compression dynamic caused by carrier heating. However, measurements performed with 100 fs pulses did not reveal any evidence for spectral hole burning. In particular, no positive gain dynamic in the absorption regime was observed [13], in contrast to the results in this thesis (see Fig. 4.7(c) on page 89). However, the results in Ref. [13] were obtained with an actively modelocked dye laser system followed by two stages of pulse compression. The pulses obtained in this manner are much noisier and have much larger pedestals than pulses from a modelocked Ti:sapphire laser system. Still, it is a little surprising that the spectral hole burning feature was not seen despite the poor quality of the pulses.

Evidence for spectral hole burning first emerged from gain measurements in InGaAsP diode laser amplifiers performed by Hall *et al.* [22, 23, 32]. Later, gain measurements performed on AlGaAs diode laser amplifiers using 400 fs pulses from a dye laser system showed no evidence for spectral hole burning [15]. It is possible that these long pulses could not resolve the $\sim$ 100 fs spectral hole burning feature. Finally, measurements performed with the Ti:sapphire laser on the same AlGaAs diode laser amplifiers [16, 17] revealed gain dynamics that were qualitatively similar to those seen by Hall *et al.* Thus, in InGaAsP and AlGaAs devices the dominant ultrafast gain dynamics were seen to be two-photon absorption, carrier heating with a delayed turn-on, and spectral hole burning [16, 17, 22, 23, 32].

Other pump-probe measurements on InGaAsP devices also support these processes as being responsible for the ultrafast gain dynamics [24, 100, 102]. In addition, stimulated cooling far in the absorption regime was also observed [100, 102] – this is the same effect as we saw in Fig. 6.4 on page 116. Finally, two-wavelength pump-probe studies of gain dynamics in strained-layer quantum well InGaAs diode laser amplifiers revealed a carrier heating dynamic that is primarily caused by stimulated transitions [19, 20]. Heating through free carrier absorption was seen to be a less important effect. Cooling through stimulated absorption was also seen far in the absorption regime [20].

Thus, these pump-probe measurements agree that two-photon absorption, carrier heating and cooling, and spectral hole burning are the dominant ultrafast gain dynamics in active semiconductor waveguides. The cause of carrier heating is attributed to some combination of free carrier absorption, two-photon absorption, and stimulated transitions – however, the relative importance of these processes has not definitely been established. It may depend to some extent on the material system and the device structure.

The other important class of time-resolved studies concerns pump-probe measurements of refractive index dynamics. The early work was performed by LaGasse and Anderson *et al.* on passive AlGaAs waveguides [27, 28, 29]. These below-band studies measured n_2 versus wavelength and revealed the resonant enhancement as the wavelength approaches the band edge [29]. The refractive index measurements pre-

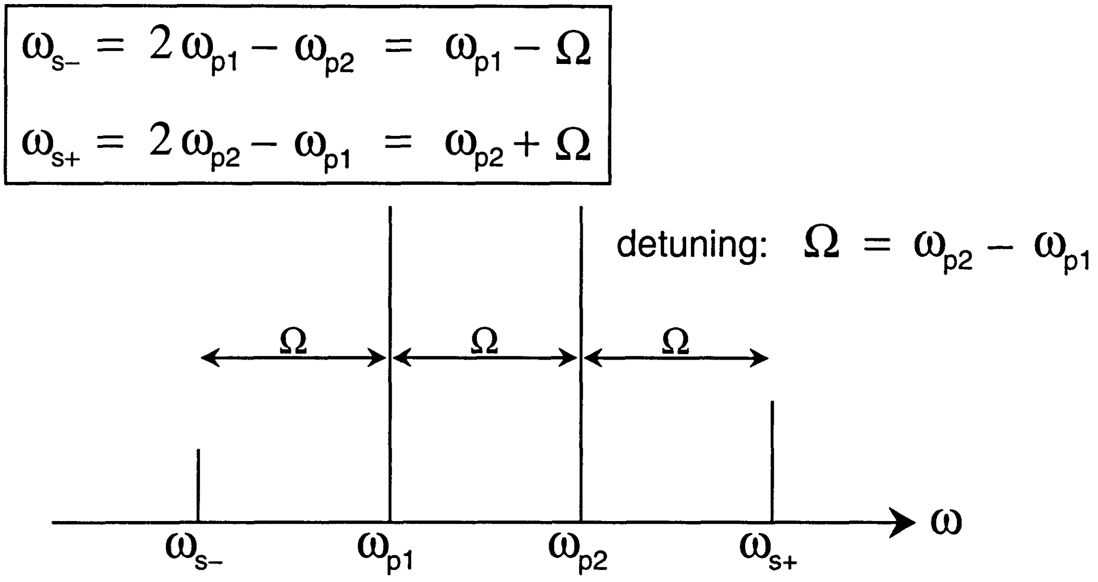

Figure 7.4: Four-wave mixing in a diode laser amplifier. Two CW pumps at frequencies ω_{p1} and ω_{p2} produce sidebands at ω_{s-} and ω_{s+}.

sented in this thesis are a continuation of those passive waveguide measurements. The below-band behavior of n_2 presented here agrees with that seen previously by LaGasse and Anderson *et al.* In this work, we have extended the measurements to an active structure that allowed carrier density dependent measurements to be performed.

Other measurements of spectral distortions experienced by pulses traveling through diode laser amplifiers have also shown evidence for ultrafast refractive index nonlinearities [11, 18]. However, the values for n_2 measured in one case are nearly five times larger than the n_2 we observe [11].

7.4 Four-wave mixing studies

Four-wave mixing (FWM) is a complementary experimental approach to time domain studies. In a FWM measurement two CW pump beams detuned by frequency Ω are sent through a diode laser amplifier (see Fig. 7.4). Through nonlinear interactions, sidebands are produced at $\omega_{s+} = \omega_{p2} + \Omega$ and $\omega_{s-} = \omega_{p1} - \Omega$. Notice that the magnitude of the sidebands is not necessarily the same. Measuring the sizes of the positive and negative detuned sidebands versus detuning reveals information about dynamics on a Ω^{-1} time scale.

The signal in a FWM measurement is proportional to $|H(\pm\Omega)|^2$, where $H(\Omega)$ is the Fourier transform of the complex response function $h'(t) + ih(t)$ [2, 34, 35, 40]. Thus, the two experimental approaches – pump-probe and FWM – should in theory yield the same results. Just as with pump-probe experiments, the FWM signal is analyzed by fitting with a theoretical response function. As in the fits to pump-probe data, there is a certain amount of ambiguity in the form of the response function. Further, since the FWM signal mixes the gain and index responses together, the FWM data is a bit more difficult to analyze. Pump-probe experiments have the advantage that the gain and the refractive index responses are measured separately. Also, pump-probe experiments can be performed in the gain, transparency, and absorption regimes, while FWM measurements are usually performed only in the gain regime.

Recently, there have been quite a few FWM measurements performed on diode laser amplifiers (most of them at 1.5 μm on InGaAsP devices) [34, 35, 37, 38, 39, 40, 41, 42, 43, 103, 104]. Studies by Zhou *et al.* have extended the detuning frequency out to 3.5 THz [40], corresponding to a temporal resolution of about 50 femtoseconds. In general, these FWM studies reveal ultrafast dynamics that agree with pump-probe studies. A few of these studies have observed responses that are consistent with carrier heating and spectral hole burning [39, 40, 41, 42, 104]. However, some have seen responses that are attributed primarily to spectral hole burning with little or no carrier heating signal present [34, 35]. This could be explained by the fact that these experiments were performed at frequencies red-shifted from the gain peak, as suggested by D'Ottavi *et al.* [104]. In that case, the response may be more sensitive to spectral hole burning effects and less sensitive to the carrier heating nonlinearity. Finally, the existence of a delay in the onset of carrier heating and the existence of spectral hole burning are issues currently being debated.

To bridge the gap between pump-probe measurements and FWM experiments, the FWM signal implied by our time domain response function will be presented. Here, we consider what sort of FWM signal one would expect based on the response function that was used to fit our pump-probe data for operation in the gain regime (Eq. (4.1) on page 93). To review, the complex impulse response function used to fit the pump-probe data can be written as a sum of exponential responses:

$$h(t) = \sum_m a_m \, (i - \alpha_m) \, e^{-t/\tau_m} \; . \tag{7.1}$$

The a_m constants are the fitting parameters, and the time constant of each dynamic is given by τ_m. The imaginary part of this expression represents the gain response, and the real part represents the refractive index response.

The α term is the alpha parameter that relates gain changes to index changes [105, 106]. For instance, the gain and index change resulting from a small change in carrier density dN are related by

$$\alpha = -\frac{4\pi}{\lambda}\frac{dn/dN}{dg/dN}. \tag{7.2}$$

The negative sign is included to make α a positive number since the carrier-induced gain and index changes have opposite signs. An analogous expression for α_T can be written to express the relation between the gain and index change that result from a carrier temperature change:

$$\alpha_T = -\frac{4\pi}{\lambda}\frac{dn/dT}{dg/dT}. \tag{7.3}$$

In the results presented here, we use $\alpha = 5$ and $\alpha_T = 2$ [15]. Note that both alpha parameters are positive, in agreement with the gain and refractive index responses we measure. The fits presented in the work by Zhou *et al.*, however, use a *negative* value for α_T [40, 41, 42]. This is a significant discrepancy with our results because a negative α_T implies that heating the carriers causes a negative gain change *and* a negative index change. It is possible that another response function $H(\Omega)$ can be found that fits the FWM data and gives a positive value for α_T.

We can Fourier transform Eq. 7.1 to get the FWM signal:

$$|H(\Omega)|^2 = \left|\sum_m \frac{a_m\tau_m(1 - i\alpha_m)}{1 - i\Omega\tau_m}\right|^2. \tag{7.4}$$

Plugging in typical values used for the fits to the above-band gain and refractive index data in the gain regime of operation, we obtain the four plots shown in Fig. 7.5.

The dotted straight line in each plot shows the −20 dB/decade roll-off caused by carrier density modulation. Carrier density effects begin to roll-off around 0.2 GHz; this response is analogous to the long-lived gain and refractive index changes seen in the above-band pump-probe measurements. The dashed line is the FWM

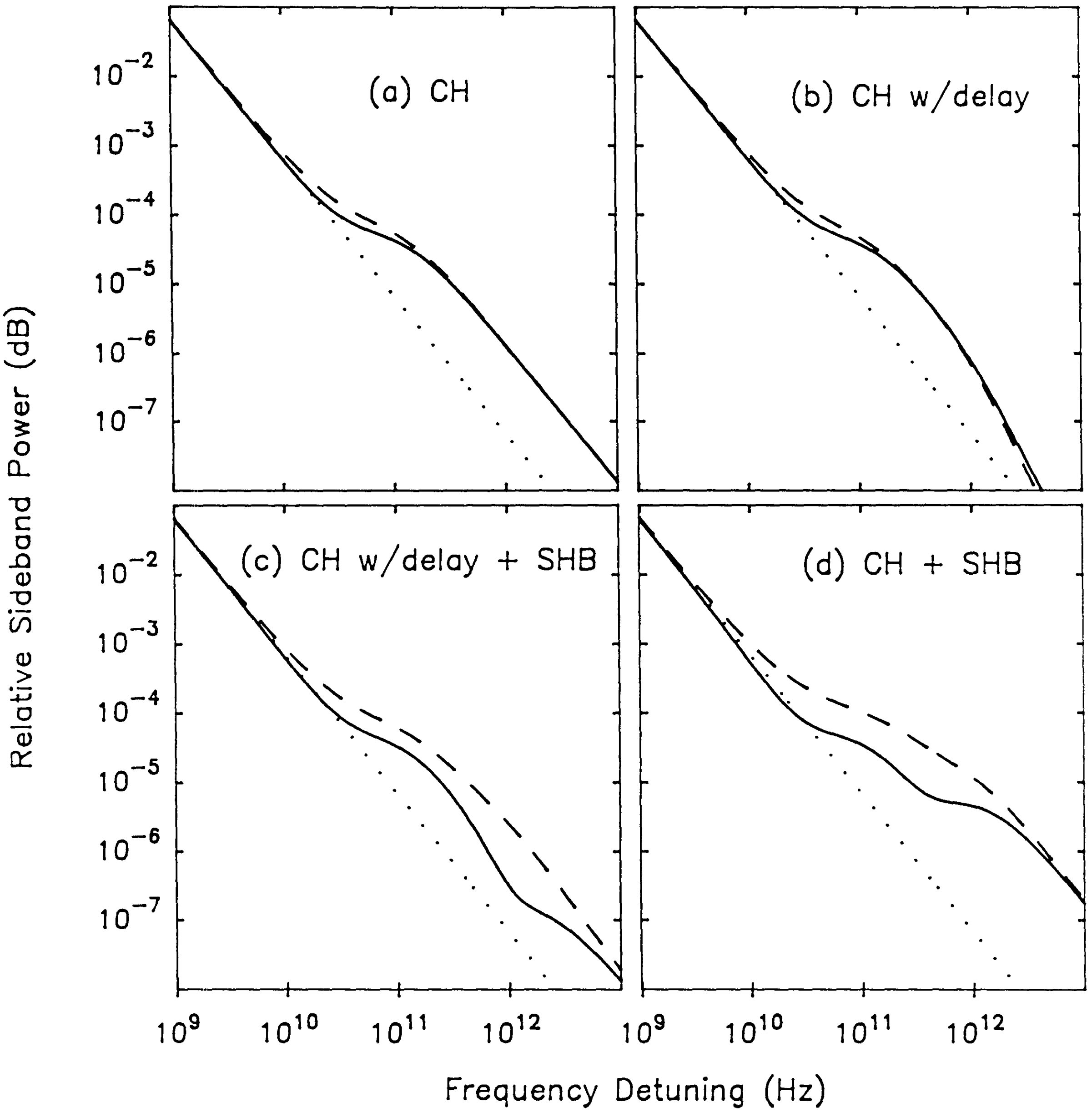

Figure 7.5: Predicted four-wave mixing signal. The dotted line shows the −20 dB/decade roll-off from carrier density modulation. The dashed line is for positive frequency detuning, and the solid line is for negative frequency detuning. The dynamics included in the plots are as follows: (a) carrier heating (no delay); (b) carrier heating with a delay, (c) carrier heating with delay, and spectral hole burning; and (d) carrier heating (no delay) and spectral hole burning.

signal for positive frequency detuning (ω_{s+}), and the solid line is the FWM signal for negative frequency detuning (ω_{s-}). In Fig. 7.5(a), the FWM signal for the 1.1 ps carrier heating nonlinearity without any delay is shown. In Fig. 7.5(b), the 120 fs carrier heating delay is included. Fig. 7.5(c) shows the predicted FWM signal for carrier heating (with the delay) and spectral hole burning. The shape of this curve agrees fairly well with the measurements of Zhou *et al.* [40, 41, 42]. Finally, Fig. 7.5(d) shows the FWM signal for carrier heating (without any delay) and spectral hole burning. The size of the SHB component has been increased by four times over the SHB component in plot (c). However, the similarity between Figs. 7.5(c) and (d) shows that it is difficult to draw conclusions from FWM data regarding spectral hole burning and the delay in carrier heating. That is, the second plateau in the negative frequency detuning response (solid line) could be caused by spectral hole burning and the carrier heating delay (plot (c)), *or* it could be caused just by a strong spectral hole burning dynamic (plot (d)).

Finally, the contributions from the instantaneous gain and refractive index dynamics – two-photon absorption and the optical Stark effect – have not been included in Fig. 7.5. The effect of these dynamics on the FWM signal is to add a constant term to the summation in Eq. 7.4. This constant term will cause the FWM response to eventually flatten out to a constant value at large frequency detunings. However, because of dispersion, the FWM response will still roll-off due to phase mismatch between the various frequencies. So, another explanation for the second plateau that appears at large detunings is that it is due to the instantaneous processes. This observation further complicates the analysis of FWM measurements at large detunings – spectral hole burning, the carrier heating delay, two-photon absorption, and the optical Stark effect are all tied up together. The instantaneous dynamics are generally not included in the analysis of recent FWM measurements. However, based on the measured pump-probe responses presented in this thesis, these nonlinearities are important and should not be ignored in analyzing FWM studies.

Both pump-probe measurements and FWM measurements have difficulty resolving dynamics on a 100 fs and faster time scale. Further, there are some discrepancies between the two approaches that remain to be resolved. Specifically, the existence of spectral hole burning and a delay in carrier heating needs to be studied further using both approaches. Perhaps performing pump-probe measurements with shorter pulses and FWM measurements with larger detunings will help. In addition, the instantaneous nonlinearities should be included in the analysis of FWM experiments.

Chapter 8

Conclusion

And now it's time for the traditional look at what was known, what was learned, and what remains to be done. Through a series of pump-probe measurements of an AlGaAs diode laser amplifier, we have studied the ultrafast gain and refractive index dynamics exhibited by an active semiconductor waveguide. In this work the processes of interest include two-photon absorption, free carrier absorption, stimulated transitions, and the optical Stark effect. These processes give rise to a variety of interesting dynamics such as carrier heating and cooling, spectral hole burning, and an instantaneous refractive index transient. By performing measurements at a variety of wavelengths, carrier densities, and pump powers, we have characterized the behavior of these dynamics over a broad range of conditions. From these studies we learned a great deal about fundamental processes in semiconductors. In the case of the refractive index dynamics, these measurements allowed the determination of the nonlinear refractive index coefficient n_2 as a function of wavelength and carrier density. In addition, some interesting artifacts caused by pulse chirp and spectral filtering taught us about the pump-probe experimental technique itself.

Thus, the pump-probe measurement technique applied to diode laser amplifiers reveals a great deal about fundamental processes in semiconductors. In addition, the results have important implications for practical devices involving active semiconductor waveguides. The next section outlines the impact of the results presented in this thesis on the development of practical active waveguide-based devices. Then, ideas for future experimental work are discussed.

8.1 Prospects for practical devices

A high-speed all-optical switch, in which one beam of light switches another, could be of use in future lightwave communication systems. An all-optical wavelength converter is another device that would be important in wavelength-division multiplexed communication networks. Both of these devices require fast, strong refractive index nonlinearities. The measurements of the nonlinear refractive index coefficients presented in this thesis allow us to evaluate the feasibility of using active semiconductor waveguides in an all-optical device. Further, having characterized the refractive index dynamics as a function of wavelength and carrier density, we can suggest operating regimes that would optimize device performance.

The first criterion for evaluating active waveguides for use in devices is the size of the refractive index nonlinearities. The n_2 for the instantaneous refractive index dynamic in AlGaAs is measured to be $\sim 10^{-12}$ cm^2/W, compared to $\sim 10^{-16}$ cm^2/W for optical fiber [68]. Thus, semiconductor waveguides offer refractive index nonlinearities about four orders of magnitude larger than optical fiber. This means, for example, that a fiber optic switch requiring 10 meters of optical fiber could be realized with a 1 millimeter-long semiconductor waveguide. Thus, the strength of refractive index nonlinearities in semiconductors makes semiconductor waveguides attractive candidates for compact all-optical devices.

In the case of an optical switch, a phase shift on the order of π radians must be achieved with moderate optical powers. Such a fast phase shift in an active semiconductor waveguide is feasible, but as the measurements in this thesis show, there are several issues that must be addressed. Although fast phase shifts are present, they are generally difficult to isolate from other undesirable dynamics. For instance, the ultrafast refractive index dynamics are usually accompanied by gain nonlinearities. Also, the refractive index response often includes a long-lived step index change. Finally, the ultrafast index response is composed of two ultrafast dynamics of opposite sign, the positive carrier heating dynamic and the negative instantaneous dynamic. In order to design a fast optical switch, one needs to suppress the unwanted gain dynamics and long-lived responses. In addition, one or the other fast index dynamic must be selected to provide a single ultrafast index dynamic which would not change sign.

Based on the measured nonlinear refractive index coefficients for carrier heating and the instantaneous index nonlinearity (see Fig. 7.2), we can suggest one promising approach for building an optical switch in an active semiconductor waveguide. This approach involves using the carrier heating refractive index dynamic rather than the instantaneous index dynamic. The carrier heating nonlinearity scales up with the pulse *energy*, while the instantaneous nonlinearity is proportional to the pulse *intensity*. Also, the carrier heating nonlinearity increases with carrier density, while the instantaneous nonlinearity is suppressed at high carrier densities. So, we can get a large positive index change by using "long" pulses (about 1 ps duration) and operating at a high bias current. This will eliminate most of the negative instantaneous index change due to the optical Stark effect, and we are left with the positive carrier heating index nonlinearity. The bias current applied to the waveguide could be used to tune the size of the carrier heating index change as desired. The beam that is being switched could be tuned below the band edge where the medium is transparent and no gain nonlinearities other than two-photon absorption are present.

The optimum pulse width for such a device is on the order of the recovery time of the carrier heating nonlinearity ($\sim$ 1.1 ps). Pulses much longer than 1 ps will not yield a larger index change because the carrier heating-induced index change will begin to recover within the duration of the pulse. Pulses shorter than 1 ps will exhibit the unwanted negative instantaneous index nonlinearity. Thus, pulses about 1 ps in duration would provide the best switching performance. This indicates that it is possible to operate an active waveguide switch at bit rates in excess of 100 gigabits per second.

Such high bit rates are not in demand now but may be required in future lightwave communication systems. As the demand increases for higher bit rates, the need for fast, compact all-optical switching devices will grow. In the future, active semiconductor waveguides could become the basic building block for such optical switching devices.

8.2 Future work

Here, we outline a few suggestions for future experiments. First, there are some discrepancies between pump-probe measurements and four-wave mixing measurements that remain to be resolved. Experiments performed in the frequency domain have shown evidence for carrier heating, but the delay in carrier heating and the presence of spectral hole burning in the gain regime is still being debated. One experiment that could be performed is to carefully measure the gain dynamics just below and just above the band edge. In the below-band case, the instantaneous transient results from two-photon absorption. In the above-band case, the instantaneous transient should include additional contributions from spectral hole burning. Careful measurements of the instantaneous transient above and below the band edge would reveal the importance of spectral hole burning in the gain regime.

Performing pump-probe measurements on a short waveguide would also improve our understanding of the dynamics that occur on the ~100 femtosecond time scale. The measurements described in this thesis were performed on a 300 μm-long waveguide. The shortest pulse that can be sent through this waveguide without experiencing significant broadening is on the order of 100 femtoseconds. Because of dispersion, shorter pulses sent through the waveguide broaden so much that the time resolution is actually worse than with a 100 femtosecond pulse. Performing pump-probe measurements on a waveguide cleaved to a 50 to 100 μm length would enable the use of pulses as short as 50 femtoseconds. This improved time resolution would allow the further study of spectral hole burning and the delay in carrier heating. From there, we could relate the results to four-wave mixing experiments and hopefully resolve some of the discrepancies that remain. Also, a delay in the turn-on of the instantaneous index transient caused by the optical Stark effect has been predicted [93] but not observed. Perhaps better time resolution would reveal this delay.

Now that the low-power behavior has been characterized, further measurements of the high-power response would be interesting and useful. First, some new nonlinear behavior may be uncovered – already we have seen that the carrier heating recovery time increases for high pump powers. Also, high-power results are of interest for device applications where we are interested in generating large phase shifts.

Another important issue in generating large phase shifts is the design of the active waveguide structure. Performing pump-probe measurements on a device with a large confinement factor would certainly increase the amount of probe phase shift that could be achieved. The diode lasers used in this work had relatively narrow active region (0.05 μm) that resulted in a confinement factor around 10%. Increasing the width of the active region would produce a larger confinement factor and a correspondingly larger phase shift. Demonstrating a π phase shift would show that all-optical switching devices are feasible.

Further, one could try to demonstrate an all-optical switch with such a wide active region device. As mentioned in the previous section, the below-band carrier heating index dynamic could be used as the switching nonlinearity, and measurements could be performed with pulses around 1 picosecond duration. After that, it might be possible to build a compact, modular switch with pulses provided by a modelocked diode laser, rather than using pulses from a Ti:sapphire laser system. Eventually, as workable switches are developed, other systems-type issues will have to be investigated. Examples include measurements of bit error rates and inter-symbol interference effects caused by long-lived dynamics.

Another issue that needs to be resolved is the rapid degradation of the devices as described in Chapter 1. Perhaps the devices would last longer if they were packaged in a hermetically sealed case and actively cooled by mounting them on a thermoelectric cooler.

Finally, all the measurements described here were performed on a structure with a bulk active region. One might predict that larger optical nonlinearities would be seen in quantum confined structures such as quantum wells and quantum wires. A multiple-quantum well diode laser structure could produce large phase shifts for use in an optical switch. In other measurements performed on quantum well diode lasers, however, the measured nonlinearities have been similar in size to the bulk nonlinearities [23, 32]. Thus, it is not clear that quantum structures would radically improve the performance of active waveguides for device applications. Still, such measurements might be interesting from a fundamental standpoint. For example, it might be possible to observe quantum effects such as exciton enhancements in quantum well and wire structures.

References

[1] E. P. Ippen and C. V. Shank, "Techniques for measurement," in *Ultrashort Light Pulses, Picosecond Techniques and Applications* (S.L. Shapiro, ed.), New York; Springer, 1977.

[2] G. P. Agrawal, "Population pulsations and nondegenerate four-wave mixing in semiconductor lasers and amplifiers," *J. Opt. Soc. Am. B*, vol. 5, no. 1, pp. 147–158, 1988.

[3] R. S. Tucker, "High-speed modulation of semiconductor lasers," *J. Lightwave Technol.*, vol. LT-3, pp. 1180–1192, 1985.

[4] J. E. Bowers, B. R. Hemenway, A. H. Gnauck, and D. P. Wilt, "High-speed InGaAsP constricted-mesa lasers," *IEEE J. Quantum Electron.*, vol. 22, no. 6, pp. 833–844, 1986.

[5] R. Olshansky, P. Hill, V. Lanzisera, and W. Powazinik, "Frequency response of 1.3 μm InGaAsP high speed semiconductor lasers," *IEEE J. Quantum Electron.*, vol. QE-23, no. 9, pp. 1410–1418, 1987.

[6] C. B. Su, J. Eom, C. H. Lange, C. B. Kim, R. B. Lauer, W. C. Rideout, and J. S. LaCourse, "Characterization of the dynamics of semiconductor lasers using optical modulation," *IEEE J. Quantum Electron.*, vol. 28, no. 1, pp. 118–127, 1992.

[7] R. Frankenberger and R. Schimpe, "Measurement of the gain saturation spectrum in InGaAsP diode lasers," *Appl. Phys. Lett.*, vol. 57, no. 24, pp. 2520–2522, 1990.

[8] R. Frankenberger and R. Schimpe, "Origin of nonlinear gain saturation in index-guided InGaAsP laser diodes," *Appl. Phys. Lett.*, vol. 60, no. 22, pp. 2720–2722, 1992.

[9] G. P. Agrawal and N. A. Olsson, "Self-phase modulation and spectral broadening of optical pulses in semiconductor laser amplifiers," *IEEE J. Quantun Electron.*, vol. 25, no. 11, pp. 2297–2306, 1989.

[10] A. Dienes, J. P. Heritage, M. Y. Hong, and Y. H. Chang, "Time- and spectral-domain evolution of subpicosecond pulses in semiconductor optical amplifiers," *Opt. Lett.*, vol. 17, no. 22, pp. 1602–1604, 1992.

[11] R. S. Grant and W. Sibbett, "Observations of ultrafast nonlinear refraction in an InGaAsP optical amplifier," *Appl. Phys. Lett.*, vol. 58, no. 11, pp. 1119–1121, 1991.

[12] M. S. Stix, M. P. Kesler, and E. P. Ippen, "Observations of subpicosecond dynamics in GaAlAs laser diodes," *Appl. Phys. Lett.*, vol. 48, no. 25, pp. 1722–1724, 1986.

[13] M. P. Kesler and E. P. Ippen, "Subpicosecond gain dynamics in GaAlAs laser diodes," *Appl. Phys. Lett.*, vol. 51, no. 22, pp. 1765–1767, 1987.

[14] M. P. Kesler and E. P. Ippen, "Subpicosecond spectral gain dynamics in AlGaAs laser diodes," *Electron. Lett.*, vol. 24, no. 17, pp. 1102–1103, 1988.

[15] C. T. Hultgren and E. P. Ippen, "Ultrafast refractive index dynamics in AlGaAs diode laser amplifiers," *Appl. Phys. Lett.*, vol. 59, no. 6, pp. 635–637, 1991.

[16] C. T. Hultgren, D. J. Dougherty, and E. P. Ippen, "Above- and below-band femtosecond nonlinearities in active AlGaAs waveguides," *Appl. Phys. Lett.*, vol. 61, no. 23, pp. 2767–2769, 1992.

[17] C. T. Hultgren, K. L. Hall, G. Lenz, D. J. Dougherty, and E. P. Ippen, "Spectral-hole burning and carrier heating nonlinearities in active waveguides," in *Picosecond Electronics and Optoelectronics Conference Technical Digest 1993*, pp. 6–12, 1993.

[18] P. J. Delfyett, Y. Silberberg, and G. A. Alphonse, "Hot-carrier thermalization induced self-phase modulation in semiconductor traveling wave amplifiers," *Appl. Phys. Lett.*, vol. 59, no. 1, pp. 10–12, 1991.

[19] C.-K. Sun, H. K. Choi, C. A. Wang, and J. G. Fujimoto, "Studies of carrier heating in InGaAs/AlGaAs strained-layer quantum well diode lasers using a multiple wavelength pump probe technique," *Appl. Phys. Lett.*, vol. 62, no. 7, pp. 747–749, 1993.

[20] C.-K. Sun, H. K. Choi, C. A. Wang, and J. G. Fujimoto, "Femtosecond gain dynamics in InGaAs/AlGaAs strained-layer single-quantum-well diode lasers," *Appl. Phys. Lett.*, vol. 63, no. 1, pp. 96–98, 1993.

[21] C.-K. Sun, B. Golubovic, J. G. Fujimoto, H. K. Choi, and C. A. Wang, "Heterodyne nondegenerate pump-probe measurement technique for guided wave devices." submitted to Opt. Lett., 1994.

[22] K. L. Hall, J. Mark, E. P. Ippen, and G. Eisenstein, "Femtosecond gain dynamics in InGaAsP optical amplifiers," *Appl. Phys. Lett.*, vol. 56, pp. 1740–1742, 1990.

[23] K. L. Hall, Y. Lai, E. P. Ippen, G. Eisenstein, and U. Koren, "Femtosecond gain dynamics and saturation behavior in InGaAsP multiple quantum well optical amplifiers," *Appl. Phys. Lett.*, vol. 57, pp. 2888–2890, 1990.

[24] J. Mark and J. Mørk, "Subpicosecond gain dynamics in InGaAsP optical amplifiers: Experiment and theory," *Appl. Phys. Lett.*, vol. 61, no. 19, pp. 2281–2283, 1992.

[25] M. Shirasaki, H. A. Haus, and D. Liu-Wong, "Nonlinear fiber interferometer and logic gate," in *Conference on Lasers and Electro-optics Technical Digest*, p. Th01, 1987.

[26] M. J. LaGasse, D. Liu-Wong, and H. A. Haus, "Ultrafast switching with a single-fiber interferometer," *Opt. Lett.*, vol. 14, no. 6, pp. 311–313, 1989.

[27] M. J. LaGasse, K. K. Anderson, H. A. Haus, and J. G. Fujimoto, "Femtosecond all-optical switching in AlGaAs waveguides using a time division interferometer," *Appl. Phys. Lett.*, vol. 54, no. 21, pp. 2068–2070, 1989.

[28] K. K. Anderson, M. J. LaGasse, C. A. Wang, J. G. Fujimoto, and H. A. Haus, "Femtosecond dynamics of the nonlinear index near the band edge in AlGaAs waveguides," *Appl. Phys. Lett.*, vol. 56, no. 19, pp. 1834–1836, 1990.

[29] M. J. LaGasse, K. K. Anderson, C. A. Wang, H. A. Haus, and J. G. Fujimoto, "Femtosecond measurements of the nonresonant nonlinear index in AlGaAs," *Appl. Phys. Lett.*, vol. 56, no. 5, pp. 417–419, 1990.

[30] K. L. Hall, G. Lenz, E. P. Ippen, and G. Raybon, "Heterodyne pump-probe technique for time-domain studies of optical nonlinearities in waveguides," *Opt. Lett.*, vol. 17, no. 12, pp. 874–876, 1992.

[31] K. L. Hall, A. M. Darwish, E. P. Ippen, U. Koren, and G. Raybon, "Femtosecond index nonlinearities in InGaAsP optical amplifiers," *Appl. Phys. Lett.*, vol. 62, no. 12, pp. 1320–1322, 1993.

[32] K. L. Hall, G. Lenz, E. P. Ippen, U. Koren, and G. Raybon, "Carrier heating and spectral hole burning in strained-layer quantum-well laser amplifiers at 1.5 μm," *Appl. Phys. Lett.*, vol. 61, no. 21, pp. 2512–2514, 1992.

[33] K. Inoue, T. Mukai, and T. Saitoh, "Nearly degenerate four-wave mixing in a travelling-wave semiconductor laser amplifier," *Appl. Phys. Lett.*, vol. 51, pp. 1051–1053, 1987.

[34] K. Kikuchi, M. Kakui, C.-E. Zah, and T.-P. Lee, "Observation of highly nondegenerate four-wave mixing in 1.5 μm traveling-wave semiconductor optical amplifiers and estimation of nonlinear gain coefficient," *IEEE J. Quantum Electron.*, vol. 28, no. 1, pp. 151–156, 1992.

[35] K. Kikuchi, M. Amano, C. E. Zah, and T. P. Lee, "Analysis of origin of nonlinear gain in 1.5 μm semiconductor active layers by highly nondegenerate four-wave mixing," *Appl. Phys. Lett.*, vol. 64, no. 5, pp. 548–550, 1994.

[36] H. Q. Le, W. D. Goodhue, and K. Rauschenbach, "Measurement of third order optical nonlinear susceptibility using four-wave mixing in a single-mode ridge waveguide," *Opt. Lett.*, vol. 15, no. 20, pp. 1126–1128, 1990.

[37] T. Mukai and T. Saitoh, "Detuning characteristics and conversion efficiency of nearly degenerate four-wave mixing in a 1.5 μm traveling-wave semiconductor laser amplifier," *IEEE J. Quantum Electron.*, vol. 26, no. 5, pp. 865–875, 1990.

[38] S. Murata, A. Tomita, J. Shimizu, M. Kitamura, and A. Suzuki, "Observation of highly nondegenerate four-wave mixing ($>$ 1 THz) in an InGaAsP multiple quantum well laser," *Appl. Phys. Lett.*, vol. 58, no. 14, pp. 1458–1460, 1991.

[39] L. F. Tiemeijer, "Effects of nonlinear gain on four-wave mixing and asymmetric gain saturation in a semiconductor laser amplifier," *Appl. Phys. Lett.*, vol. 59, no. 5, pp. 499–501, 1991.

[40] J. Zhou, N. Park, J. W. Dawson, K. J. Vahala, M. A. Newkirk, and B. I. Miller, "Efficiency of broadband four-wave mixing wavelength conversion using semiconductor traveling-wave amplifiers," *IEEE Photon. Technol. Lett.*, vol. 6, no. 1, pp. 50–52, 1994.

[41] J. Zhou, N. Park, J. W. Dawson, K. J. Vahala, M. A. Newkirk, and B. I. Miller, "Terahertz four-wave mixing spectroscopy for study of ultrafast dynamics in a semiconductor optical amplifier," *Appl. Phys. Lett.*, vol. 63, no. 9, pp. 1179–1181, 1993.

[42] J. Zhou, N. Park, J. W. Dawson, K. J. Vahala, M. A. Newkirk, U. Koren, and B. I. Miller, "Highly nondegenerate four-wave mixing and gain nonlinearity in a strained multiple-quantum-well optical amplifier," *Appl. Phys. Lett.*, vol. 62, p. 2301, 1993.

[43] R. Nietzke, P. Panknin, W. Elsässer, and E. O. Göbel, "Four-wave mixing in GaAs/AlGaAs semiconductor lasers," *IEEE J. Quantum Electron.*, vol. 25, no. 6, pp. 1399–1406, 1989.

[44] T. Saitoh and T. Mukai, "Recent progress in semiconductor laser amplifiers," *J. Lightwave Technol.*, vol. 6, no. 11, pp. 1656–1664, 1988.

[45] M. J. O'Mahony, "Semiconductor laser optical amplifiers for use in future fiber systems," *J. Lightwave Technol.*, vol. 6, no. 4, pp. 531–544, 1988.

[46] J. C. Simon, "GaInAsP semiconductor laser amplifiers for single-mode fiber communications," *J. Lightwave Technol.*, vol. LT-5, no. 9, pp. 1286–1295, 1987.

[47] G. Eisenstein, P. B. Hansen, J. M. Wiesenfeld, R. S. Tucker, and G. Raybon, "Amplification of high repetition rate picosecond pulses using an InGaAsP traveling-wave optical amplifier," *Appl. Phys. Lett.*, vol. 53, no. 16, pp. 1539–1541, 1988.

[48] J. M. Wiesenfeld, G. Eisenstein, R. S. Tucker, G. Raybon, and P. B. Hansen, "Distortionless picosecond pulse amplification and gain compression in a travelling-wave InGaAsP optical amplifier," *Appl. Phys. Lett.*, vol. 53, no. 14, pp. 1239–1241, 1988.

[49] N. A. Olsson and R. M. Jopson, "Two-stage high-gain optical amplifier," *J. Lightwave Technol.*, vol. 7, no. 5, pp. 791–793, 1989.

[50] H. A. Haus, E. P. Ippen, and F. J. Leonberger, "Nonlinear optical waveguide devices," in *Optical Signal Processing* (J. L. Horner, ed.), pp. 245–277, Academic Press, Inc.; New York, 1987.

[51] T. Durhuus, C. Joergensen, B. Mikkelsen, R. J. S. Pedersen, and K. E. Stubkjaer, "All optical wavelength conversion by SOA's in a Mach-Zehnder configuration," *IEEE Photon. Technol. Lett.*, vol. 6, no. 1, pp. 53–55, 1994.

[52] R. Schnabel, U. Hilbk, T. Hermes, P. Meiβner, C. Helmolt, K. Magari, F. Raub, W. Pieper, F. J. Westphal, R. Ludwig, L. Küller, and H. G. Weber, "Polarization insensitive frequency conversion of a 10-channel OFDM signal using four-wave-mixing in a semiconductor laser amplifier," *IEEE Photon. Technol. Lett.*, vol. 6, no. 1, pp. 56–58, 1994.

[53] A. Yariv, D. Fekete, and D. M. Pepper, "Compensation for channel dispersion by nonlinear optical phase conjugation," *Opt. Lett.*, vol. 4, no. 2, pp. 52–54, 1979.

[54] R. M. Jopson, A. H. Gnauck, and R. M. Derosier, "Compensation of fibre chromatic dispersion by spectral inversion," *Electron. Lett.*, vol. 29, pp. 576–578, 1993.

[55] M. C. Tatham, G. Sherlock, and L. D. Westbrook, "Compensation of fibre chromatic dispersion by optical phase conjugation in a semiconductor laser amplifier," *Electron. Lett.*, vol. 29, no. 21, pp. 1851–1852, 1993.

[56] J. Goodberlet, J. Wang, J. G. Fujimoto, and P. A. Schulz, "Femtosecond passively mode-locked Ti:Al_2O_3 laser with a nonlinear external cavity," *Opt. Lett.*, vol. 14, no. 20, pp. 1125–1127, 1989.

[57] D. E. Spence, P. N. Kean, and W. Sibbett, "60-fsec pulse generation from a self-mode-locked Ti:sapphire laser," *Opt. Lett.*, vol. 16, no. 1, pp. 42–44, 1994.

[58] L. Spinelli, B. Couillaud, N. Goldblatt, and D. K. Negus, "Starting and generation of sub-100 fs pulses in Ti:Al_2O_3 by self-focusing," in *Conference on Lasers and Electro-optics Technical Digest*, pp. 583–584 (postdeadline paper), 1991.

[59] M. T. Asaki, C.-P. Huang, D. Garvey, J. Zhou, H. C. Kapteyn, and M. M. Murnane, "Generation of 11-fs pulses from a self-mode-locked Ti:sapphire laser," *Opt. Lett.*, vol. 18, no. 12, pp. 977–979, 1993.

[60] A. Stingl, C. Spielmann, and F. Krausz, "Generation of 11-fs pulses from a Ti:sapphire laser without the use of prisms," *Opt. Lett.*, vol. 19, no. 3, pp. 204–206, 1994.

[61] K. Aiki, M. Nakamura, T. Kuroda, J. Umeda, R. Ito, N. Chinone, and M. Maeda, "Transverse mode stabilized $Al_xGa_{1-x}As$ injection lasers with channeled-substrate-planar structure," *IEEE J. Quantum Electron.*, vol. QE-14, no. 2, pp. 89–94, 1978.

[62] Chris Cook of MIT Lincoln Laboratory is gratefully acknowledged for his expert deposition of AR-coatings on the devices.

[63] J. K. Butler, "Theory of transverse cavity mode selection in homojunction and heterojunction semiconductor diode lasers," *J. Appl. Phys.*, vol. 42, no. 11, pp. 4447–4457, 1971.

[64] H. C. Casey and M. B. Panish, *Heterostructure Lasers, Part A: Fundamental Principles.* Academic Press; New York, 1978.

[65] H. C. Casey, D. D. Sell, and M. B. Panish, "Refractive index of $Al_xGa_{1-x}As$ between 1.2 and 1.8 eV," *Appl. Phys. Lett.*, vol. 24, no. 2, pp. 63–65, 1974.

[66] T. F. Marple, "Refractive index of GaAs," *J. Appl. Phys.*, vol. 35, no. 4, pp. 1241–1242, 1964.

[67] J. S. Blakemore, "Semiconducting and other major properties of gallium arsenide," *J. Appl. Phys.*, vol. 53, no. 10, pp. R123–R181, 1992.

[68] K. S. Kim, R. H. Stolen, W. A. Reed, and K. W. Quoi, "Measurement of the nonlinear index of silica-core and dispersion-shifted fibers," *Opt. Lett.*, vol. 19, no. 4, pp. 257–259, 1994.

[69] G. P. Agrawal, *Nonlinear Fiber Optics.* Academic Press; Boston, 1989.

[70] G. Lasher and F. Stern, "Spontaneous and stimulated recombination radiation in semiconductors," *Phys. Rev.*, vol. 133, no. 2a, pp. a553–a563, 1964.

[71] R. L. Liboff, *Introductory Quantum Mechanics.* Holden-Day; Oaktown, California, 1980.

[72] M. G. A. Bernard and G. Duraffourg, "Laser conditions in semiconductors," *Phys. Stat. Solid*, vol. 1, no. 7, pp. 699–703, 1961.

[73] J. I. Pankove, *Optical Processes in Semiconductors.* Dover Publications, Inc.; New York, 1971.

[74] F. Stern, "Dispersion of the index of refraction near the absorption edge of semiconductors," *Phys. Rev.*, vol. 133, no. 6a, pp. A1653–A1664, 1964.

[75] C. H. Henry, R. A. Logan, and K. A. Bertness, "Spectral dependence of the change in refractive index due to carrier injection in GaAs lasers," *J. Appl. Phys.*, vol. 52, no. 7, pp. 4457–4461, 1981.

[76] B. R. Bennett, R. A. Soref, and J. A. del Alamo, "Carrier-induced change in refractive index of InP, GaAs, and InGaAsP," *IEEE J. Quantum Electon.*, vol. 26, no. 1, pp. 113–122, 1990.

[77] J. Manning, R. Olshansky, and C. B. Su, "The carrier-induced index change in AlGaAs and 1.3 μm InGaAsP diode lasers," *IEEE J. Quantum Electron.*, vol. 19, no. 10, pp. 1525–1530, 1983.

[78] S. H. Park, J. F. Morhange, A. D. Jeffery, R. A. Morgan, A. Chavez-Pirson, H. M. Gibbs, S. W. Koch, N. Peyghambarian, M. Derstine, A. C. Gossard, J. H. English, and W. Weigmann, "Measurements of room-temperature band-gap-resonant optical nonlinearities of GaAs/AlGaAs multiple quantum wells and bulk GaAs," *Appl. Phys. Lett.*, vol. 52, no. 15, pp. 1201–1203, 1988.

[79] Y. H. Lee, A. Chavez-Pirson, S. W. Koch, H. M. Gibbs, S. H. Park, J. Morhange, A. Jeffery, N. Peyghambarian, L. Banyai, A. C. Gossard, and W. Wiegmann, "Room-temperature optical nonlinearities in GaAs," *Phys. Rev. Lett.*, vol. 57, no. 19, pp. 2446–2449, 1986.

[80] Z. Vardeny and J. Tauc, "Picosecond coherence coupling in the pump and probe technique," *Opt. Comm.*, vol. 39, no. 6, pp. 396–400, 1981.

[81] T. F. Heinz, S. L. Palfrey, and K. B. Eisenthal, "Coherent coupling effects in pump-probe measurements with collinear, co-propagating beams," *Opt. Lett.*, vol. 9, no. 8, pp. 359–361, 1984.

[82] S. L. Palfrey and T. F. Heinz, "Coherent interactions in pump-probe absorption measurements: the effect of phase gratings," *J. Opt. Soc. Am. B*, vol. 2, no. 4, pp. 674–678, 1985.

[83] H. J. Eichler, D. Langhans, and F. Massmann, "Coherence peaks in picosecond sampling experiments," *Opt. Comm.*, vol. 50, no. 2, pp. 117–122, 1984.

[84] A. von Jena and H. E. Lessing, "Coherent coupling effects in picosecond absorption experiments," *Appl. Phys.*, vol. 19, pp. 131–144, 1979.

[85] W. H. Knox, D. S. Chemla, and G. Livescu, "High density femtosecond excitation of nonthermal carrier distributions in intrinsic and modulation doped GaAs quantum wells," *Sol. St. Electron.*, vol. 31, no. 3, pp. 425–450, 1988.

[86] W. H. Knox, D. S. Chemla, G. Livescu, J. E. Cunningham, and J. E. Henry, "Femtosecond carrier thermalization in dense Fermi seas," *Phys. Rev. Lett.*, vol. 61, no. 11, pp. 1290–1293, 1988.

[87] M. C. Gabriel, H. A. Haus, and E. P. Ippen, "Thermal index changes by optical absorption in group III-V semiconductor waveguides," *J. Lightwave Technol.*, vol. LT-4, no. 10, pp. 1482–1493, 1986.

[88] The explanation for the refractive index artifact that is outlined in this section was developed by David Dougherty.

[89] J. P. Van der Ziel, "Self-focusing effects in pulsating $Al_xGa_{1-x}As$ double-heterostructure lasers," *IEEE J. Quantum Electron.*, vol. 17, no. 1, pp. 60–68, 1981.

[90] D. Botkin, S. Weiss, G. Sucha, D. S. Chemla, and J. M. Wiesenfeld, "Ultrafast dynamics of the optical mode of a 1.5 μm multiple quantum well optical amplifier," *Appl. Phys. Lett.*, vol. 64, no. 21, pp. 2861–2863, 1994.

[91] M. Sheik-Bahae, D. C. Hutchings, D. J. Hagan, and E. W. Van Stryland, "Dispersion of bound electronic nonlinear refraction in solids," *IEEE J. Quantum. Electron.*, vol. 27, no. 6, pp. 1296–1309, 1991.

[92] M. Sheik-Bahae, J. Wang, and E. W. Van Stryland, "Nondegenerate optical Kerr effect in semiconductors," *IEEE J. Quantum. Electron.*, vol. 30, no. 2, pp. 249–254, 1994.

[93] M. Sheik-Bahae and E. W. Van Stryland, "Ultrafast nonlinearities in semiconductor laser amplifiers." submitted to *IEEE J. Quantum. Electron.*, 1994.

[94] K. L. Hall, E. P. Ippen, and G. Eisenstein, "Bias-lead monitoring of ultrafast nonlinearities in InGaAsP diode laser amplifiers," *Appl. Phys. Lett.*, vol. 57, pp. 129–131, 1990.

[95] V. V. Lu'c, P. G. Eliseev, M. A. Manko, and G. T. Mikaelian, "Electrical diagnostics of the amplifier operation and a feasibility of signal registration on the basis of the voltage saturation effect in junction laser diodes," *IEEE J. Quantum Electron.*, vol. QE-19, no. 6, pp. 1080–1083, 1983.

[96] Y. Mitsuhashi, J. Shimada, and S. Mitsutsuka, "Voltage change across the self-coupled semiconductor laser," *IEEE J. Quantum Electron.*, vol. QE-17, no. 7, pp. 1216–1225, 1981.

[97] S. M. Sze, *Physics of Semiconductor Devices.* John Wiley and Sons; New York, 1981.

[98] D. A. O. Davies, M. A. Fisher, D. J. Elton, S. D. Perrin, M. J. Adams, G. T. Kennedy, R. S. Grant, P. D. Roberts, and W. Sibbett, "Nonlinear switching in InGaAsP laser amplifier directional couplers biased at transparency," *Electron. Lett.*, vol. 29, no. 19, pp. 1710–1711, 1993.

[99] J. Mørk and A. Mecozzi, "Response function for gain and refractive index dynamics in active semiconductor waveguides." to be published in Appl. Phys. Lett., 1994.

[100] J. Mørk, J. Mark, and C. P. Seltzer, "Carrier heating in InGaAsP laser amplifiers due to two-photon absorption," *Appl. Phys. Lett.*, vol. 64, no. 17, pp. 2206–2208, 1994.

[101] S. A. Lyon, "Spectroscopy of hot carriers in semiconductors," *J. Luminescence*, vol. 35, pp. 121–154, 1986.

[102] M. Willatzen, J. Mark, J. Mørk, and C. P. Seltzer, "Carrier temperature and spectral holeburning dynamics in InGaAsP quantum well laser amplifiers," *Appl. Phys. Lett.*, vol. 64, no. 2, pp. 143–145, 1994.

[103] A. Uskov, J. Mørk, J. Mark, M. C. Tatham, and G. Sherlock, "Terahertz four-wave mixing in semiconductor optical amplifiers: experiment and theory." submitted to Appl. Phys. Lett., 1994.

[104] A. D'Ottavi, E. Iannone, A. Mecozzi, S. Scotti, P. Spano, J. Landreau, A. Ougazzaden, and J. C. Bouley, "Investigation of carrier heating and spectral hole burning in semiconductor amplifiers by highly nondegenerate four-wave mixing," *Appl. Phys. Lett.*, vol. 64, no. 19, pp. 2492–2494, 1994.

[105] C. H. Henry, "Theory of the linewidth of semiconductor lasers," *IEEE J. Quantum Electron.*, vol. 18, no. 2, pp. 259–264, 1982.

[106] M. Osiński and J. Buus, "Linewidth broadening factor in semiconductor lasers – an overview," *IEEE J. Quantum Electron.*, vol. QE-23, no. 9, pp. 9–29, 1987.